The Density-Enthalpy Method

Applied to Model

Two–phase Darcy Flow

IBRAHIM,

Master of Science (M.Sc.) Systems Engineering, Pakistan Institute of Engineering
and Applied Sciences, Quaid-i-Azam University Islamabad, Pakistan

geboren te Haripur, Pakistan.

Dit proefschrift is goedgekeurd door de promotor:
Prof.dr.ir. C. Vuik
Toegevoegd promotor:
Dr.ir. F. J. Vermolen

Samenstelling promotiecommissie:

Rector Magnificus	voorzitter
Prof.dr.ir. C. Vuik	Technische Universiteit Delft, promotor
Dr.ir. F. J. Vermolen	Technische Universiteit Delft, toegevoegd promotor
Prof.dr.ir. J. M. Nordbotten	Universiteit Bergen, Norge
Prof.dr.ir. C. R. Kleijn	Technische Universiteit Delft
Prof.dr. R. M. M. Mattheij	Technische Universiteit Eindhoven
Prof.dr.ir. A. W. Heemink	Technische Universiteit Delft
Dr.ir. E. S. J. Rudolph	Technische Universiteit Delft

The density-enthalpy method applied to model two–phase Darcy flow.
Dissertation at Delft University of Technology.

Cover: Later

Summary

In this thesis, we use a more recent method to numerically solve two-phase fluid flow problems. The method is developed at TNO and it is presented by Arendsen *et al.* in [1] for spatially homogeneous systems. We will refer to this method as *the density-enthalpy method* (DEM) because the density-enthalpy phase diagrams play an important role in this approach. Multiphase flow occurs in numerous natural and industrial processes. These processes (or flow systems) are typically modeled by one or more sets of PDEs. In the literature, a huge variety of mathemaical models for flow and transport in porous media are presented and used to simulate these processes. Many authors classify them into moving grid/free boundary methods and fixed grid methods. The method we use lie in the later category. Although DEM is developed for multiphase flow problems but this thesis is limited only to two-phase fluid flow of one substance (Propane). As the name indicates, density and enthalpy are our primary variables.

The mathematical model for our approach consists of a mass balance, an energy balance, Darcy's law and other thermodynamic relations. We solve the mass and energy balances for two state variables, the density (ρ) and the enthalpy (h). Other solution variables (such as pressure, temperature, and gas mass fraction, etc) are obtained from given ρ-h phase diagrams. These diagrams are obtained from thermodynamic properties of a substance (in our case the substance is Propane). For the spatial discretization, we use the finite-element method. An Euler Backward method is used for the time integration.

The finite-element method is used for the spatial discretization of the system over $1D$ and $2D$ grids. This method is selected because of its ability to handle complex domain geometries. In particular, SUPG (Streamline Upwind Petrove-Galerkin) is used in the initial chapters. The use of SUPG is related to the numerical wiggles as discussed in the coming chapters. Later on, a standard Galerkin algorithm is applied where no spurious oscillations are observed. We use piecewise (bi-)linear basis functions to approximate solution variables and test functions appearing in the weak forms of the PDEs.

The backward Euler method is used for the time integration of the PDEs. The use

of piecewise (bi-)linear basis functions and Euler backward time integration scheme implies a numerical error of order $O(\Delta x^2 + \Delta t)$, where Δx and Δt are the spatial and time steps, respectively. This is verified numerically.

The $0D$ model works fine as shown by Arendsen [1, 2, 3]. The first attempt to solve a multidimensional flow system by using density-enthalpy phase diagrams was made by Abouhafç in [12]. He used the IMEX (IMplicit-EXplicit) scheme for system linearization. For his solver, it was necessary to use very small time-steps. This also means that a large computation time is required for a relatively small process time. At the start of our thesis, the real cause behind a small time-step necessity was unknown. We started with IMEX to verify the results obtained by Abouhafç. Next, we applied Euler backward with the Picard iteration method but the challenge of a small time-step remained there. Later on, we show that our criterion for choosing the initial guess, as required at the start of each Picard iteration, makes it equivalent to IMEX linearization scheme, which imposes an upper bound on the time-step for convergence. This motivated us to use the Newton-Raphson method for the system linearization. In general, the Newton method is more sensitive to the initial guess. In our case, we use the system variables from the previous time-step as initial guess at the start of a fresh Newton-Raphson iteration. We have shown that this scheme successfully allows a reasonably large time-step (independent of the spatial grid size).

Another challenge at the start of our thesis was to deal with solution variables exhibiting nonphysical steep gradients and sudden variations near the boundary. This problem also appeared in [12] but it was left untreated. We have shown that the use of nonhomogeneous boundary conditions makes the problem ill-posed. This is responsible for nonphysical behavior of the solution variables. We propose some guidelines to use nonzero boundary fluxes to keep the problem well-posed.

From the simulation results of this fluid system, we conclude that the new method can successfully be applied to numerically solve multi-phase fluid systems. However we need to consider certain aspects regarding this approach. One issue is that density-enthalpy phase diagrams are not widely available for many multi-phase systems. There are also certain issues with non-homogenous boundary conditions (such as well-posedness and selection criterion of certain parameters). These issues are treated partially but are also included in the recommendation for future work.

Contents

List of Tables

x

List of Figures

Chapter 1

Introduction

A literature review on mathematical models for transport in porous media is presented. Further, the Density–Enthalpy Method that is developed and of which the equations are solved in this thesis, is evaluated in terms of its differences from traditional approaches, as well as its merits and demerits. A short summary for the coming chapters in the thesis is given at the end of this chapter.

1.1 Literature Overview

In the literature, a huge variety of mathematical models for flow and transport in porous media are presented and used to simulate all kinds of processes like oil extraction from underground reservoirs, sequestration of carbon–dioxide in sub–soil reservoirs, as well as fortification of sandy soils, to mention just a few. The models are all based on conserved quantities, such as volumetric fraction through saturations, mass, enthalpy (energy). Since, the models involve the interplay of many physical parameters like the soil permeability, fluid viscosity, temperature, etc., the formalisms often inherit a challenging nonlinear character in the resulting system of partial differential equations. Further, in some of the applications, in particular in Riemann problems, the solutions exhibit a shock–like behavior, which also needs a careful numerical assessment with the use of flux/slope–limiters in discretization techniques like the finite–volume, finite–element or discontinuous Galerkin methods. In this section, we discuss some classes of models. We emphasize that a complete description falls outside the scope of the thesis.

1.1.1 A Fractional Flow Model: The Buckley–Leverett Formulation

The simplest model that we consider is based on conservation of fluid volume. The model accounts for a balance in a fully saturated porous medium. Let the porous

medium in the domain Ω be homogeneous and isotropic with porosity ϕ. We formulate the volume balance equations for the viscous fluid in a porous medium for two phases. Let S_i denote the saturation of phase i (in our case liquid or gas), which is the volume fraction of phase i, then the volume balance equations are for $(x, y, z) \in \Omega$, $t > 0$:

$$\phi \frac{\partial S_i}{\partial t} + \underline{\nabla} \cdot \underline{q}_i = 0, \qquad i \in \{1, 2\}. \tag{1.1}$$

Here $\underline{q}_i = (q_{i,x}, q_{i,y}, q_{i,z})^T$ denotes the specific discharge of phase i. Further, ϕ is the porosity. The relation between the specific discharge and the pressure gradient is modeled through Darcy's Law

$$\underline{q}_i = -\frac{k_o k_{ri}(S_i)}{\mu} (\nabla p_i + \rho_i g \underline{e}_z), \tag{1.2}$$

where k_o, p_i, ρ_i, respectively, denote the intrinsic permeability, relative permeability of phase i, and the specific mass of phase i. The above equation models the competition of two phases in a bi–phasic flow problem. The difference between the pressures of the two phases is the capillary pressure, and this pressure is classically modeled through the Leverett equation, although there exist more modern formalisms, among which we mention the model due to Hassanizadeh. Further, under neglection of the capillary pressure, the pressure p_i in the above equation is replaced with p. The above formalism can be extended to a multi–phase environment. Since S_i should be summable to unity, we obtain

$$\sum_i \nabla \cdot \underline{q}_i = 0, \tag{1.3}$$

which provides an equation for the pressure. The system of equations is supplemented with an initial condition, as well as with boundary conditions. For the one–dimensional counterpart, under neglecting the capillary pressure, we get

$$\phi \frac{\partial S_i}{\partial t} + Q(t) \frac{\partial f_i(S_i)}{\partial x} = 0, \qquad i \in \{1, 2\}, \tag{1.4}$$

where $\sum_i \frac{\partial q_i}{\partial x} = 0$ implies $\sum_i q_i = Q(t)$. Further, we have

$$f_i(S_i) = \frac{k_{ri}(S_i)}{\sum_j k_{rj}(S_i)}.$$

The hyperbolic relation (1.4) is known as the famous Buckley–Leverett equation. This equation is used as a benchmark problem for many numerical strategies in porous media flow. Therefore, an extensive study of the behavior of analytic solutions in terms of (combinations of) rarefactions and shocks (through the Rankine–Hugoniot condition for the equation of motion). For an analytic treatment, we refer to Smoller among many others.

1.1.2   The Enthalpy Treatment

Besides matter, also heat is transported in the porous medium by flow and diffusion. This necessitates a rigorous treatment of the thermodynamic aspects of the system to be considered. In many studies, enthalpy is used as the primary variable, rather than temperature. This treatment removes the need to use substitution of state–variables and may hence lead to a simpler implementation of complex numerical schemes such as grid adaptive methods, as well as higher–order discretization methods. In the framework of the enthalpy method in a porous medium, we summarize the work by Brantferger *et al.* (1991), where a multi–phase–species model is considered. The current treatment is not carried out in full rigor. The specific discharge is assumed to be related to the pressure gradient via the generalized multi–phase Darcy Law. Further, the number of moles of each chemical in each phase is tracked over time and position via

$$\frac{1}{V_b}\frac{\partial n_i}{\partial t} + \nabla \cdot \sum_j (x_{ij}\rho_j q_j) = 0, \qquad i \in \{1, 2\}, \tag{1.5}$$

under absence of further reactions. Here V_b, n_i, x_{ij} and ρ_j, respectively, denote the bulk volume, vector with the number of moles of each component in phase i, molar fraction of component j in phase i, and the specific mass of component j. Further, q_j represents the volumetric discharge (flux) of phase j. Next to the above equation, describing the balance of matter, we have conservation of energy, modeled by

$$\frac{1}{V_b}\frac{\partial U}{\partial t} + \nabla \cdot \left[\sum_j (\rho_j H_j u_j) - D\nabla T \right] = 0. \tag{1.6}$$

Here, U, H_j, D, T, respectively, denote the total internal energy, enthalpy of phase j, the heat conductivity coefficient and temperature. In addition to these conservation laws, the time–derivative of the pore volume constraint is used as an independent equation, see Brantferger *et al.* (1991) to link the total fluid volume, porosity and the pressure. Further, the volume fraction of each phase is computed via the thermodynamic relations. In this formalism, the component mole numbers in each phase are modeled to account for matter. The densities of the phases present are used as input parameters. All this information can be used to determine the total density in the associated flow problem.

1.1.3   Various Studies for Multi-Phase Flow in Porous Media

In the context of a fractional flow formulation, with an extension to capillary pressure between steam and nitrogen, we mention the study by Lambert *et al.* (2010) on the analysis of Riemann solutions. Principles from Lake (1989) and Smoller (1983) are used to construct analytic solutions of the Riemann problem in terms of rarefactions and shocks. The transport of matter is, as in Brantferger *et al.* (1991), combined with transport of energy, where the enthalpy of the system is tracked over position in the medium and over time. Diffusion of heat is neglected in their study in order to

deal with a fully hyperbolic system of partial differential equations. The speed of the characteristics is analyzed by solving a standard spectral problem. The results indicate the existence of either shocks or diffuse (rarefaction) profiles. The same problem was dealt with earlier in the study of Bruining & van Duijn (2006) in the framework of existence and construction of traveling wave solutions. The lastmentioned study encompasses a fractional flow formulation of a tri–phasic problem (water, oil and steam) with the use of fractional flow model under incorporating a Brooks–Corey relation for the capillary pressure. The temperature distribution is obtained by setting the temperature discontinuous over the front position and hence the temperature is not solved as an additional unknown. Analytic expressions are obtained for the front velocity which are used for the construction of discontinuous traveling wave solutions.

A slightly different formalism, based on fractional flow principles, is presented by Amaziane & Jurak (2007). Their model solely tracks the transport of matter and is based on the introduction of a 'global pressure'. This global pressure introduces a nonlinear parabolic term. They use a Picard Fixed Point Method to construct a numerical solution. The paper by Chen & Ewing (1997) compares the use of various formulations for three–phase flow in porous media. The formalisms are the phase formulation with total velocity and with total flux, and the approach of a global velocity. The statement in full rigor of these systems is beyond the scope of this chapter. All formulations are based on the fractional flow formulation. The comparisons are done with respect to accuracy and efficiency. The saturations are obtained through a finite–volume method and the pressure equations are solved using a mixed finite–element method (Raviart–Thomas–Nedelec elements). Various tests were done with different relations between relative permeabilities and saturations.

Krautle and Knabner (2007) formulated a multicomponent multiphase problem in a generic way. This includes a set of PDEs for dynamic components, ODEs for static species and algebraic equations for equilibrium reactions. They presented a method to reduce the number of equations to solve the system efficiently. This involves a technique to decouple some of the equations, leading to small nonlinear systems. The smaller systems are solved by global implicit approach (GIA).

Niessner & Hassanizadeh (2007) present a macro–scale model in porous media that is based on a fractional flow formalism for multi–phase flow. An extended form of Darcy's Law is used with a rigorous thermodynamic assessment. This assessment yields a modified relation for the capillary pressure where next to the saturation, the specific interfacial area is taken into account. It is shown that their novel capillary pressure model is capable of capturing physical processes such as hysteresis, which were not captured in classical formalisms.

With respect to numerical solution strategies, we remark that most studies are based on a finite–volume discretization of the saturation / hyperbolic partial differential equations. The hyperbolic nature with the possible existence of shocks complicates the finite–element treatment in many cases. To overcome spurious oscillations, SUPG techniques are often employed. Their main drawback, however, is the incorporation of numerical diffusion, which flattens out sharp profiles, that is interfaces between adjacent phases. To this extent, we mention the work by Nayagum *et al.*

(2004) where a discontinuous Galerkin method, to solve the hyperbolic equations, is combined with a mixed finite–element method with applications in two–phase flow in porous media.

We also note that the enthalpy method is also applied in studies devoted to moving boundary problems, such as classical Stefan problems, with phase separation. This class of models could also fit in the framework of micro–models in a single pore. Finally, we mention the application by Celia & Nordbotten (2009) of simplified models with elegant analysis on–the–back–of–an–envelop–expressions for porous media flow in order to simulate and analyze sequestration of carbondioxide in the subsoil to store green house gases.

1.1.4 The Present Model's Perspective

In this section, we describe the perspective of the work in this thesis in the framework of all the aforementioned models. The present work, referred to as the *Density–Enthalpy Method* (DEM), is, like the models described earlier, based on a macro–scale formalism for transport in porous media. The difference is that the density in the DEM is, next to the enthalpy, one of the primary variables. The density refers to all flowing agents, in the current case, liquid and gas phases of propane. The model was first derived and considered by Arendsen *et al.* for a spatially homogeneous case. Using the values of the total fluid density and total fluid enthalpy, the constitutive relations from thermodynamics define the pressure, temperature and gas fraction at any time. The model is very close to thermodynamics as the density is considered as a continuous variable and in the sense that herewith the actual evolution of mass is modeled. A demerit may be that the volume fractions of each phase may be determined in a somewhat less accurate way, due to post–processing steps to evaluate the phase fractions, than if these parameters would have been determined directly via a volume balance. In the present thesis and in the MSc–work of Abdelhac, the spatially homogeneous model is extended to a spatial model in more dimensions. This formalism is also different from the classical fractional flow formulations in the sense that the actual total density is modeled as one of the primary variables instead of the direct evaluation of the volume fractions of the phases involved in the system. Therefore, the current DEM models *conservation of mass*, rather than *conservation of volume* in the classical fractional flow formulations. The temporal evolution of heat (temperature) is modeled through an enthalpy method, which is consistent with most of the studies in literature. However, the current approach with the direct evaluation of the total fluid density, enables a slightly different treatment of the energetic balance through a more simple, but physically sound, conservation law. The current DEM is hence very close to thermodynamics as one would use to model the spatially homogeneous case ($0D$ problem) based on a set of ordinary differential equations combined with constitutive relations from thermodynamics. These features make the DEM an interesting candidate for a numerical study. A comparative study with the other model approaches that are based on an enthalpy formalism should be done in future studies to sustain the merits and demerits of the DEM.

1.2   Outline of the thesis

We developed our understanding about the system model with the passage of time. The thesis is organized in a chronological way. The complexity of the solution algorithm also increases with each chapter of the thesis. Following is a short summary for the coming chapters.

- In Chapter 2, we start with numerical solutions of $1D$ convection and diffusion equations by FEM, which serves as the building blocks of the original system (in later chapters). We also solve a simplified nonlinear flow system.

- In Chapter 3, the $1D$ mathematical modeling of a real flow problem in the context of density-enthalpy method is provided. We use SUPG for the spatial discretization, Euler backward for the time integration and an IMEX method for the lineralization. We also tried Picard iteration method for linearization. In the simulation section, we take many test cases including isolated and open system for mass or/and energy. The system dynamics are interpreted on basis of physical laws.

- In Chapter 4, we show that the non-homogeneous boundary conditions make the problem ill-posed. We solve a $2D$ flow system with a zero inward mass and energy fluxes. In the simulation section, we show that the solution algorithm works for the $2D$ case.

- In Chapter 5, we figure out the origin of a small time-step necessity. It is shown that a fully implicit time integration scheme solves the problem very efficiently. Furthermore, we experiment with phase-front tracking to compare the density-enthalpy method qualitatively to the level-set method.

- Chapter 6 is devoted to the stability analysis and convergence rate of the numerical solution of the ρ-h model. For stability analysis, the system is transformed from "many-equations" to an equivalent "two-equations" model, which is further approximated by a linear model. The eigenvalues of the linear system are used to decide about the system stability. For error modeling and computing the order of accuracy in the numerical solution, we use Richardson criterion [38].

- Chapter 7 deals with a strategy to choose system parameters for non-zero boundary fluxes of mass and energy, without making the problem ill-posed. One-phase flow examples are also given, in this chapter.

- Chapter 8 comprises of conclusions and further work.

Chapter 2

Elementary 1D flow systems and time integration schemes

In this chapter, we set the foundations of the actual model of a flow system, which is discussed in the later chapters of the thesis. We start with a stationary linear flow system and the finite element method (FEM) to solve it. In the second example, a dynamic convection diffusion equation is solved by applying various time integration methods. Later on, the Burgers equation and a nonlinear model consisting of coupled partial differential equations (PDEs) is discussed.

2.1 Convection diffusion problem

We consider a unit line segment as the domain of computation i.e., $\Omega = (0, 1)$. The problem is defined as

$$-D\frac{d^2u}{dx^2} + v\frac{du}{dx} = q(x), \quad x \in \Omega, \; u \in C^2(\Omega) \cap C^1(\overline{\Omega}), \tag{2.1}$$

$$u(0) = 2, \; u(1) = 1,$$

where $\overline{\Omega} = [0, 1]$, v is the speed of the wave (i.e., the medium), D is the diffusion coefficient, and $q(x)$ is a source term. Both coefficients, v and D, are assumed to be constant. The solution $u(x)$ could represent temperature or some other physical quantity. In this case, we use Dirichlet boundary conditions.

2.1.1 Standard Galerkin Algorithm

In order to solve this equation numerically, we apply the standard Galerkin approach. Of course it can be solved by finite differences, but the purpose here is to develop the

methods we applied for the actual model (given in the chapters later on). Multiply Equation (2.1) by a test function $\phi \in L^2(\Omega)$ and integrate over Ω to obtain

$$-D \int_\Omega \frac{d^2u}{dx^2}\phi(x)dx + v \int_\Omega \frac{du}{dx}\phi(x)dx = \int_\Omega q(x)\phi(x)dx. \qquad (2.2)$$

By applying integration by parts, we get

$$-D\left[\frac{du}{dx}\phi(x)\right]_0^1 + D \int_\Omega \frac{du}{dx}\frac{d\phi}{dx}dx + v \int_\Omega \frac{du}{dx}\phi(x)dx = \int_\Omega q(x)\phi(x)dx. \qquad (2.3)$$

In the above equation, one determines $u \in H^1(\Omega)$ with $u(0) = 2$ and $u(1) = 1$ such that Equation (2.3) holds for all $\phi \in H_0^1(\Omega)$. Here

$$H^1(\Omega) := \left\{\phi \in L^2(\Omega) \ \middle| \ \frac{d\phi}{dx} \in L^2(\Omega)\right\},$$

and

$$H_0^1(\Omega) := \left\{\phi \in H^1(\Omega) \mid \phi(0) = \phi(1) = 0\right\}.$$

We divide Ω into small segments of length Δx and solve the given equation on N vertices of these segments represented by x_j, where $j = 1, 2, .., N$ and $\Delta x = \frac{1}{N-1}$. The solution u is approximated by a combination of discrete solution values u_j and a set of basis functions ϕ_j, i.e.,

$$u(x) \approx \sum_{j=1}^N u_j\phi_j(x), \quad x \in \Omega,$$

where $u_1 = u(0) = 2$ and $u_N = u(1) = 1$ are known and for ϕ_j, we use piecewise linear functions [16]. It is important to note that

$$\phi_i(x_j) = \delta_{ij},$$

where δ is the Kronecker delta function. The test function ϕ is also chosen from the set of basis functions, hence

$$\phi = \phi_i, \ i = \{2, .., N - 1\}.$$

Since $i \neq 0$ and $i \neq N$, we have $\phi(0) = \phi(1) = 0$, which makes the first term in (2.3) equal to zero. Upon substitution of ϕ and u by ϕ_i and their approximate values, respectively, Equation (2.3) can be written as,

$$D \sum_{j=1}^N u_j \int_\Omega \frac{d\phi_i}{dx}\frac{d\phi_j}{dx}dx + v \sum_{j=1}^N u_j \int_\Omega \phi_i \frac{d\phi_j}{dx}dx = \int_\Omega q\phi_i dx, \ i = 2, 3, ..., N - 1.$$

We have $N - 2$ equations, which is equal to the number of unknown values u_j. Now, bringing all the known values to the right hand side of the above equation, we obtain

$$D \sum_{j=2}^{N-1} u_j \int_\Omega \frac{d\phi_i}{dx}\frac{d\phi_j}{dx}dx + v \sum_{j=2}^{N-1} u_j \int_\Omega \phi_i \frac{d\phi_j}{dx}dx = -Du_1 \int_\Omega \frac{d\phi_1}{dx}\frac{d\phi_i}{dx}dx$$

$$-vu_1 \int_\Omega \phi_i \frac{d\phi_1}{dx}dx - Du_N \int_\Omega \frac{d\phi_N}{dx}\frac{d\phi_i}{dx}dx - vu_N \int_\Omega \phi_i \frac{d\phi_N}{dx}dx + \int_\Omega q\phi_i dx.$$

This equation can be represented by an equivalent matrix equation

$$S\boldsymbol{u} = \boldsymbol{f}, \tag{2.4}$$

where the stiffness matrix S (of dimension $N - 2 \times N - 2$) and the vector $\boldsymbol{f}$ are given by

$$S_{ij} = D \int_{\Omega} \frac{d\phi_i}{dx} \frac{d\phi_j}{dx} dx + v \int_{\Omega} \phi_i \frac{d\phi_j}{dx} dx,$$

$$f_i = -Du_1 \int_{\Omega} \frac{d\phi_1}{dx} \frac{d\phi_i}{dx} dx - vu_1 \int_{\Omega} \phi_i \frac{d\phi_1}{dx} dx$$

$$- Du_N \int_{\Omega} \frac{d\phi_N}{dx} \frac{d\phi_i}{dx} dx - vu_N \int_{\Omega} \phi_i \frac{d\phi_N}{dx} dx + \int_{\Omega} q\phi_i dx,$$

where $\boldsymbol{u}$ is the numerical solution vector with dimension $N-2$. The following Newton-Cotes quadrature rule is used for all $1D$ numerical integrations

$$\int_a^b f(x)dx \approx \frac{b-a}{2} \left[f(a) + f(b) \right].$$

We use a direct solver in order to solve Equation (2.4). The numerical solution of Equation (2.1) (represented by $\boldsymbol{u}^{(1)}$) is given in Figure 2.1(a) for $D = 1$ and $v = 1$. The analytical solution of this problem is given by

$$u^{(2)} = \frac{1}{1 - e^m}(e^{mx} - e^m), \ m = \frac{v}{D}.$$

In Figure 2.1(b), the relative difference, $\Delta\boldsymbol{u}$, between $\boldsymbol{u}^{(1)}$ and $\boldsymbol{u}^{(2)}$ is plotted. It is defined as

$$\Delta\boldsymbol{u} = \frac{\left|\boldsymbol{u}^{(1)} - \boldsymbol{u}^{(2)}\right|}{\|\boldsymbol{u}^{(2)}\|}, \quad \text{where } \|\boldsymbol{u}^{(2)}\| = \sqrt{\frac{1}{N} \sum_{i=1}^{N} \left(u_i^{(2)}\right)^2}. \tag{2.5}$$

The graph indicates that the maximum relative error increases polynomially with Δx.

In another test example, we take $D = 0.1$ and $v = 4$ (a convection dominant case). The plot of the numerical solution is provided in Figure 2.1(c) along with the analytical solution. The wiggles in the numerical solution are a result of the large Peclet number ($\frac{v}{D}\Delta x$). To reduce these wiggles, the Streamline Upwind Petrov-Galerkin method can be used.

2.1.2 Streamline Upwind Petrov-Galerkin

In this method, a modified test function is used,

$$w = \phi + \psi,$$

where ϕ is the classical test function. The additional term ψ introduces artificial diffusion and hence counters the convection dominance. This idea is taken from the
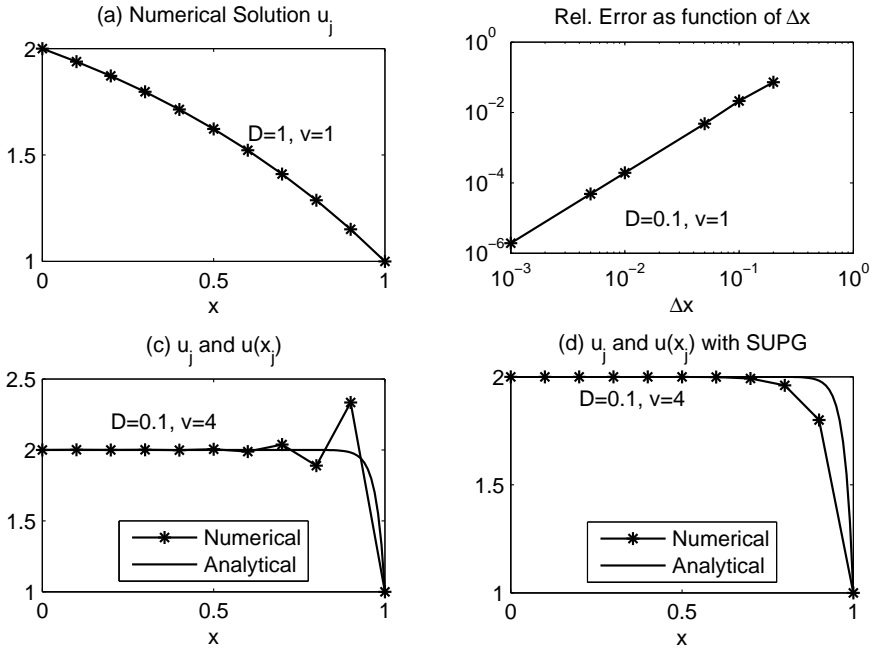
Figure 2.1: Steady-state convection-diffusion equation. (a) Numerical solution u_j by SGA with $D = 1$, $v = 1$, $\Delta x = 0.1$, and $q = 0$. (b) Relative difference between numerical and analytical solutions, defined by Equation (2.5). (c) Plots of u_j by SGA and $u(x)$ with $D = 0.1$ and $v = 4$. (d) Plots of u_j by SUPG and $u(x)$ with $D = 0.1$ and $v = 4$.

finite difference method [18]. We discretize the diffusion term in Equation (2.1) by the central difference and the convection term by a backward difference scheme, and get

$$-D\left[\frac{u_{i+1} - 2u_i + u_{i-1}}{(\Delta x)^2} + O(\Delta x)^2\right] + v\left[\frac{u_i - u_{i-1}}{\Delta x} + \frac{\Delta x}{2}\frac{d^2u}{dx^2} + O(\Delta x)^2\right] = q_i, \quad (2.6)$$

where we use Taylor series expansions, such as

$$u(x + \Delta x) = u_{i-1} = u(x) + \Delta x\frac{du}{dx} + \frac{(\Delta x)^2}{2!}\frac{d^2u}{dx^2} + ...O(\Delta x^3),$$

$$u(x - \Delta x) = u_{i-1} = u(x) - \Delta x\frac{du}{dx} + \frac{(\Delta x)^2}{2!}\frac{d^2u}{dx^2} - ...O(\Delta x^3)$$

Equation (2.6) shows that a $O(\Delta x)^2$ accurate backward difference of convection term introduces a diffusion of magnitude $v\frac{\Delta x}{2}\frac{d^2u}{dx^2}$. Elimination of spurious oscillations in the solution (in finite difference) by this technique motivates us to use a similar factor in

finite elements (FEM is otherwise equivalent to central difference for simple meshes). The value of ψ is given by

$$\psi(x) = sign(v)\frac{\Delta x}{2}\frac{d\phi}{dx}\xi.$$

For a first order upwind, we have $\xi = 1$. Hence,

$$w = \phi + sign(v)\frac{\Delta x}{2}\frac{d\phi}{dx}.$$

Using w with $\xi = 1$ and $\phi = \phi_i$ in Equation (2.2) instead of ϕ and repeating the steps for discretization of Equation (2.1), we arrive at a similar matrix equation as in Equation (2.4)

$$S\boldsymbol{u} = \boldsymbol{f},$$

with

$$S_{ij} = D\int_{\Omega}\frac{d\phi_i}{dx}\frac{d\phi_j}{dx}dx + v\int_{\Omega}\frac{d\phi_j}{dx}\left(\phi_i + \frac{\Delta x}{2}\frac{d\phi_i}{dx}\right)dx,$$

$$f_i = -Du_1\int_{\Omega}\frac{d\phi_1}{dx}\frac{d\phi_i}{dx}dx - vu_1\int_{\Omega}\frac{d\phi_1}{dx}\left(\phi_i + \frac{\Delta x}{2}\frac{d\phi_i}{dx}\right)dx - Du_N\int_{\Omega}\frac{d\phi_N}{dx}\frac{d\phi_i}{dx}dx$$

$$- vu_N\int_{\Omega}\frac{d\phi_N}{dx}\left(\phi_i + \frac{\Delta x}{2}\frac{d\phi_i}{dx}\right)dx + \int_{\Omega}q\phi_idx.$$

The additional term $sign(v)\frac{\Delta x}{2}\frac{d\phi}{dx}$ is effective only in the convection part since the elementwise derivative of ψ is zero. The solution of Equation (2.1) by using the $SUPG$ method is shown in Figure 2.1(d) together with the analytical solution $u(x) = \frac{1}{1-e^m}(e^{mx}-e^m)$, where $m = \frac{v}{D}$. Again, we used $D = 0.1$, $v = 4$, but with the test function w. We observe that the numerical solution in this case is smooth but it deviates from the analytical solution, where u varies sharply. This clipping effect is due to the artificial diffusion term and it can be reduced by taking a finer mesh since $\boldsymbol{u} \to u$ as $\Delta x \to 0$. Again, a finer mesh means that extra memory and more computational time is required. For the current problem, a finer mesh can also be used for the standard Galerkin method to remove the spurious oscillations.

2.2 Solution of a transient convection diffusion equation

Consider the following time-dependent convection-diffusion equation, along with the initial value and boundary conditions

$$\frac{\partial u}{\partial t} + v\frac{\partial u}{\partial x} - D\frac{\partial^2 u}{\partial x^2} = q, \quad x \in \Omega,\ t \in \mathbb{R}^+, \tag{2.7}$$

$$u(0, t) = 1, \ u(1, t) = (2 - t), \ u(x, 0) = \frac{1}{e - 1}(e^x - 1) + 1.$$

The unknown variable $u(x, t)$ in this case is a function of time and space. All other constants have the same definitions as given in the previous example. We solve this equation over a unit line segment for $t \in (0, 1]$. After multiplying Equation (2.7) by a test function ϕ of our choice and integrating over the problem domain, we get the weak formulation $\in L^2(\Omega)$

$$\int_\Omega \frac{\partial u}{\partial t} \phi dx + v \int_\Omega \frac{\partial u}{\partial x} \phi dx - D \int_\Omega \frac{\partial^2 u}{\partial x^2} \phi dx = \int_\Omega q \phi dx. \tag{2.8}$$

We have $\phi(0) = \phi(1) = 0$, therefore the boundary term vanishes. The problem domain is divided into $N - 1$ elements as explained in the previous section. The spatial discretization of $u(x, t)$ is done as follows

$$u(x, t) \approx \sum_{j=1}^N u_j(t) \phi_j(x), \quad \text{where } u_1(t) \text{ and } u_N(t) \text{ are given.}$$

After using the approximate values of $u(x, t)$ in the weak formulation, we get

$$\sum_{j=1}^N \frac{du_j}{dt} \int_\Omega \phi_i \phi_j dx + v \sum_{j=1}^N u_j \int_\Omega \frac{d\phi_j}{dx} \phi_i dx - D \sum_{j=1}^N u_j \int_\Omega \frac{d\phi_i}{dx} \frac{d\phi_j}{dx} dx$$

$$= \int_\Omega q \phi_i dx, \quad i = 2, 3, .., N - 1.$$

Taking all the known terms to the right hand side of this equation, we have

$$\sum_{j=2}^{N-1} \frac{du_j}{dt} \int_\Omega \phi_i \phi_j dx + v \sum_{j=2}^{N-1} u_j \int_\Omega \frac{d\phi_j}{dx} \phi_i dx - D \sum_{j=2}^{N-1} u_j \int_\Omega \frac{d\phi_i}{dx} \frac{d\phi_j}{dx} dx = \int_\Omega q \phi_i dx$$

$$- v u_1 \int_\Omega \frac{d\phi_1}{dx} \phi_i dx - v u_N \int_\Omega \frac{d\phi_N}{dx} \phi_i dx - D u_1 \int_\Omega \frac{d\phi_1}{dx} \frac{d\phi_i}{dx} dx - D u_N \int_\Omega \frac{d\phi_N}{dx} \frac{d\phi_i}{dx} dx.$$

This equation can be written in a matrix form

$$M \frac{d\boldsymbol{u}}{dt} = -S \boldsymbol{u} + \boldsymbol{f}, \tag{2.9}$$

where the ijth element of the mass matrix M is given by

$$M_{ij} = \int_\Omega \phi_i \phi_j dx.$$

Similarly, the stiffness matrix S and the vector $\boldsymbol{f}$ are defined as

$$S_{ij} = v \int_\Omega \frac{d\phi_j}{dx} \phi_i dx + D \int_\Omega \frac{d\phi_i}{dx} \frac{d\phi_j}{dx} dx,$$

$$f_i = \int_\Omega q \phi_i dx - v u_1 \int_\Omega \frac{d\phi_1}{dx} \phi_i dx - v u_N \int_\Omega \frac{d\phi_N}{dx} \phi_i dx$$

$$- D u_1 \int_\Omega \frac{d\phi_1}{dx} \frac{d\phi_i}{dx} dx - D u_N \int_\Omega \frac{d\phi_N}{dx} \frac{d\phi_i}{dx} dx.$$

2.2.1 Forward Euler time integration

We divide the time domain into equal intervals of duration Δt and represent the time instances $0,\ \Delta t,\ 2\Delta t,\ 3\Delta t, ...$ by $\tau = 0,\ 1,\ 2,\ 3, ...$ Now, by applying Forward Euler scheme for the time derivative term, we obtain

$$M\frac{\boldsymbol{u}^\tau - \boldsymbol{u}^{\tau-1}}{\Delta t} = -S\boldsymbol{u}^{\tau-1} + \boldsymbol{f}^{\tau-1}, \quad \tau \geq 1. \tag{2.10}$$

Note that $\boldsymbol{u}^{\tau-1}$ is already computed in the previous iteration. This time-discretization scheme is called *explicit*. The mass matrix M is a band matrix in this case (even for higher dimensional problems), and hence its inversion is cheap. However, in the explicit scheme we are faced with a stability condition. Let α be an eigenvalue of $I - \Delta t M^{-1}S$, then Δt should be chosen such that,

$$|\alpha| \leq 1, \quad \forall\, \alpha,$$

otherwise we will have an unstable result. For a stable solution, the value of Δt is bounded by the inequality

$$\Delta t < \min\left(\frac{\Delta x^2}{D}, \frac{\Delta x}{v}\right), \tag{2.11}$$

where Δx is the grid size. For the current example, we have, $\Delta x = 0.1$, $\Delta t = 0.01$, $N = 11$, $D = 1$, $q = 0$, $u(0,t) = 1$, $u(1,t) = (2 - t)$, $u(x,0) = \frac{e}{e-1}(1 - e^{-x}) + 1$. The result is shown in Figure 2.2.
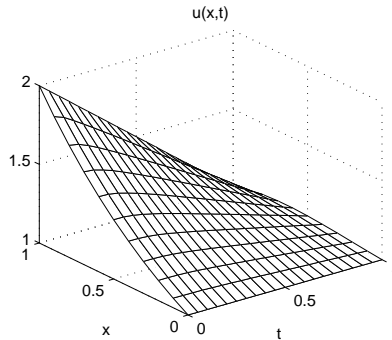
Figure 2.2: The numerical solution of the time dependent convection-diffusion equation by SGA, $D = 1$, $v = 1$, $u(0,t) = 1$, $u(1,t) = (2 - t)$, $u(x,0) = \frac{1}{e-1}(e^x - 1) + 1$

2.2.2 Backward Euler time integration

If we use Backward Euler scheme for Equation (2.10), we have

$$M\frac{\boldsymbol{u}^\tau - \boldsymbol{u}^{\tau-1}}{\Delta t} = -S\boldsymbol{u}^\tau + \boldsymbol{f}^\tau.$$

An advantage of the implicit method is that it is unconditionally stable.

2.3   Numerical solution of Burgers' equation

Consider the following non-linear equation, also called Burgers' equation with viscosity,

$$\frac{\partial u}{\partial t} + u\frac{\partial u}{\partial x} - D\frac{\partial^2 u}{\partial x^2} = q, \quad x \in (0,1),\ t \in (0,1]. \tag{2.12}$$

The initial value and boundary conditions are mentioned as

$$u(0,t) = \frac{1}{1 + \exp\left(\frac{-t}{4D}\right)}, \quad u(1,t) = \frac{1}{1 + \exp\left(\frac{1-\frac{t}{2}}{2D}\right)}, \quad \text{(boundary conditions)},$$

$$u(x,0) = \frac{1}{1 + \exp\left(\frac{x}{2D}\right)}, \quad \text{(initial value)}.$$

In this case, the difficult part is the convection term. Among many time integration schemes, we mention three of them. By using Euler forward method (i.e., explicit method), we have

$$\frac{u^\tau - u^{\tau-1}}{\Delta t} + u^{\tau-1}\frac{du^{\tau-1}}{dx} - D\frac{d^2u^{\tau-1}}{dx^2} = q, \quad x \in (0,1),\ \tau = 1,2,...,\tau_{max}, \tag{2.13}$$

where $\tau_{max} = \frac{t_p}{\Delta t}$ and t_p is the process time. We can use Equation (2.11) to estimate Δt, assuming that we have some idea about maximum value of u.

In another choice, we take all solution variables u at the current time index τ except for the coefficient u that appears outside the derivative term in the convective part, i.e.,

$$\frac{u^\tau - u^{\tau-1}}{\Delta t} + u^{\tau-1}\frac{du^\tau}{dx} - D\frac{d^2u^\tau}{dx^2} = q, \quad x \in (0,1), \tag{2.14}$$

which is a combination of implicit and explicit terms and called an *IMEX* (*IMplicit EXplicit*) time integration scheme. An estimate for the stability condition in this case is relaxed to $\Delta t < \frac{\Delta x}{u}$. For a detailed numerical solution procedure of Equations (2.13) and (2.14), we refer to [5].

Secondly, we take all u in Equation (2.12), outside the time differencing, at current time index τ (fully implicit scheme) and consider an additional index p (e.g., for Picard iteration). Hence we realize

$$\frac{u^{\tau,p} - u^{\tau-1}}{\Delta t} + u^{\tau,p-1}\frac{du^{\tau,p}}{dx} - D\frac{d^2u^{\tau,p}}{dx^2} = q, \quad x \in (0,1), \tag{2.15}$$

The convection term is linearized by taking the coefficient u at the previous Picard iteration. Picard iteration is used to solve non-linear equations written (for example) in the form,

$$\boldsymbol{u}^p = F(\boldsymbol{u}^{p-1}). \tag{2.16}$$

From a programming point of view, this gives an inner iteration loop at each time step and $\boldsymbol{u}^1$ starts with an initial guess. We calculate $\boldsymbol{u}^p$ by using Equation (2.16). The

value of $\boldsymbol{u}^p$ as computed in the current Picard iteration is used as $\boldsymbol{u}^{p-1}$ in the next Picard iteration. This procedure goes on until a stopping condition is satisfied. The iteration stops successfully if (for example) the infinity norm of $\boldsymbol{e}^p = \frac{\|\boldsymbol{u}^p - \boldsymbol{u}^{p-1}\|}{\|\boldsymbol{u}^p\|}$, is less than a specified value, i.e.,

$$\boldsymbol{e}^p_\infty < \delta,$$

where δ is an acceptable error level. In this case we move on to the next time step. If this condition is not met within a specified number of iterations or $\boldsymbol{u}^p \to \infty$, the Picard iteration stops unsuccessfully, i.e., we do not have a converged solution. Equation (2.16) can be formulated in many ways. If it is divergent in one form, it might converge in another form. For the current time dependent problem, we use $\boldsymbol{u}^{\tau-1}$ as the initial guess in the first Picard iteration for $\boldsymbol{u}^{\tau,1}$.

Theorem 2.3.1. *(BANACH FIXED-POINT THEOREM) Assume that K is a nonempty closed set in a Banach space V, and further, that $T : K \to K$ is a contractive mapping with contractivity constant α, $0 \le \alpha < 1$. Then the following results hold*

(1) Existence and uniqueness: There exists a unique $u \in K$ such that

$$u = T(u)$$

(2) Convergence and error estimates of the iteration: For any $u_0 \in K$, the sequence $u_n \subset K$ defined by $u_{n+1} = T(u_n)$, $n = 0, 1, ...$, converges to u:

$$\|u_n - u\|_V \to 0 \ \text{as } n \to \infty.$$

For the error, the following bounds are valid:

$$\|u_n - u\|_V \le \frac{\alpha^n}{1 - \alpha}\|u_0 - u_1\|_V,$$

$$\|u_n - u\|_V \le \frac{\alpha}{1 - \alpha}\|u_{n-1} - u_n\|_V,$$

$$\|u_n - u\|_V \le \alpha\|u_{n-1} - u\|_V.$$

For a proof of the above theorem, we refer to [28]. The weak formulation of Equation (2.15) is written as

$$\int_\Omega \frac{u^{\tau,p} - u^{\tau-1}}{\Delta t}\phi(x)dx + \int_\Omega u^{\tau,p-1}\frac{du^{\tau,p}}{dx}\phi(x)dx - D\int_\Omega \frac{d^2u^{\tau,p}}{dx^2}\phi dx = \int_\Omega q\phi dx,$$

The approximations $u^\tau \approx \sum_{j=1}^N u_j^\tau \phi_j$ and $\phi = \phi_i$ lead to an equivalent matrix equation

$$M\boldsymbol{u}^{\tau,p} + \Delta t S \boldsymbol{u}^{\tau,p} = M\boldsymbol{u}^{\tau-1} + \Delta t\boldsymbol{f} + \Delta t\boldsymbol{q}, \tag{2.17}$$

where $S = S(u^{\tau,p-1})$ and $f = f(u^{\tau,p-1})$. Now, the global matrices and vectors at (τ, p) are defined as

$$M_{ij} = \int_\Omega \phi_i \phi_j dx, \quad i, j = \{2, 3, .., N-1\},$$

$$S_{ij} = \int_\Omega u^{\tau,p-1} \phi_l \frac{d\phi_j}{dx} \phi_i dx + D \int_\Omega \frac{d\phi_i}{dx} \frac{d\phi_j}{dx} dx,$$

$$f_i = \int_\Omega u^{\tau-1} \phi_i dx - u_1^\tau \int_\Omega u^{\tau,p-1} \frac{d\phi_1}{dx} \phi_i dx - Du_1^\tau \int_\Omega \frac{d\phi_1}{dx} \frac{d\phi_i}{dx} dx$$

$$- u_N^\tau \int_\Omega u^{\tau,p-1} \frac{d\phi_N}{dx} \phi_i dx - Du_N^\tau \int_\Omega \frac{d\phi_N}{dx} \frac{d\phi_i}{dx} dx, \quad i = \{2, 3, .., N-1\},$$

$$q_i = \int_\Omega q\phi_i dx.$$

Again, Equation (2.17) is solved by a direct solver. The solution plot u is provided
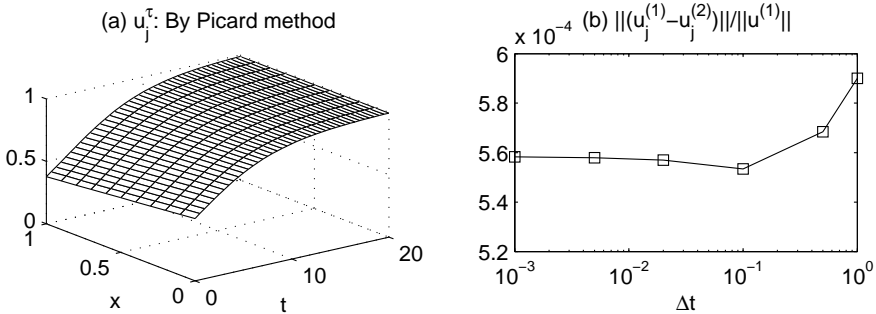
Figure 2.3: Numerical solution of the Burgers equation with $\Delta x = 0.1$, $\Delta t = 0.01$, $D = 1$, $q(x,t) = 0$. (a) The plot of $u(x,t)$ by Picard method and (b) a plot of $\max \frac{\|u_j^{(2)} - u_j^{(1)}\|}{\|u_j\|}$, as function of Δt, where $u^{(1)}$ is obtained by the Picard method and $u^{(2)}$ is the analytical solution.

in Figure 2.3(a). The analytical solution of Equation (2.12), with no source term, is given by [29],

$$u(x,t) = \frac{1}{1 + \exp\left(\frac{x - \frac{t}{2}}{2D}\right)}, \tag{2.18}$$

Figure 2.3(b) shows $\left|\frac{u_{j,2} - u_{j,1}}{u_{j,2}}\right|_\infty$ as function of Δt, where u_1 is obtained by the Picard method and u_2 is determined from Equation (2.18). The maximum relative error should increases linearly for $\Delta t > 0.1$. However, the error contributed by the spatial discretization dominates for a small Δt. In Chapter 6, we use Richardson extrapolation for error estimation.

2.4   A system of non-linear equations

In this section, we consider a hypothetical fluid flow system through a porous medium on a domain Ω (a unit line segment). We aim at solving the system numerically for the variables such as density ρ, specific enthalpy h, velocity v, pressure P, and temperature T. The model is given by the following relations.
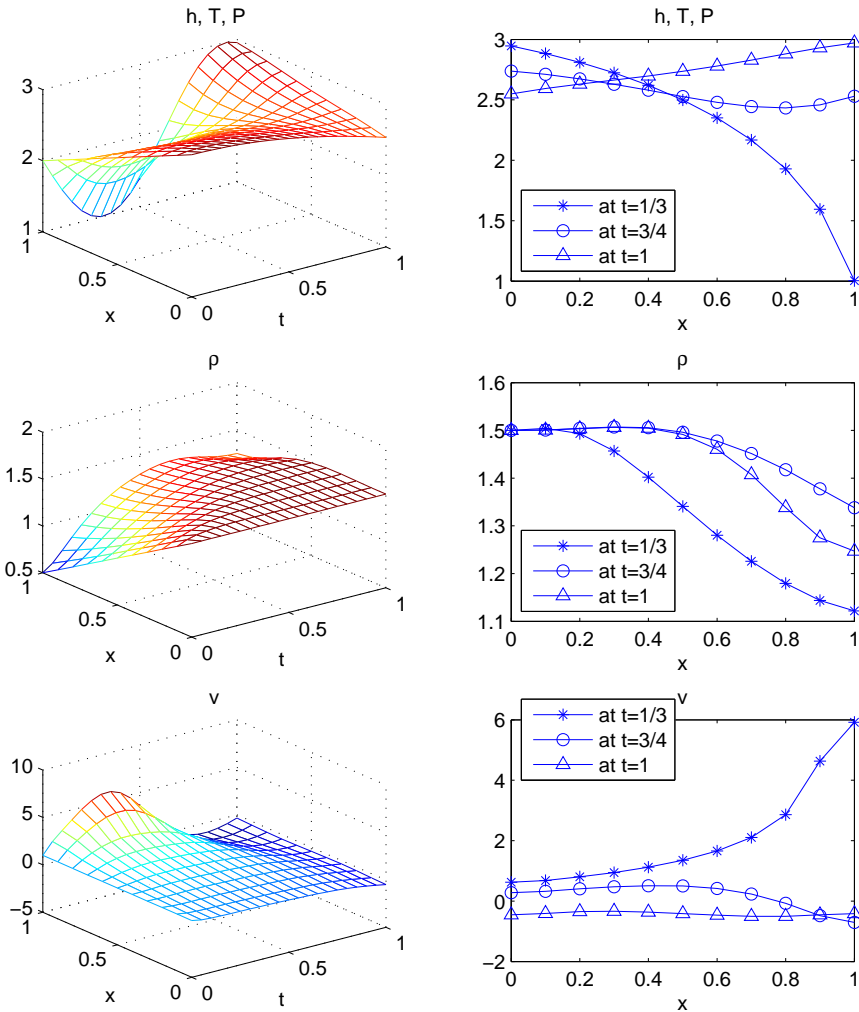
Figure 2.4: The plots of the solution variables $P = T = h$, ρ, and v.

$$\frac{\partial \rho}{\partial t} + \frac{\partial(\rho v)}{\partial x} = 0, \quad x \in \Omega, \; t > 0, \tag{2.19}$$

$$\frac{\partial(\rho h)}{\partial t} + \frac{\partial(\rho h v)}{\partial x} - D_1 \frac{\partial^2 T}{\partial x^2} = q(x, t), \tag{2.20}$$

$$v(x, t) + \frac{K}{\mu} \frac{\partial P}{\partial x} = 0, \tag{2.21}$$

$$P(x, t).V = RT(x, t), \tag{2.22}$$

$$h(x, t) = cT(x, t), \tag{2.23}$$

where K is the permeability, μ is the viscosity, V is the volume and c is a given constant. Initial value and boundary conditions are mentioned later. We choose values of the constants in such a way that $h = T = P$. The system consists of the mass conservation law (2.19), energy conservation law (2.20), Darcy's law (2.21), ideal gas law (2.22), and a connecting relation between temperature T and specific enthalpy h. The original model is given in [12]. By using the last three equations, we eliminate v, T, and P in Equations (2.19) and (2.20). Furthermore, the value of $\frac{\partial \rho}{\partial t}$ is used from Equation (2.19) into Relation (2.20). The system of five relations is transformed into the following two *PDE*s. Therefore, we have

$$\frac{\partial \rho}{\partial t} - \frac{\partial h}{\partial x} \frac{\partial \rho}{\partial x} - \rho \frac{\partial^2 h}{\partial x^2} = 0, \tag{2.24}$$

$$\rho \frac{\partial h}{\partial t} - \rho \frac{\partial h}{\partial x} \frac{\partial h}{\partial x} - \frac{\partial^2 h}{\partial x^2} = q(x, t). \tag{2.25}$$

The initial values and the boundary conditions are given by,

$$h(x, 0) = 3 - x, \; h(0, t) = 2 + \sin(5t), \; h(1, t) = 2 + \cos(t),$$
$$\rho(x, 0) = 1.5 - x, \; \rho(0, t) = 1.5. \tag{2.26}$$

We integrate this system in time by Euler Backward with a Picard iteration for dealing with the nonlinearity. This gives

$$\frac{\rho^{\tau,p} - \rho^{\tau-1}}{\Delta t} - \frac{dh^{\tau,p-1}}{dx} \frac{d\rho^{\tau,p}}{dx} - \rho^{\tau,p} \frac{d^2 h^{\tau,p-1}}{dx^2} = 0, \tag{2.27}$$

$$\rho^{\tau,p-1} \frac{h^{\tau,p} - h^{\tau-1}}{\Delta t} - \rho^{\tau,p-1} \frac{dh^{\tau,p-1}}{dx} \frac{dh^{\tau,p}}{dx} - \frac{d^2 h^{\tau,p}}{dx^2} = q^\tau(x), \tag{2.28}$$

where p is the Picard iteration index. Now, the approximations $\rho^\tau(x) \approx \sum_{j=1}^{N} \rho_j^\tau \phi_j$, $h^\tau(x) \approx \sum_{j=1}^{N} h_j^\tau \phi_j$, and $w(x) = \phi_i + \frac{\Delta x}{2} \frac{d\phi_i}{dx}$ leads to write Equations (2.27) and (2.28) into the following matrix equations.

$$M^{(1)} \boldsymbol{\rho}^{\tau,p} + \Delta t S^{(1)} \boldsymbol{\rho}^{\tau,p} = M^{(1)} \boldsymbol{\rho}^{\tau-1} + \Delta t \boldsymbol{f}^{(1)}, \tag{2.29}$$

$$M^{(2)} \boldsymbol{h}^{\tau,p} + \Delta t S^{(2)} \boldsymbol{h}^{\tau,p} = M^{(2)} \boldsymbol{h}^{\tau-1} + \Delta t \boldsymbol{f}^{(2)} + \Delta t \boldsymbol{q}, \tag{2.30}$$

where global matrices, in general, are computed at $u^{\tau,p-1}$ and $h^{\tau,p-1}$. Hence, we have

$$M^{(1)}_{ij} = \int_\Omega \phi_i \phi_j dx, \quad i,j = 2,3,..,N-1,$$

$$S^{(1)}_{ij} = -\int_\Omega \frac{dh^{\tau,p-1}}{dx} \frac{d\phi_j}{dx}\left(\phi_i + \frac{\Delta x}{2}\frac{d\phi_i}{dx}\right)dx,$$

$$f^{(1)}_i = -\rho^\tau_0 \int_\Omega \frac{dh^{\tau,p-1}}{dx}\frac{\phi_0}{dx}\left(\phi_i + \frac{\Delta x}{2}\frac{d\phi_i}{dx}\right)dx$$

$$\quad -\rho^\tau_N \int_\Omega \frac{dh^{\tau,p-1}}{dx}\frac{\phi_N}{dx}\left(\phi_i + \frac{\Delta x}{2}\frac{d\phi_i}{dx}\right)dx, \quad i = 2,3,..,N-1,$$

$$M^{(2)}_{ij} = \int_\Omega \rho^{\tau,p-1}\phi_i\phi_j dx,$$

$$S^{(2)}_{ij} = -\int_\Omega \rho^{\tau,p-1}\frac{dh^{\tau,p-1}}{dx}\frac{d\phi_j}{dx}\phi_i dx - \int_\Omega \frac{d\phi_i}{dx}\frac{d\phi_j}{dx}dx,$$

$$f^{(2)}_i = h^\tau_0 \int_\Omega \rho^{\tau,p-1}h^{\tau,p-1}\frac{\phi_0}{dx}\phi_i dx - h^\tau_0 \int_\Omega \frac{\phi_1}{dx}\frac{d\phi_i}{dx}dx$$

$$\quad + h^\tau_N \int_\Omega \rho^{\tau,p-1}h^{\tau,p-1}\frac{\phi_N}{dx}\phi_i dx - h^\tau_N \int_\Omega \frac{\phi_N}{dx}\frac{d\phi_i}{dx}dx,$$

$$q_i = \int_\Omega q\phi_i dx.$$

The solution plots of the unknown variables are given in Figure 2.4. At $t = 0$, the velocity is positive for the entire spatial domain and hence the boundary condition mentioned for the convection equation at $x = 0$ is consistent. At $t = 3/4$, the velocity is positive (left to right) at $x = 0$ but it is negative (right to left) at $x = 1$. In such cases, boundary conditions are required at both $x = 0$ and $x = 1$, at the same time. At $t = 1$, the velocity plot suggests that the boundary condition is necessary and allowable at $x = 1$ only.

2.4.1 Characteristics of a hyperbolic partial differential equation

In the this section, a hyperbolic differential equation appears in our mathematical model. The mass conservation law as given in the following equation (along with initial and boundary conditions) can be used to determine a one dimensional mass flow within the fluid system and across the boundaries.

$$\frac{\partial\rho}{\partial t} + \frac{\partial(\rho v)}{\partial x} = 0, \qquad\qquad x \in \Omega,\ t > 0. \tag{2.31}$$

In Figure 2.5, three sets of characteristics are shown using various velocity profiles. Characteristics shown in Figure 2.5(b) corresponds to the velocity given in 2.5(a). Therefore the information (e.g., about $\rho(x,t)$) flows from the left boundary into the system. Hence, we are required to specify a boundary condition for ρ at the left boundary. The information is going out of the system from the right boundary which implies that we do not have to impose a boundary condition at this boundary.

Similarly, we specify a boundary condition for ρ at the right boundary for a case as given in Figure 2.5(c) and (d). In Figure 2.5(e) and (f), the system is acting as a source, for example due to initial conditions, and the information is going out of the system from both ends. Hence no boundary condition can be imposed in this case.
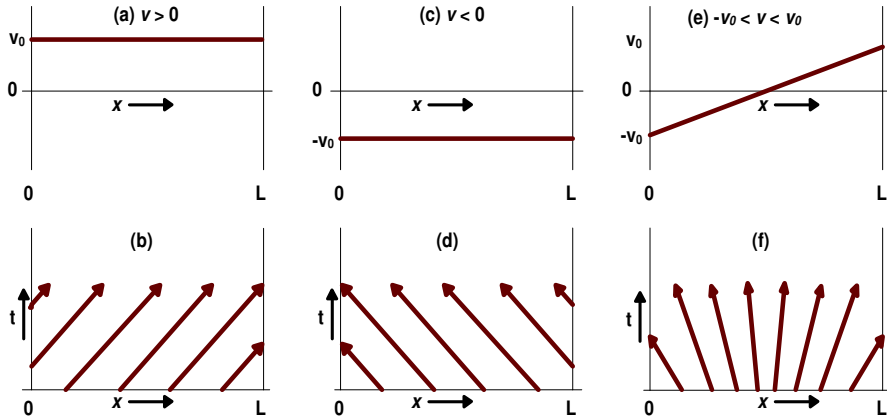
Figure 2.5: Plots of ρ characteristics using various velocity profiles, (b) information flowing towards right, (d) information flowing towards left, and (f) information is flowing outward from both ends.

3

The density enthalpy model in $1D$

In this chapter, we take a real model for the representation of a $1D$ flow system in porous medium. It is called numerical density-enthalpy method and is taken from [12]. The reasons to chose this model are mentioned in the introduction chapter. The numerical methods (e.g., FEM, $SUPG$, Picard iteration etc) as described in the previous chapter, are used to solve the $1D$ flow system in porous medium. The flow system is modeled by conservation laws, Darcy's law, and certain thermodynamic relations. The system of equations is solved for density and enthalpy. All other solution variables are computed from the pair (ρ, h). We attempted $IMEX$ and Picard methods to enable a reasonably large time step. However, $IMEX$ and Picard did not prove to be efficient and therefore we switched to Newton Raphson method in chapter 5.

3.1 Mathematical modeling

We consider a $1D$ fluid system in porous medium, where the medium is Propane (C_3H_8). We solve this system numerically for variables ρ, h, T, P, v, X_G, etc, over a unit line segment Ω. The mathematical model we consider is presented by the following equations.

$$\frac{\partial \rho}{\partial t} + \frac{\partial(\rho v)}{\partial x} = 0, \qquad x \in \Omega,\ t > 0, \qquad (3.1)$$

$$\frac{\partial(\rho h)}{\partial t} + \frac{\partial(\rho h v)}{\partial x} - \frac{\partial}{\partial x}\left(D\frac{\partial T}{\partial x}\right) = q, \qquad x \in \Omega,\ t > 0, \qquad (3.2)$$

$$v = -\frac{K}{\mu}\frac{\partial P}{\partial x}, \qquad\qquad x \in \Omega,\ t > 0, \qquad\qquad (3.3)$$

$$P = P(\rho, h), \qquad\qquad (3.4)$$

$$T = T(\rho, h), \qquad\qquad (3.5)$$

$$X_G = X_G(\rho, h), \qquad\qquad (3.6)$$

where X_G is the gas mass fraction. The density ρ is the average density of two phases. The specific enthalpy h also belongs to two phases (gas and liquid). Currently, we use only one component (Propane) and hence we assume that the velocity v is same for the both phases. In a later chapter, we included the gravity term in Darcy's law. Other variables have the same definitions as given in Section 2.4. The first three equations are the same as given by Equations (2.19) to (2.21). The last three relations indicate that T, P, and X_G are computed directly from (ρ, h), by using numerical ρ-h diagrams as discussed later. Computation of X_G is a post processing step. The dimensions of X_G are [k_g of gas/k_g of gas+liquid]. Now, the initial conditions are given by

$$\rho(x, 0) = \rho_0(x), \qquad\qquad x \in \Omega,$$

$$h(x, 0) = h_0(x), \qquad\qquad x \in \Omega. \qquad\qquad (3.7)$$

For *the mass equation*, the mass flux across the boundary is proportional to the difference in densities

$$\rho v = \epsilon k_m (\rho - \rho_a), \quad t > 0,\ x \in \{0, 1\}, \qquad\qquad (3.8)$$

$$\epsilon = \begin{cases} 1, & \text{if } x = 1, \\ -1, & \text{if } x = 0, \end{cases}$$

where k_m is a mass transfer coefficient and ρ_a is the ambient density. For *the energy equation*, the boundary condition corresponds to the energy transportation due to convection and diffusion and it is given by

$$-D\frac{\partial T}{\partial x} + (\rho h)v = \epsilon k_h (T - T_a) + \epsilon h_a k_m (\rho - \rho_a), \quad t > 0,\ x \in \{0, 1\}, \qquad (3.9)$$

where k_h is a heat transfer coefficient, h_a is the ambient enthalpy, and T_a is the ambient temperature.

3.1.1 Numerical density-enthalpy phase diagrams

We take the density (ρ) and the enthalpy (h) as state variables (primary variables) which means that temperature, pressure and mass fractions for various phases (secondary variables) can be computed (directly from ρ and h), once ρ and h are determined. The transformation from (ρ, h) to (T, P, X_G) is achieved through numerical ρ-h phase diagrams. These phase diagrams are constructed by Arendsen *at el.* They employed Peng/Robinson equation of state and Shomate equations (for enthalpy). In Figure 3.1, three such diagrams are shown for Propane (C_3H_8). In principle, such
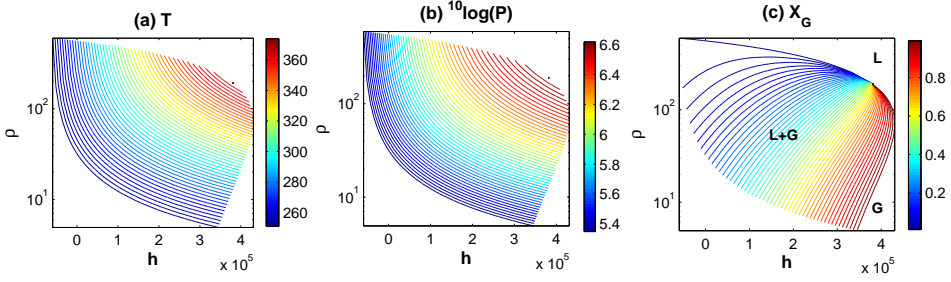
Figure 3.1: Numerical ρ-h diagrams. Plots of (a) isotherms, (b) isobars, and (c) constant gas mass fraction curves.

diagrams can be obtained through constrained minimization of the total Gibbs free energy as a function of temperature, pressure and mass distribution at given density and enthalpy. However, this approach is difficult to implement and requires large computation due to the amount of variables and discontinuities of the density and enthalpy as function of other variables (e.g., temperature, pressure, and mass fractions). In [2], the Gibbs free energy is minimized implicitly by determining the lines of equal chemical potential and the various phase equilibrium zones. In Figure 3.1(c), the liquid and gas phases are labeled as 'L' and 'G' respectively. The transitional zone (between liquid and gas phases) is marked with '$L + G$' which is noticeably larger than the 'L' and 'G' zones within the set of the used parameter values. Other phase diagrams for the transformation (T, X_G) to (ρ, h, P) are also available.

3.2 Linearization and Discretization

To solve this fluid system we use the streamline upwind Petrov-Galerkin (SUPG) method. We start the solution algorithm with the standard Galerkin algorithm and later extend it to SUPG.

3.2.1 Standard Galerkin algorithm for *the mass equation*

We use the IMEX method to linearize the mass equation

$$\frac{\rho^\tau - \rho^{\tau-1}}{\Delta t} + \frac{\partial(\rho^\tau v^{\tau-1})}{\partial x} = 0, \qquad x \in \Omega, \ \tau = \{1, 2, .., \tau_{max}\}. \qquad (3.10)$$

The corresponding weak formulation is given by

$$\int_\Omega \frac{\rho^\tau - \rho^{\tau-1}}{\Delta t} \phi dx + \int_\Omega \frac{\partial(\rho^\tau v^{\tau-1})}{\partial x} \phi dx = 0, \qquad (3.11)$$

where τ is a time index and $\tau_{max} = t_{max}/\Delta t$ and t_{max} is the process time [s]. Later on, we will discuss some delicate issues with respect to the time step. Applying integration

by parts to the integral on the right-hand side gives

$$\int_\Omega \frac{\rho^\tau - \rho^{\tau-1}}{\Delta t}\phi dx + \left[\rho^\tau v^{\tau-1}\phi\right]_0^1 - \int_\Omega \rho^\tau v^{\tau-1}\frac{d\phi}{dx}dx = 0. \tag{3.12}$$

Now the density $\rho^\tau(x)$ is approximated by the following expression

$$\rho^\tau(x) \approx \sum_{j=1}^N \rho_j^\tau \phi_j(x), \quad x \in \Omega, \tag{3.13}$$

where N is a number related to number of node points. We have N nodes and $N-1$ elements as a result of the spatial domain discretization. Now, substituting the value of $\rho^\tau(x)$ into Equation (3.12) along with $\phi = \phi_i$, $i = \{1, 2, .., N\}$.

$$\sum_{j=1}^N \left(\int_\Omega \phi_i\phi_j dx\right)\frac{\rho_j^\tau - \rho_j^{\tau-1}}{\Delta t} - \sum_{j=1}^N \left(\int_\Omega v^{\tau-1}\frac{d\phi_i}{dx}\phi_j dx\right)\rho_j^\tau - \rho_1^\tau v_1^{\tau-1}\delta_{1i} + \rho_N^\tau v_N^{\tau-1}\delta_{iN} = 0. \tag{3.14}$$

The linearized mass equation, as given by Relation (3.10) is hyperbolic in ρ. Therefore the corresponding boundary condition is used only for an inward velocity, i.e., when mass flows into the system, as explained in Section 2.4.1. In the case when velocity is outward, we do not use boundary conditions for a hyperbolic differential equation. By applying the boundary conditions as given by Equations (3.8) and (3.9), the boundary terms in the above equation can be written as

$$-\rho_1^\tau v_1^{\tau-1}\delta_{1i} + \rho_N^\tau v_N^{\tau-1}\delta_{iN} = \begin{cases} -\rho_1^\tau v_1^{\tau-1}\delta_{1i} & \text{if } v_1^{\tau-1} \le 0 \\ k_m(\rho_1^\tau - \rho_a)\delta_{1i} & \text{if } v_1^{\tau-1} > 0 \end{cases}$$
$$+ \begin{cases} \rho_N^\tau v_N^{\tau-1}\delta_{iN} & \text{if } v_N^{\tau-1} \ge 0 \\ k_m(\rho_N^\tau - \rho_a)\delta_{iN} & \text{if } v_N^{\tau-1} < 0 \end{cases}.$$

The matrix form of Equation (3.14) is given by

$$M^{(1)}\boldsymbol{\rho}^\tau + \Delta t S^{(1)}\boldsymbol{\rho}^\tau = M^{(1)}\boldsymbol{\rho}^{\tau-1} + \Delta t\boldsymbol{f}^{(1)}, \quad \tau = \{1, 2, .., \tau_{max}\}, \tag{3.15}$$

where $S^{(1)} = S^{(1)}(v^{\tau-1})$ and $\boldsymbol{f}^{(1)} = \boldsymbol{f}^{(1)}(v^{\tau-1})$ and they are defined as

$$S_{ij}^{(1)} = \int_\Omega v^{\tau-1}\frac{d\phi_i}{dx}\phi_j dx + \begin{cases} -v_1^{\tau-1}\delta_{1i} & \text{if } v_1^{\tau-1} \le 0 \\ k_m\delta_{1i} & \text{if } v_1^{\tau-1} > 0 \end{cases}$$
$$+ \begin{cases} v_N^{\tau-1}\delta_{iN} & \text{if } v_N^{\tau-1} \ge 0 \\ k_m\delta_{iN} & \text{if } v_N^{\tau-1} < 0 \end{cases},$$
$$f_i^{(1)} = \begin{cases} k_m\rho_a\delta_{1i} & \text{if } v_1^{\tau-1} > 0 \\ k_m\rho_a\delta_{iN} & \text{if } v_N^{\tau-1} < 0 \\ 0 & \text{otherwise} \end{cases}.$$

Equation (3.15) is solved by using a direct solver.

3.2.2   Standard Galerkin algorithm for *the energy equation*

The energy equation is also linearized by the *IMEX* method. It is given by

$$\frac{s^\tau - s^{\tau-1}}{\Delta t} + \frac{\partial(s^\tau v^{\tau-1})}{\partial x} = \frac{\partial}{\partial x}\left(D\frac{\partial T^{\tau-1}}{\partial x}\right) + q^\tau, \tag{3.16}$$

where $s^\tau = \rho^\tau h^\tau$. Although the energy equation (as given by Equation (3.2)) is not a hyperbolic PDE but now that we discretized it temporally and T is taken at the previous time step, it is treated as a hyperbolic differential equation. Therefore we use a boundary condition only if the velocity is inward (i.e., the mass is flowing into the system). We multiply the time discretized *energy equation* by the test function ϕ and integrate over Ω

$$\int_\Omega \frac{s^\tau - s^{\tau-1}}{\Delta t}\phi dx + \int_\Omega \frac{\partial(s^\tau v^{\tau-1})}{\partial x}\phi dx = \int_\Omega \frac{\partial}{\partial x}\left(D\frac{\partial T^{\tau-1}}{\partial x}\right)\phi dx + \int_\Omega q\phi dx. \tag{3.17}$$

Applying integration by parts, we have the following weak formulation

$$\int_\Omega \frac{s^\tau - s^{\tau-1}}{\Delta t}\phi dx + \left[\left(s^\tau v^{\tau-1} - D\frac{\partial T^{\tau-1}}{\partial x}\right)\phi\right]_0^1 - \int_\Omega (s^\tau v^{\tau-1})\frac{d\phi}{dx}dx$$

$$= -\int_\Omega D\frac{\partial T^{\tau-1}}{\partial x}\frac{d\phi}{dx}dx + \int_\Omega q\phi \, dx, \tag{3.18}$$

By using the same discretization scheme for h^τ as we used for ρ^τ in *the mass equation*, we have

$$\sum_{j=1}^N \left(\int_\Omega \phi_i\phi_j dx\right)\frac{s_j^\tau - s_j^{\tau-1}}{\Delta t} - \sum_{j=1}^N \left(\int_\Omega v^{\tau-1}\frac{d\phi_i}{dx}\phi_j dx\right)s_j^\tau - s_1^\tau v_1^{\tau-1}\phi_i(x_1)$$

$$+ D\frac{\partial T^{\tau-1}}{\partial x}\bigg|_0 \phi_i(x_1) + s_N^\tau v_N^{\tau-1}\phi_i(x_N) - D\frac{\partial T^{\tau-1}}{\partial x}\bigg|_1 \phi_i(x_N)$$

$$= -D\int_\Omega \frac{\partial T^{\tau-1}}{\partial x}\frac{d\phi_i}{dx}dx + \int_\Omega q\phi_i dx. \tag{3.19}$$

Next, we apply the boundary condition as given by Equation (3.9). The boundary terms in the above equation become

$$-s_1^\tau v_1^{\tau-1}\phi_i(x_1) + D\frac{\partial T^{\tau-1}}{\partial x}\bigg|_{x=x_1} \phi_i(x_1) = -k_h(T_1^{\tau-1} - T_a)\delta_{1i}$$

$$+\begin{cases} s_1^\tau v_1^{\tau-1}\delta_{1ij} & \text{if } v_1^{\tau-1} \le 0 \\ -h_a k_m(\rho_1^\tau - \rho_a)\delta_{1i} & \text{if } v_1^{\tau-1} > 0 \end{cases},$$

$$s_N^\tau v_N^{\tau-1}\phi_i(x_N) - D\frac{\partial T^{\tau-1}}{\partial x}\bigg|_{x=x_N} \phi_i(x_N) = -k_h(T_N^{\tau-1} - T_N)\delta_{iN}$$

$$-\begin{cases} s_N^\tau v_N^{\tau-1}\delta_{ijN} & \text{if } v_N^{\tau-1} \ge 0 \\ h_a k_m(\rho_1^\tau - \rho_a)\delta_{iN} & \text{if } v_N^{\tau-1} < 0 \end{cases}.$$

The matrix form of Equation (3.19) is given by

$$M^{(1)}s^\tau + \Delta t S^{(2)}s^\tau = Ms^{\tau-1} + \Delta t f^{(2)}, \quad \tau = \{1, 2, .., \tau_{max}\}, \tag{3.20}$$

where the stiffness matrix $S^{(2)} = S^{(2)}(v^{\tau-1})$ and $f^{(2)} = f^{(2)}(v^{\tau-1})$ are defined as

$$S_{ij}^{(2)} = \int_\Omega v^{\tau-1} \frac{d\phi_i}{dx} \phi_i dx + \begin{cases} v_1^{\tau-1}\delta_{1ij} & \text{if } v_1^{\tau-1} \le 0 \\ -v_N^{\tau-1}\delta_{ijN} & \text{if } v_N^{\tau-1} \ge 0 , \\ 0 & \text{otherwise} \end{cases} \tag{3.21}$$

$$f_i^{(2)} = -D \int_0^1 \frac{dT^{\tau-1}}{dx} \frac{d\phi_i}{dx} dx + k_h(T_1^{\tau-1} - T_a)\delta_{1i} + k_h(T_N^{\tau-1} - T_a)\delta_{iN} \tag{3.22}$$

$$+ \begin{cases} h_a k_m(\rho_1^\tau - \rho_a)\delta_{1i} & \text{if } v_1^{\tau-1} > 0 \\ h_a k_m(\rho_N^\tau - \rho_a)\delta_{iN} & \text{if } v_N^{\tau-1} < 0 . \\ 0 & \text{otherwise} \end{cases} \tag{3.23}$$

Note that ρ^τ is already obtain by solving the mass equation. Therefore ρ_1^τ and ρ_N^τ are used in the computation of $S^{(2)}$ and $f^{(2)}$.

3.2.3 Streamline Upwind Petrov-Galerkin method for the mass equations

The mass equation, in our case, is a convection equation and the energy equation could be convection dominant in a case when $\frac{\partial T}{\partial x}$ is small and the heat source (q) is equal to zero. To apply the SUPG method, we split the test function into two parts $w = \phi + \psi$, where ϕ is the classical test function and ψ denotes a correction in order to take care of the upwind behavior. The weak form of the mass equation is written as

$$\int_0^1 \frac{\rho^\tau - \rho^{\tau-1}}{\Delta t} \phi(x)dx + \int_0^1 \frac{\rho^\tau - \rho^{\tau-1}}{\Delta t} \psi(x)dx =$$
$$-\int_0^1 \frac{\partial(\rho^\tau v^{\tau-1})}{\partial x} \phi(x)dx - \int_0^1 \frac{\partial(\rho^\tau v^{\tau-1})}{\partial x} \psi(x)dx, \tag{3.24}$$

or

$$\int_0^1 \frac{\rho^\tau - \rho^{\tau-1}}{\Delta t} \phi(x)dx + \int_0^1 \frac{\rho^\tau - \rho^{\tau-1}}{\Delta t} \psi(x)dx =$$
$$-\int_0^1 \frac{\partial(\rho^\tau v^{\tau-1})}{\partial x} \phi(x)dx - \int_0^1 \{\rho^\tau \frac{\partial v^{\tau-1}}{\partial x} + v^{\tau-1}\frac{\partial \rho^\tau}{\partial x}\}\psi(x)dx. \tag{3.25}$$

We neglect the term $\rho^\tau \frac{\partial v^{\tau-1}}{\partial x}$ because the contribution of this term is not significant [12] (also verified numerically). We use $\psi = \frac{\Delta x}{2}\xi\frac{d\phi_i}{dx}$ and take $\xi = sign(v)$, which corresponds to the classical upwind scheme. Following the same steps as in SGA method, we get a system of difference equations of the form

$$M\frac{\rho^\tau - \rho^{\tau-1}}{\Delta t} = S^{(\rho)}\rho^\tau + f^{(\rho)}, \tag{3.26}$$

where the mass matrix $M = M(v^{\tau-1})$ and the stiffness matrix $S^{(\rho)}$ for $i, j = \{1, ..., N\}$, are given by

$$M_{ij} = M_{ij}^{(1)} + \int_0^1 \frac{\Delta x}{2} \text{sign}(v^{\tau-1}) \frac{d\phi_i}{dx} \phi_j dx, \tag{3.27}$$

$$S_{ij}^{(\rho)} = S_{ij}^{(1)} - \int_0^1 v^{\tau-1} \frac{d\phi_j}{dx} \left(\frac{\Delta x}{2} \text{sign}(v^{\tau-1}) \frac{d\phi_i}{dx} \right) dx, \tag{3.28}$$

whereas the vector $f^{(\rho)} = f^{(1)}$.

3.2.4 The energy equation with SUPG method

For the energy equation, we get another system of difference equations of the form

$$M \frac{s^\tau - s^{\tau-1}}{\Delta t} = S^{(h)} s^\tau + f^{(h)}, \tag{3.29}$$

where M is already defined, $S^{(h)} = S^{(\rho)}$ and $f^{(h)}$ is given as

$$f_i^{(h)} = f_i^{(2)} + \int_0^1 q^\tau \left(\frac{\Delta x}{2} \text{sign}(v^{\tau-1}) \frac{d\phi_i}{dx} \right) dx. \tag{3.30}$$

3.2.5 Discretization of Darcy's law and other thermodynamic relations

Since the pair (ρ^τ, h^τ) has already been computed by Equations (3.15) and (3.20), T^τ, P^τ, and X_G^τ can be determined by the following function

$$(T_i^\tau, P_i^\tau, X_{G,i}^\tau) = g(\rho_i^\tau, h_i^\tau), \quad i = \{1, 2, .., N\}, \quad \tau = \{1, 2, .., \tau_{max}\}, \tag{3.31}$$

where g is given by Figure 3.1. The weak formulation of Darcy's law is written as

$$\int_\Omega v^\tau dx = -\frac{K}{\mu} \int_\Omega \frac{\partial P^\tau}{\partial x} \phi dx.$$

The temporal and spatial discretization of this equation leads to the matrix equation

$$Mv^\tau = f^{(v)},$$

where $f^{(v)} = f^{(v)}(P^\tau)$ is defined as

$$f_i^{(v)} = -\frac{K}{\mu} \int_\Omega \frac{\partial P^\tau}{\partial x} \phi_i dx,$$

where P^τ is already known from Relation (3.31).

3.3   Numerical Experiments

In the following subsections, four different examples (Case Studies) are given.

- Case Study 1: Inwardly isolated system with a positive initial velocity;

- Case Study 2: Inwardly isolated system with an inward initial velocity;

- Case Study 3: Open system, mass and energy flowing into the system;

- Case Study 4: Open system, mass and energy flowing out of the system.

The study of each case consists of $1D$ numerical results and their explanations. We compared one of the state variables (i.e., density) for several grid densities at various time instances in order to check for convergence. For all numerical experiments, we use the values that were given in Table 3.1 for several parameters. Remaining parametric values are given in individual experiments.

Symbol	value	comments/units
K	10^{-10}	$[m^2]$
N	41	(in general)
q	0	$[W/m^3]$
h_a	3.5×10^4	(in general)$[J/Kg]$
Δx	0.025	(in general)[m]
Δt	1/16000	(with dx =0.025)$[s]$
μ	5×10^{-5}	$Pa.s$
D	0.05	$[W/m/K]$

Table 3.1: Parametric values.

3.3.1   Initial conditions

Since the initial setting of T and X_G is easier in practice, we express the initial conditions in terms of T and X_G. Phase diagrams are also available for a transformation from (T, X_G) to (P, ρ, h). In the next chapter, we show that T is a function of P and vice versa, for two phase flow. Further, we observe that T and P have similar spatial derivative signs and a linear T profile results in an approximately linear P profile. The fluid flows from a higher pressure point to a lower pressure point and hence a desired initial velocity can be set by choosing a suitable temperature profile. For a positive initial velocity from both boundaries, one option is to set an initial temperature profile as shown in Figure 3.2(a). The resulting initial pressure pattern is depicted in 3.2(b). Such a pressure profile (a lower pressure at the central part and the higher pressure at and near boundaries) forces an inward initial velocity from both boundaries (see Figure 3.2(c)).
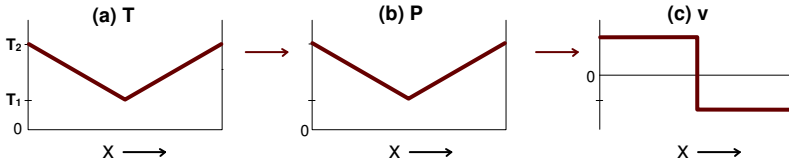
Figure 3.2: (a) Temperature profile for a desired initial condition, (b) the resulting pressure pattern, and (c) an inward velocity resulted from a suitable pressure (indirectly the temperature) profile.

3.3.2 Selection of a time step Δt

To our knowledge, the analytical bounds for Δt are unknown for the solution of the nonlinear system given by Equations (3.1) to (3.5). Empirically, $\Delta t \leq (\Delta x)^2/10$, for a stable solution when *IMEX* method is used. For example, a mesh of 101 grid nodes requires a time step 10^{-5} [s] i.e., 10^5 time steps are necessary per second of process time. To summarize, an excessively small Δt is needed despite the fact that we are using *IMEX* time integration scheme.

3.3.3 Case Study 1: Inwardly isolated system with a positive initial velocity

We call it an *inwardly isolated system* because the mass and energy can not enter the system but they can flow out of the system in this numerical experiment. We set $k_m = k_h = 0$ so that no mass or heat is allowed to enter the system. But the mass (and therefore energy) can flow out of the system due to an initial outward velocity at the right boundary ($v(x,0) > 0$). The ambient density and temperature (ρ_a and T_a) do not contribute in this example. We set an initial positive velocity, i.e., from left to right as shown in Figure 3.3(f). A desired initial velocity is obtained by setting a suitable initial temperature as explained in Section 3.3.1. The initial conditions are given by

$$T(x,0) = 291 - x, \qquad\qquad 0 \leq x \leq 1,$$
$$X_G(x,0) = 0.1, \qquad\qquad 0 \leq x \leq 1.$$

A linear temperature profile results in an approximately linear P, ρ, and h. A higher pressure value in the left part of the domain, as compared to the right part (Figure 3.3(d)), forces a positive velocity (Figure 3.3(f)). The mass cannot enter from the left boundary ($k_m = 0$), therefore, the velocity at the left boundary goes to zero in a very short time interval. As determined in our numerical experiment, this interval is 1.56×10^{-5} seconds but ideally it should take one iteration (i.e., no time). A positive velocity means that the density in the left side decreases with time (Figure 3.3(a)). It also means that the mass and the energy are flowing out from the right boundary. A decreasing density in the left side implies that the gas content is increasing as compared to the liquid phase (Figure 3.3(e)). Figure 3.4(a) shows that the total mass in the fluid system
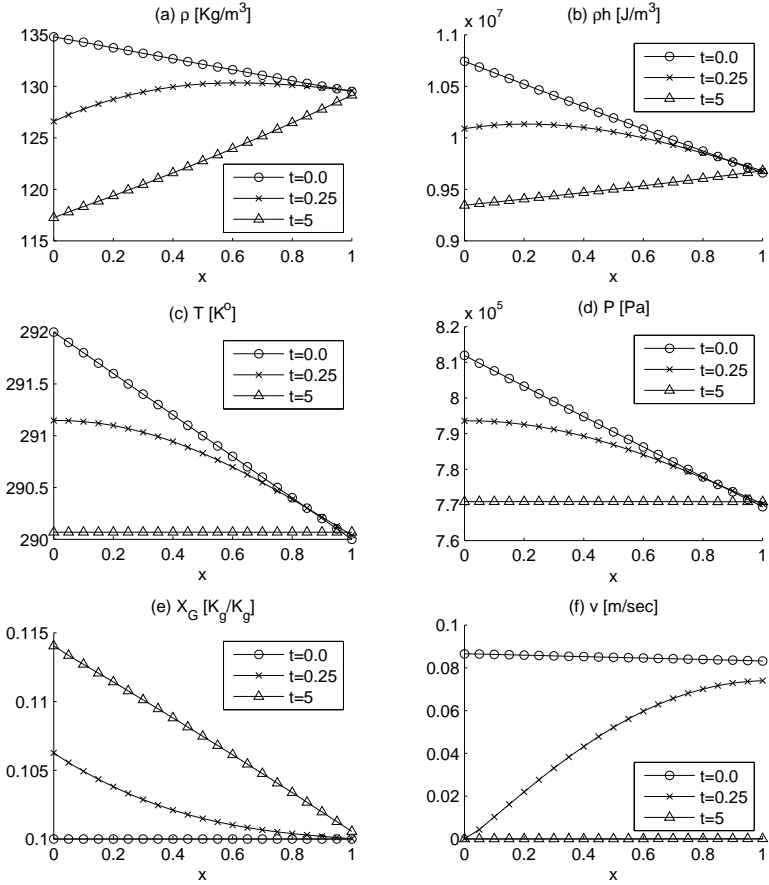
Figure 3.3: Case 1. Inwardly isolated system with $k_m = 0$, $k_h = 0$. Solution plots of (a) density, (b) total enthalpy, (c) temperature (d) pressure, (e) gas mass fraction, and (f) velocity.
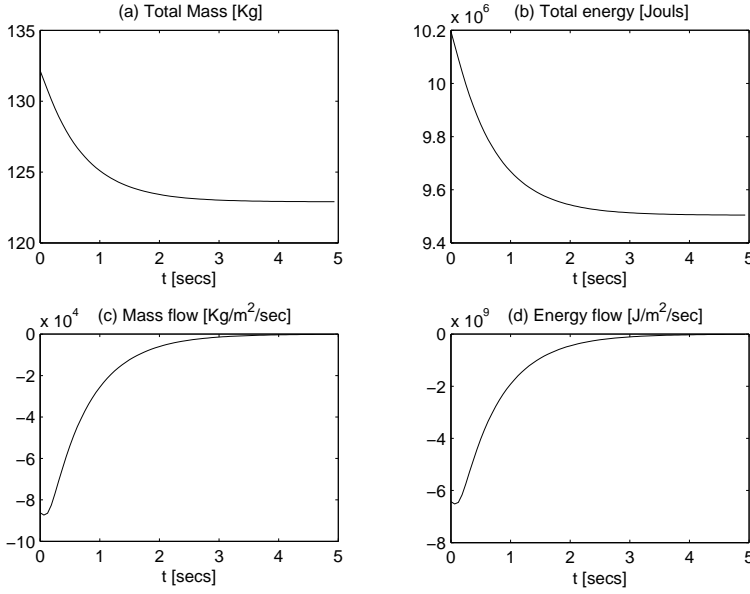
Figure 3.4: Case 1. Plots of (a) total mass, (b) total energy, (c) mass flow rate, and (d) energy flow rate.

$(\int_{\Omega} \rho dx \approx \sum_{i=2}^{N-1} \rho_i^{\tau} \Delta x + \frac{1}{2}(\rho_1^{\tau} \Delta x + \rho_N^{\tau} \Delta))$ decreases with time before reaching to a steady-state value. The total energy $(\int_{\Omega} \rho h dx \approx \sum_{i=2}^{N-1} \rho_i^{\tau} h_i^{\tau} \Delta x + \frac{1}{2}(\rho_1^{\tau} h_1^{\tau} \Delta x + \rho_N^{\tau} h_N^{\tau} \Delta x))$ is also shown in Figure 3.4(b). The total energy decreases because of the outward mass and heat transportation.

The mass and energy flow rates are given by [12]

$$\text{mass flow rate} = \sum_{i=1}^{N} \left(\sum_{j=1}^{N} S_{ij}^{(\rho)} \rho_j^{\tau} + f_i^{(\rho)} \right), \tag{3.32}$$

$$\text{energy flow rate} = \sum_{i=1}^{N} \left(\sum_{j=1}^{N} S_{ij}^{(h)} s_j^{\tau} + f_i^{(h)} \right), \tag{3.33}$$

where the matrices and vectors used are defined in Sections 3.2.1 and 3.2.2. These flow rates (as given in Figure 3.4(c) and 3.4(d)) are also used to check mass and energy conservation. In accordance with Fourier's law, the temperature (and pressure) decreases in the left part and with the passage of time the temperature (and pressure) gradient decreases (Figure 3.3(c) and 3.3(d)). A decreasing pressure gradient lowers the magnitude of the velocity. Both, the mass and heat flow from left to right, therefore, the total enthalpy also decreases in the left part and increases, relatively, in the right side as shown in Figure 3.3(b). Apart from the comparison of ρ, h, T, and P values in left and right sides, they always decrease in absolute terms due to the mass and heat outflow. The transport of mass and energy continues until the temperature

and pressure gradients become zero. It is obvious that the temperature and pressure are the main drivers for all transport. Other variables (ρ, h, X_G, and v) depend on T and P whereas T and P tend to become constant. The transfer of mass and heat stops as soon the system reaches its steady state value (thermal equilibrium).

3.3.4 Case Study 2: Inwardly isolated system with an inward initial velocity

In this numerical experiment, again $k_m = k_h = 0$, so that the environmental parameters ρ_a and T_a do not affect solution variables. Initial conditions are given by

$$T(x, 0) = \begin{cases} 291 - x, & \text{for } 0 \leq x \leq 0.5, \\ 291 + x - 1, & \text{for } 0.5 < x \leq 1, \end{cases}$$

$$X_G(x, 0) = 0.1, \quad 0 \leq x \leq 1.$$

This kind of temperature profile sets an inward initial velocity as explained in Section 3.3.1. A piecewise linear T results in an approximately piecewise linear ρ, P, and h as shown in Figure 3.5. Since there is no mass flow across boundaries, the velocity values immediately drop to zero at both boundary nodes (Figure 3.5(f)). A velocity (i.e., the mass flow) directed from both sides to the central part increases the density in the central part (Figure 3.5(a)). A decrease in the density at both sides means that the gas mass fraction increases there (Figure 3.5(e)). The temperature (and pressure) also lowers at both sides near boundaries and increases at the central part as depicted in Figure 3.5(c) and 3.5(d). These trends in the mass and heat flow shape the total enthalpy graphs as given in Figure 3.5(b). Again all transport stops when the temperature and the pressure gradients become zero. In this case, we observe that the steady-state condition is attained in a relatively short time (approx. 0.75 sec). Since there is no mass and the heat transfer across boundaries, the total mass and the total energy of the system should be unchanged with time. But we observe small numerical errors in the results as shown in Figure 3.6(a) and 3.6(b).

3.3.5 Case Study 3: Open system with an inflow of mass and energy.

In this example, we allow nonzero mass and heat fluxes. The initial and environmental data, we use, is given in Table 3.2. An inflow is triggered by the conductive heat

Table 3.2: Case Study 3: Open system

k_m	k_h	ρ_a	T_a	$T(x, 0)$	$X_G(x, 0)$
1.5	10^5	200	293	291	0.1

exchange boundary condition. Hence mass and energy flow into the system from both boundaries. The temperature increases with time and attains a steady-state value equal
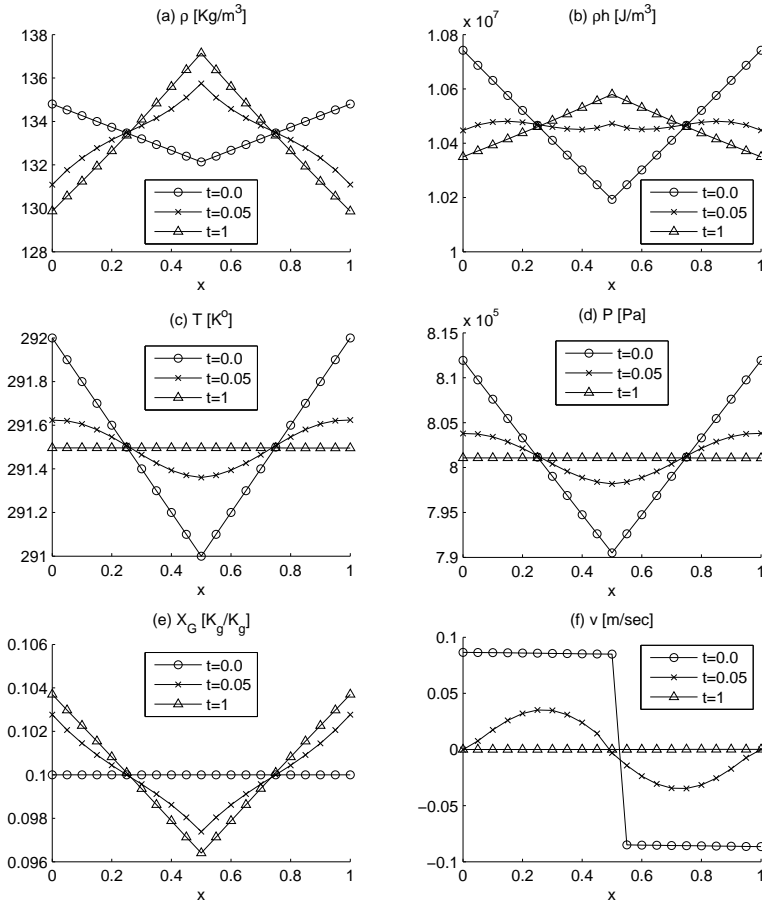
Figure 3.5: Case 2. Inwardly isolated system with initial inward velocity ($k_m = 0$, $k_h = 0$). Solution plots of (a) density, (b) total enthalpy, (c) temperature (d) pressure, (e) gas mass fraction, and (f) velocity.
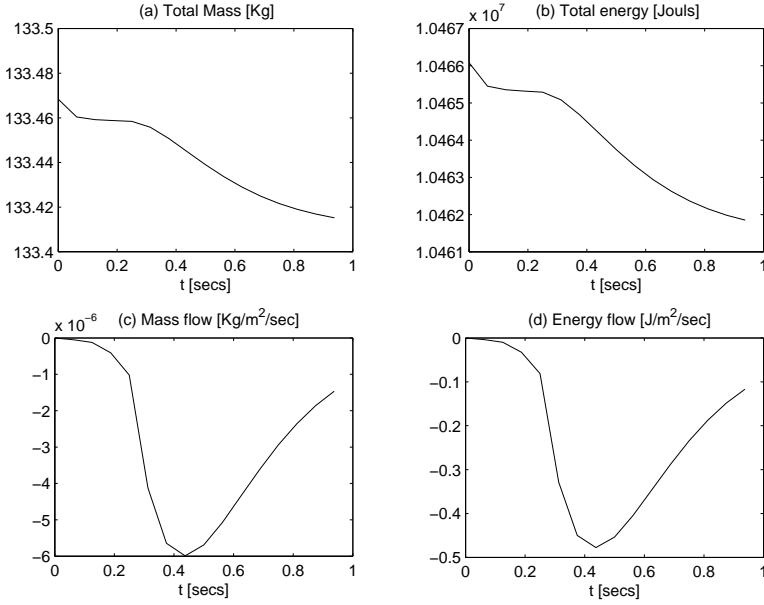
Figure 3.6: Case Study 2: Plots of (a) total mass, (b) total energy, (c) mass flow rate, and (d) energy flow rate.

to the ambient temperature T_a. The density graphs given in Figure 3.7(a) reveal that, with an inflow mass, the density increases everywhere within the system. An increase in mass and temperature values results in an increase in the total enthalpy in the system (Figure 3.7(b)). As soon the temperature (and pressure) becomes constant, the system reaches a steady-state value.

To investigate the shape of ρ plots on the time axis (at least initially), we consider the mass equation

$$\frac{\partial \rho}{\partial t} + \frac{\partial(\rho v)}{\partial x} = 0, \qquad\qquad x \in \Omega, t > 0, \qquad\qquad (3.34)$$

or

$$\frac{\partial \rho}{\partial t} + v \frac{\partial \rho}{\partial x} + \rho \frac{\partial v}{\partial x} = 0, \qquad\qquad (3.35)$$

Taking $x = x(t)$ and setting $\frac{dx}{dt} = v$ for ρ characteristics, we have

$$\frac{\partial \rho}{\partial t} + \frac{\partial \rho}{\partial x}\frac{dx}{dt} = -\frac{\partial v}{\partial x}\rho. \qquad\qquad (3.36)$$

From the numerical solution, we know that $\frac{\partial v}{\partial x}$ is negative mostly except that it is zero for $t = 0$ and for a steady state system. Equation (3.36) can be written as

$$\frac{d\rho}{dt} = \alpha^2 \rho, \qquad\qquad (3.37)$$
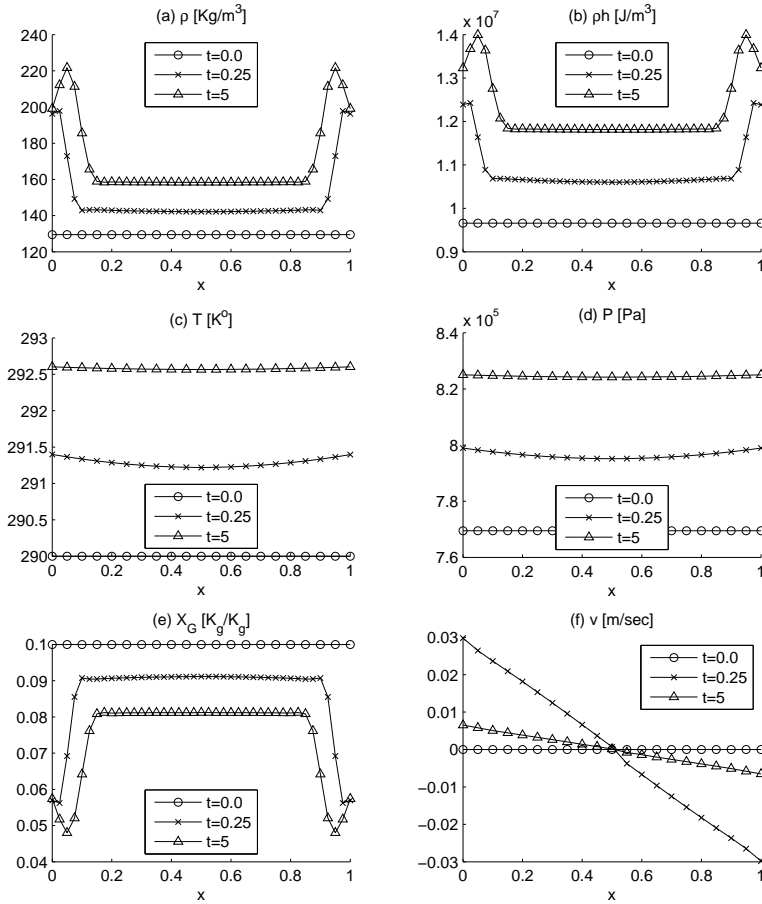
Figure 3.7: Case 3. Open system with $k_m = 1.5$, $k_h = 10^5$. Graphs for (a) density, (b) total enthalpy, (c) temperature (d) pressure, (e) gas mass fraction, and (f) velocity.

where $\alpha^2 = -\frac{\partial v}{\partial x}$ and the solution for the density is given by,

$$\rho(t) = \rho_0 e^{\int_0^t \alpha^2 dt}, \tag{3.38}$$

which indicates that we can expect exponentially increasing behavior in our numerical results. By looking at Figure 3.7(e) we can also argue that peaks in density graphs are possibly a result of phase change. But a complete information of density-enthalpy phase diagram's inner mechanism (i.e., relation among variables) is not available.

3.3.6 Case Study 4: Open system with an outflow of mass and energy.

In this case we set initial conditions for the mass and the energy outflow by taking the initial temperature higher than the system temperature. The initial and system parameters are given in Table 3.3. 3.2. The initial velocity is zero and the flow is triggered by

Table 3.3: Case Study 4: Open system

k_m	k_h	ρ_a	T_a	$T(x,0)$	$X_G(x,0)$
1.5	10^5	200	290	291	0.1

the conductive heat exchange boundary condition. The mass and the energy is flowing out of the system, therefore density and temperature go down and hence the gas mass fraction increases as shown in Figure 3.8(e). For an outward velocity, ρ_a plays no part. These results are given in Figure 3.8 and 3.9. A 'notching effect' can be observed in Figure 3.8 for density, enthalpy, and gas mass fraction plots, near boundaries. They are not physical and can be minimized by taking higher grid resolutions (as explained later).

In Figure 3.9, we have shown a switching effect between different boundary conditions. We know that the system model allows different flow mechanism between velocity conditions $\epsilon v \geq 0$ and $\epsilon v < 0$. If the value of v is close to zero then a rounding error can cause an undue switching between flow schemes.

3.4 The numerical solution by Picard method

In our numerical experiments, a small (mesh dependent) time step is necessary for a stable output, where we use the $IMEX$ time integration scheme. Now we apply a fully-implicit time integration and use Picard iteration for linearization. We use the index p for the Picard loop in our solution algorithm. For a good readability, we omit the time index τ when p is also there (but it is assumed to be there). The system is written as

$$\frac{\rho^p - \rho^{\tau-1}}{\Delta t} + \frac{\partial(\rho^p v^{p-1})}{\partial x} = 0, \qquad\qquad x \in \Omega,\ t > 0, \qquad (3.39)$$

$$\frac{s^p - s^{\tau-1}}{\Delta t} + \frac{\partial(s^p v^{p-1})}{\partial x} = \frac{\partial}{\partial x}\left(D\frac{\partial T^{p-1}}{\partial x}\right) + q^\tau, \qquad\qquad (3.40)$$

$$T^p = T(\rho^p, h^p), \qquad\qquad (3.41)$$

$$P^p = P(\rho^p, h^p), \qquad\qquad (3.42)$$

$$v^p = -\frac{K}{\mu}\frac{\partial P^p}{\partial x}. \qquad\qquad (3.43)$$

The numerical solution of these equations by FEM is analogous to Sections 3.2.1 to 3.2.5. Unfortunately, we do not see any improvement in Δt value compared to the
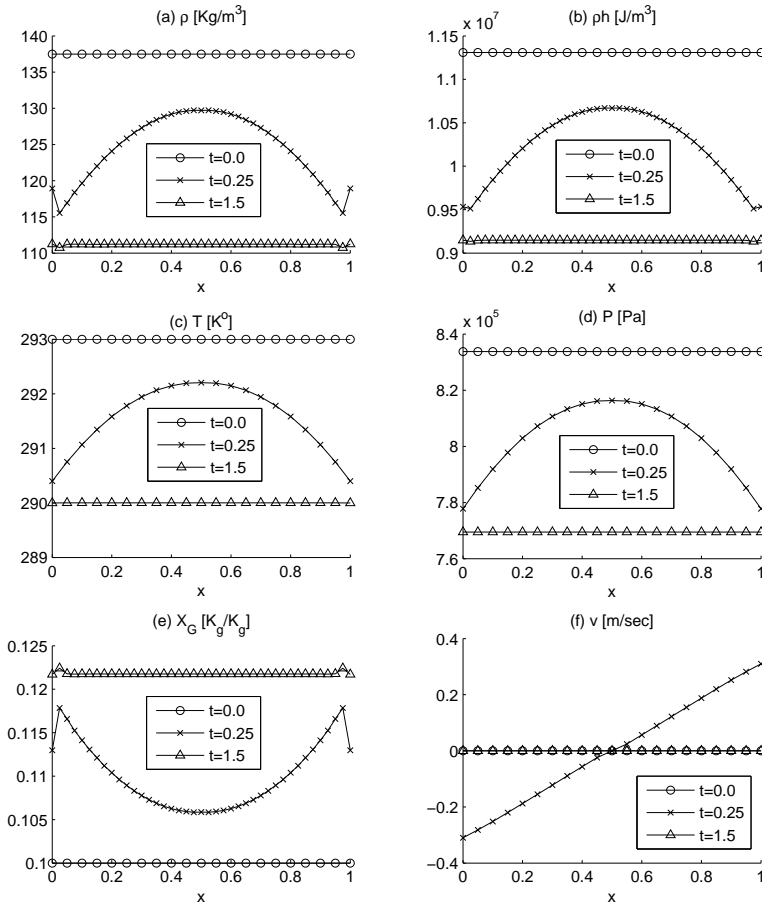
Figure 3.8: Case 4. Open system with $k_m = 1.5$, $k_h = 10^5$. Graphs for (a) density, (b) total enthalpy, (c) temperature (d) pressure, (e) gas mass fraction, and (f) velocity.
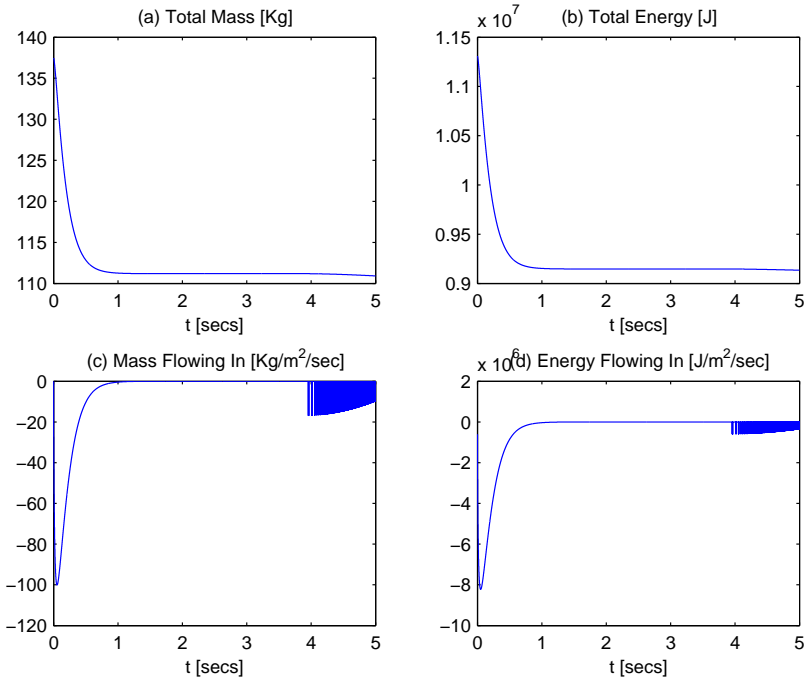
Figure 3.9: Case 4. A switching effect due to rounding errors. Plots of (a) total mass, (b) total energy, (c) mass flowing into the system, and (d) energy flowing into the system.

IMEX method. The solution graphs by both methods are similar. We will discuss the issue of Δt further in Chapter 5.

3.5   Problems and issues with the current algorithm and results

In this chapter, we introduced the ρ-h method for a $1D$ flow system by *FEM*. For the time integration, *IMEX* and Picard methods are used. We performed numerical experiments with several initial and boundary conditions. Although the ρ-h method seems to work for certain test cases, there are several aspects of the solution algorithm and the results which need further investigation. One of the major problem we encounter is that Δt should be proportional to $(\Delta x)^2$ for a stable output. This is true for both, the *IMEX* and Picard methods. Furthermore, these linearization schemes do not permit a completely isolated system. Mass and energy can always leave the system if v is outward. At boundary, a velocity close to zero may cause a switching effect

between imposing a boundary condition ($\epsilon v < 0$) and simulating without a boundary condition ($\epsilon v \geq 0$). For an open system to mass and heat, certain solution variables exhibit sudden changes and steep gradients near the boundary. In later chapters, we further investigate the boundary conditions and suggest some guidelines to avoid these nonphysical changes and steep gradients, near the boundary.

Chapter 4

The density enthalpy model in $2D$ with IMEX time integration

In this chapter we extend the model to two dimensions. The main objective here is to show that the model is consistent with respect to the dimensionality. We also discuss the use of Robin boundary conditions in the model and the consequences of the fact that $P = P(T)$ instead of $P = P(T, X_G)$. In the simulation section, the results are compared with a suitable $1D$ example. Furthermore, the solution results for a true $2D$ example are also presented and discussed. For $1D$ case, we did not find any advantage of using Picard method over IMEX method (refer to Chapter 3) therefore, we only used IMEX method for system linearization in this chapter.

4.1 Mathematical modeling for the $2D$ fluid system

The domain Ω in this case is taken as a unit square and all gradients of system variables are at most two dimensional. The dynamics of the system are given by the following equations

$$\frac{\partial \rho}{\partial t} + \nabla \cdot (\rho v) = 0, \qquad\qquad x \in \Omega,\ t > 0, \qquad (4.1)$$

$$\frac{\partial(\rho h)}{\partial t} + \nabla \cdot (\rho h v) - \nabla \cdot (D\nabla T) = q, \qquad\qquad x \in \Omega,\ t > 0, \qquad (4.2)$$

$$T = T(\rho, h), \qquad\qquad (4.3)$$

$$P = P(\rho, h), \qquad\qquad (4.4)$$

$$v = -\frac{K}{\mu}\nabla P, \qquad\qquad x \in \Omega,\ t > 0, \qquad (4.5)$$

$$X_G = X_G(\rho, h), \qquad\qquad (4.6)$$

where Equations (4.1), (4.2), and (4.5) are respectively the mass conservation, energy conservation and Darcy's laws. The operator $\boldsymbol{\nabla}$, $\boldsymbol{x}$, and the velocity $\boldsymbol{v}$ are defined as $\boldsymbol{\nabla} =< \frac{\partial}{\partial x}, \frac{\partial}{\partial y} >$, $\boldsymbol{x} = (x, y)$, and $\boldsymbol{v} =< v_x, v_y >$. The initial conditions are given by

$$\rho(\boldsymbol{x}, 0) = \rho_0, \qquad\qquad \boldsymbol{x} \in \Omega, \qquad\qquad (4.7)$$

$$h(\boldsymbol{x}, 0) = h_0, \qquad\qquad \boldsymbol{x} \in \Omega. \qquad\qquad (4.8)$$

The following boundary conditions apply to *the mass equation*

$$\rho \boldsymbol{v} \cdot \hat{\boldsymbol{n}} = k_m(\rho - \rho_a), \quad t > 0, \quad \boldsymbol{x} \in \Gamma, \qquad\qquad (4.9)$$

where $\hat{\boldsymbol{n}}$ is a unit outward pointing normal vector at the boundary. The boundary condition for *the energy equation* is given as

$$-D\boldsymbol{\nabla}T \cdot \hat{\boldsymbol{n}} + (\rho h)\boldsymbol{v} \cdot \hat{\boldsymbol{n}} = k_h(T - T_a) + \tilde{h}k_m(\rho - \rho_a), \qquad t > 0, \quad \boldsymbol{x} \in \Gamma, \qquad (4.10)$$

where

$$\tilde{h} = \begin{cases} h_a, & \text{if } \boldsymbol{v} \cdot \hat{\boldsymbol{n}} < 0, \\ h_\Gamma, & \text{if } \boldsymbol{v} \cdot \hat{\boldsymbol{n}} > 0. \end{cases}$$

4.1.1   The use of Robin boundary conditions in the ρ-h model

The use of Robin boundary conditions on our specific thermodynamic system leads to solutions near boundaries that did not seem to make any sense (abrupt changes or steep gradients). To prove that these boundary conditions are ill-conditioned for our specific thermodynamic system, we proceed with the following arguments. In the ρ-h model, the pair (T, X_G) is sufficient to determine the rest of the system variables like ρ, h, P, $\boldsymbol{v}$, etc. The total differential of $P(T, X_G)$, in this case, is given by

$$\boldsymbol{\nabla}P = \frac{\partial P}{\partial T}\boldsymbol{\nabla}T + \frac{\partial P}{\partial X_G}\boldsymbol{\nabla}X_G, \qquad\qquad (4.11)$$

Now we found that the equality $\frac{\partial P}{\partial X_G} = 0$ holds for a two-phase flow. In Figure 4.1(a), the relation between P and T is shown for $0 < X_G < 1$, which is a unique curve (i.e., P versus T relation is the same monotonically increasing curve, for all values of X_G). Figure 4.1(b) shows plots of P against X_G for three temperature values. Clearly $\frac{\partial P}{\partial X_G} = 0$ for $250 \leq T \leq 350$. Therefore, Equation (4.11) reduces to

$$\boldsymbol{\nabla}P = \frac{\partial P}{\partial T}\boldsymbol{\nabla}T, \qquad\qquad (4.12)$$

where $\frac{\partial P}{\partial T}$ is nonzero (refer to Figure 4.1(a)).
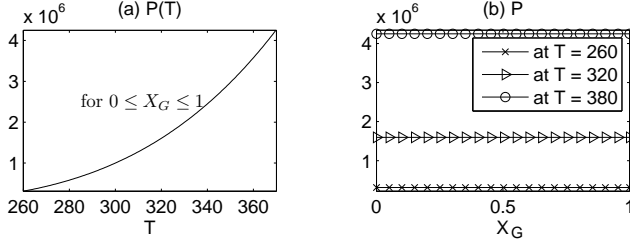
Figure 4.1: . Pressure relation with temperature and gas mass fraction.

Next, we multiply Equation (4.9) by h_Γ and subtract it from Equation (4.10), thus we obtain

$$-D\boldsymbol{\nabla} T \cdot \hat{\boldsymbol{n}} + (h - \tilde{h})\rho \boldsymbol{v} \cdot \hat{\boldsymbol{n}} = k_h(T - T_a), \quad \text{(at boundary, } s = \rho h_\Gamma),$$

$$-D\frac{1}{\left(\frac{\partial P}{\partial T}\right)}\boldsymbol{\nabla} P \cdot \hat{\boldsymbol{n}} + (h - \tilde{h})\rho \boldsymbol{v} \cdot \hat{\boldsymbol{n}} = k_h(T - T_a), \quad \text{(follows from Eq. (4.12)),}$$

$$\frac{D\mu}{K}\frac{1}{\left(\frac{\partial P}{\partial T}\right)}\boldsymbol{v} \cdot \hat{\boldsymbol{n}} + (h - \tilde{h})\rho \boldsymbol{v} \cdot \hat{\boldsymbol{n}} = k_h(T - T_a), \quad \text{(follows from Darcy's Law).}$$

Combination with Equation (4.9), gives

$$\left(D\frac{\mu}{K}\frac{1}{\left(\frac{\partial P}{\partial T}\right)} + h - \tilde{h}\right)k_m(\rho - \rho_a) = k_h(T - T_a)$$

which shows that k_m and k_h cannot be chosen independently. Furthermore the relation is time-dependent and nonlinear except for $k_m = k_h = 0$. Therefore the proposed Robin boundary conditions are ill-posed if $\frac{\partial P}{\partial X_G} = 0$. Hence, for this case, we proved the following proposition.

Proposition 4.1.1. *If $\frac{\partial P}{\partial X_G} = 0$, then the problem stated by Equations (4.1)-(4.5) supplied with initial conditions and boundary conditions as in Equations (4.9) and (4.10) is ill-posed if either k_h or k_m (or both) is nonzero.*

Presently, we consider an isolated system, i.e., $k_m = k_h = 0$. From Proposition 4.1.1, it follows that the problem is well-posed. In Chapter 6, we show that $P = P(T)$ is actually related to the two-phase flow and is consistent with Gibbs phase rule. In Chapter 7, we further look into the possibility of nonzero transfer coefficients k_m and k_h.

4.1.2 Isoparametric transformation

We keep the solution algorithm general but use a simple $2D$ computational domain, i.e., a unit square as shown in Figure 4.2. The domain interior and boundary are represented by Ω and Γ, respectively. For a numerical solution, we divide the domain into

$N = N_x \times N_y$ nodes or $(N_x - 1) \times (N_y - 1)$ small elements, where N_x and N_y are the number of nodes in respective directions. In general, we use $N_x = N_y = 41$ or 1600 square elements each having the same dimension of $\frac{1}{40}$ meter. Even with a 41×41 resolution, simulation of 1 second of actual process takes 24 hours of computational time (by using a 2.5 GHz Intel PC, Windows XP, and Matlab). For interior rectangular elements, the number of nodes per element is 4. We cannot give a general shape for continuous (conforming) basis functions in case of rectangular elements. Therefore we used a technique called *Isoparametric Transformation* [39]. We repeat this principle here, for the sake of completeness. Each rectangular element in x-y-plane is transformed to a unit square reference element in the ξ-η-plane. Four points $\mathbf{x}_1$, $\mathbf{x}_2$, $\mathbf{x}_3$, and $\mathbf{x}_4$ in each element are transformed to fixed points $\boldsymbol{\xi}_1$, $\boldsymbol{\xi}_2$, $\boldsymbol{\xi}_3$, and $\boldsymbol{\xi}_4$, where $\mathbf{x}_i = (x_i, y_i)$ and $\boldsymbol{\xi}_i = (\xi_i, \eta_i)$, $i = 1, 2, 3, 4$ with $\boldsymbol{\xi}_i$ are the vertices of the reference element shown in Figure 4.3. The inverse transformation is given by
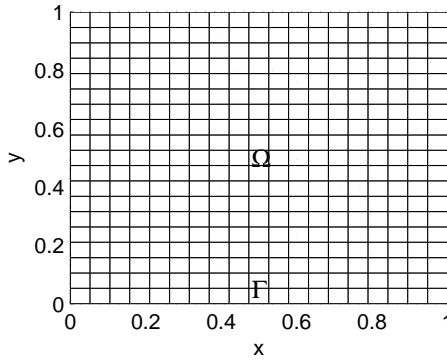
Figure 4.2:

$$\mathbf{x} = \sum_{i=1}^{4} \mathbf{x}_i \phi_i(\xi, \eta), \tag{4.13}$$
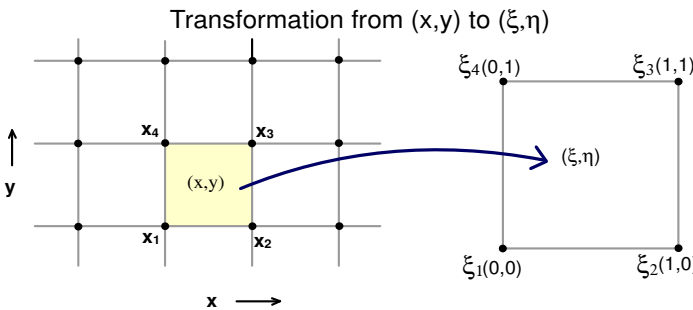
Figure 4.3: Isoparametric transformation from (x, y) plane to (ξ, η) plane.

where

$$\phi_1 = (1 - \xi)(1 - \eta), \ \phi_2 = \xi(1 - \eta), \ \phi_3 = \xi\eta, \ \text{and } \phi_4 = (1 - \xi)\eta. \qquad (4.14)$$

We need to compute $\nabla\phi_i(\boldsymbol{x})$ and $dx \, dy = \left|\frac{\partial(x,y)}{\partial(\xi,\eta)}\right| d\xi \, d\eta$, because they appear in integral terms arising in the computation of element matrices. Let the Jacobian J be given by

$$J = \frac{\partial(x, y)}{\partial(\xi, \eta)} = \begin{bmatrix} \frac{\partial x}{\partial \xi} & \frac{\partial x}{\partial \eta} \\ \frac{\partial y}{\partial \xi} & \frac{\partial y}{\partial \eta} \end{bmatrix}.$$

From Equation (4.13) and (4.14), we have

$$x = x_1 + (x_2 - x_1)\xi + (x_4 - x_1)\eta + A_x\xi\eta,$$

$$y = y_1 + (y_2 - y_1)\xi + (y_4 - y_1)\eta + A_y\xi\eta,$$

where, $A_x = (x_1 - x_2 + x_3 - x_4)$ and $A_y = (y_1 - y_2 + y_3 - y_4)$,

$$\frac{\partial x}{\partial \xi} = x_2 - x_1 + A_x\eta, \quad \frac{\partial x}{\partial \eta} = x_4 - x_1 + A_x\xi,$$

$$\frac{\partial y}{\partial \xi} = y_2 - y_1 + A_y\eta, \quad \frac{\partial y}{\partial \eta} = y_4 - y_1 + A_y\xi.$$

Let Δ_J be the determinant of J;

$$\Delta_J = (x_2 - x_1 + A_x\eta)(y_4 - y_1 + A_y\xi) - (x_4 - x_1 + A_x\xi)(y_2 - y_1 + A_y\eta)$$

Thus we have determined $d(x, y) = |\Delta_J|d(\xi, \eta)$. For $\nabla\phi_i$, we have

$$\nabla\phi_i = \left\langle \frac{\partial \phi_i}{\partial x}, \frac{\partial \phi_i}{\partial x} \right\rangle,$$

where,

$$\frac{\partial \phi_i}{\partial x} = \frac{\partial \phi_i}{\partial \xi}\frac{\partial \xi}{\partial x} + \frac{\partial \phi_i}{\partial \eta}\frac{\partial \eta}{\partial x}, \quad i = 1, 2, 3, 4. \qquad (4.15)$$

Now $\frac{\partial \phi_i}{\partial \xi}$ and $\frac{\partial \phi_i}{\partial \eta}$ are determined from Equation (4.14) (see Table 4.1). For $\frac{\partial \xi}{\partial x}$ and $\frac{\partial \eta}{\partial x}$,

i	$\frac{\partial \phi_i}{\partial \xi}$	$\frac{\partial \phi_i}{\partial \eta}$
1	$-(1 - \eta)$	$-(1 - \xi)$
2	$1 - \eta$	$-\xi$
3	η	ξ
4	$-\eta$	$1 - \xi$

Table 4.1: Four basis functions for the standard element and its partial derivatives.

we proceed with the following steps,

$$J^{-1} = \frac{1}{\Delta_J} \begin{bmatrix} \frac{\partial y}{\partial \eta} & -\frac{\partial x}{\partial \eta} \\ -\frac{\partial y}{\partial \xi} & \frac{\partial x}{\partial \xi} \end{bmatrix}. \tag{4.16}$$

But J^{-1} is also given by the following expression [18],

$$J^{-1} = \begin{bmatrix} \frac{\partial \xi}{\partial x} & \frac{\partial \xi}{\partial y} \\ \frac{\partial \eta}{\partial x} & \frac{\partial \eta}{\partial y} \end{bmatrix}. \tag{4.17}$$

Comparing Equations (4.16) and (4.17), we have,

$$\frac{\partial \xi}{\partial x} = \frac{1}{\Delta_J} \frac{\partial y}{\partial \eta} \text{ and } \frac{\partial \eta}{\partial x} = \frac{-1}{\Delta_J} \frac{\partial y}{\partial \xi},$$

where $\frac{\partial y}{\partial \eta}$ and $\frac{\partial y}{\partial \xi}$ are already computed. Similarly,

$$\frac{\partial \phi_i}{\partial y} = \frac{\partial \phi_i}{\partial \xi} \frac{\partial \xi}{\partial y} + \frac{\partial \phi_i}{\partial \eta} \frac{\partial \eta}{\partial y}, \quad i = 1, 2, 3, 4, \tag{4.18}$$

where $\frac{\partial \xi}{\partial y} = \frac{-1}{\Delta_J} \frac{\partial x}{\partial \eta}$ and $\frac{\partial \eta}{\partial y} = \frac{1}{\Delta_J} \frac{\partial x}{\partial \xi}$. Hence $\boldsymbol{\nabla} \phi_i$ is completely determined. We have used these values to compute element matrices. It is also important to mention that we are using the following Newton-Cotes quadrature rule (for a rectangle) in order to determine $2D$ integrals appearing in the proceeding sections.

$$\int_{e_{xy}} I(x, y) dx dy \approx \frac{1}{4} \sum_{i=1}^{4} I(x_i, y_i). \tag{4.19}$$

4.1.3   Discretization of $2D$ mass equation with standard Galerkin approach

We linearize the mass equation by using IMEX time integration method. Hence, we obtain

$$\frac{\rho^\tau - \rho^{\tau-1}}{\Delta t} = -\boldsymbol{\nabla} \cdot (\rho^\tau \boldsymbol{v}^{\tau-1}), \quad \boldsymbol{x} \in \Omega, \quad \tau = \{1, 2, .., \tau_{max}\}, \tag{4.20}$$

which is a hyperbolic PDE and hence, the boundary conditions are applicable only if the velocity is inward across the boundary (i.e., if $\boldsymbol{v} \cdot \hat{\boldsymbol{n}} < 0$). To obtain the weak formulation, we multiply this equation by a test function $\phi(\boldsymbol{x})$, and integrate over Ω

$$\int_\Omega \frac{\rho^\tau - \rho^{\tau-1}}{\Delta t} \phi d\Omega = -\int_\Omega \boldsymbol{\nabla} \cdot (\rho^\tau \boldsymbol{v}^{\tau-1}) \phi d\Omega. \tag{4.21}$$

Using the product rule

$$\boldsymbol{\nabla} \cdot (\rho \boldsymbol{v} \phi) = \phi \boldsymbol{\nabla} \cdot (\rho \boldsymbol{v}) + \rho \boldsymbol{v} \cdot \boldsymbol{\nabla} \phi, \tag{4.22}$$

and the divergence theorem

$$\int_\Omega \boldsymbol{\nabla} \cdot \boldsymbol{F} d\Omega = \int_\Gamma \boldsymbol{F} \cdot \hat{\boldsymbol{n}} d\Gamma, \tag{4.23}$$

in Equation (4.21) we have

$$\int_\Omega \frac{\rho^\tau - \rho^{\tau-1}}{\Delta t} \phi d\Omega = -\int_\Gamma \rho^\tau \phi \boldsymbol{v}^{\tau-1} \cdot \hat{\boldsymbol{n}} d\Gamma + \int_\Omega \rho^\tau \boldsymbol{v}^{\tau-1} \cdot \boldsymbol{\nabla} \phi d\Omega. \tag{4.24}$$

We choose a set of basis functions $\{\phi_j\}$ and approximate the solution variable by

$$\rho^\tau(\boldsymbol{x}) \approx \sum_{j=1}^N \rho_j^\tau \phi_j(\boldsymbol{x}). \tag{4.25}$$

Using the approximation of $\rho^\tau(\boldsymbol{x})$ and the value of ϕ in Equation (4.24), and applying the boundary conditions, we realize

$$\sum_{j=1}^N \frac{\rho_j^\tau - \rho_j^{\tau-1}}{\Delta t} \left(\int_\Omega \phi_i \phi_j d\Omega \right) - \sum_{j=1}^N \rho_j^\tau \int_\Omega \phi_j \boldsymbol{v}^{\tau-1} \cdot \boldsymbol{\nabla} \phi_j d\Omega$$

$$= - \begin{cases} \sum_{j=1}^n \rho_j^\tau \int_\Gamma k_m \phi_i \phi_j d\Gamma + \int_\Gamma k_m \phi_i \rho_a d\Gamma, & \text{if } \boldsymbol{v}^{\tau-1} \cdot \hat{\boldsymbol{n}} < 0, \\ \sum_{j=1}^n \rho_j^\tau \int_\Gamma \phi_i \phi_j \boldsymbol{v} \cdot \hat{\boldsymbol{n}} d\Gamma, & \text{if } \boldsymbol{v}^{\tau-1} \cdot \hat{\boldsymbol{n}} \geq 0, \end{cases} \tag{4.26}$$

where $n = 2(N_x + N_y)$ is the number of boundary nodes. This equation can be written in matrix form

$$M^{(1)} \boldsymbol{\rho}^\tau + \Delta t S^{(1)} \boldsymbol{\rho}^\tau = M^{(1)} \boldsymbol{\rho}^{\tau-1} + \Delta t \boldsymbol{f}^{(1)}, \tag{4.27}$$

where elements of the global matrices M^1, S^1, and vector $\boldsymbol{f}^1$ are defined as

$$M_{ij}^{(1)} = \int_\Omega \phi_i \phi_j d\Omega, \tag{4.28}$$

$$S_{ij}^{(1)} = \int_\Omega \phi_j \boldsymbol{v}^{\tau-1} \cdot \boldsymbol{\nabla} \phi_i d\Omega + \begin{cases} \int_\Gamma k_m \phi_i \phi_j d\Gamma, & \text{if } \boldsymbol{v}^{\tau-1} \cdot \hat{\boldsymbol{n}} < 0, \\ \int_\Gamma \phi_i \phi_j \boldsymbol{v} \cdot \hat{\boldsymbol{n}} d\Gamma, & \text{if } \boldsymbol{v}^{\tau-1} \cdot \hat{\boldsymbol{n}} \geq 0, \end{cases} \tag{4.29}$$

$$f_i^{(1)} = \begin{cases} \int_\Gamma k_m \phi_i \rho_a d\Gamma, & \text{if } \boldsymbol{v}^{\tau-1} \cdot \hat{\boldsymbol{n}} < 0, \\ 0, & \text{if } \boldsymbol{v}^{\tau-1} \cdot \hat{\boldsymbol{n}} \geq 0. \end{cases} \tag{4.30}$$

4.1.4 Discretization of the energy equation in $2D$ with standard Galerkin approach

Taking $s = \rho h$ and proceeding with the same steps, as mentioned for the mass equation, in order to obtain the weak formulation for the $2D$ energy equation (Equation (4.2)). Hence, we have

$$\int_\Omega \frac{s^\tau - s^{\tau-1}}{\Delta t} \phi d\Omega + \int_\Omega \boldsymbol{\nabla} \cdot (s^\tau \boldsymbol{v}^{\tau-1}) \phi d\Omega = \int_\Omega \boldsymbol{\nabla} \cdot (D\boldsymbol{\nabla} T^{\tau-1}) \phi d\Omega + \int_\Omega q^\tau \phi d\Omega. \tag{4.31}$$

Substituting

$$\int_{\Omega} \mathbf{\nabla} \cdot (s\mathbf{v})\phi d\Omega = - \int_{\Gamma} s\phi \mathbf{v} \cdot \hat{\mathbf{n}} d\Gamma + \int_{\Omega} s\mathbf{v} \cdot \mathbf{\nabla}\phi d\Omega, \tag{4.32}$$

and

$$\int_{\Omega} \mathbf{\nabla} \cdot (D\mathbf{\nabla}T)\phi d\Omega = \int_{\Gamma} D\frac{\partial T}{\partial n}\phi d\Gamma - \int_{\Omega} D\mathbf{\nabla}T \cdot \mathbf{\nabla}\phi d\Omega, \tag{4.33}$$

into equation (4.31) we get

$$\int_{\Omega} \frac{s^{\tau} - s^{\tau-1}}{\Delta t}\phi d\Omega = - \int_{\Gamma} s^{\tau}\phi \mathbf{v}^{\tau-1} \cdot \hat{\mathbf{n}} d\Gamma + \int_{\Omega} s^{\tau}\mathbf{v}^{\tau-1} \cdot \mathbf{\nabla}\phi d\Omega +$$

$$\int_{\Gamma} D\frac{\partial T^{\tau-1}}{\partial \hat{\mathbf{n}}}\phi d\Gamma - \int_{\Omega} D\mathbf{\nabla}T^{\tau-1} \cdot \mathbf{\nabla}\phi d\Omega + \int_{\Omega} q^{\tau}\phi d\Omega. \tag{4.34}$$

Now, the velocity direction has to be taken into account when we numerically solve this equation.

$$\int_{\Omega} \frac{s^{\tau} - s^{\tau-1}}{\Delta t}\phi d\Omega = \int_{\Omega} s^{\tau}\mathbf{v}^{\tau-1} \cdot \mathbf{\nabla}\phi d\Omega - \int_{\Gamma} k_h(T^{\tau-1} - T_a)\phi_i$$

$$- \int_{\Omega} D\mathbf{\nabla}T^{\tau-1} \cdot \mathbf{\nabla}\phi d\Omega + \int_{\Omega} q^{\tau}\phi d\Omega - \begin{cases} \int_{\Gamma} h_a k_m(\rho^{\tau} - \tau_a)\phi d\Gamma, & \text{if } \mathbf{v}^{\tau-1} \cdot \hat{\mathbf{n}} < 0, \\ \int_{\Gamma} s^{\tau}\mathbf{v}^{\tau-1} \cdot \hat{\mathbf{n}}\phi d\Gamma, & \text{if } \mathbf{v}^{\tau-1} \cdot \hat{\mathbf{n}} \geq 0, \end{cases} \tag{4.35}$$

Using the approximation $s^{\tau} \approx \sum_{j=1}^{N} s_j^{\tau}\phi_j$ and $\phi = \phi_i$, the above equation is written as

$$\sum_{j=1}^{N} \frac{\rho_j^{\tau} - \rho_j^{\tau-1}}{\Delta t}\left(\int_{\Omega} \phi_i\phi_j d\Omega\right) - \sum_{j=1}^{N} s_j^{\tau}\int_{\Omega} \phi_j\mathbf{v}^{\tau-1} \cdot \mathbf{\nabla}\phi_i d\Omega$$

$$= - \int_{\Omega} D\mathbf{\nabla}T^{\tau-1} \cdot \mathbf{\nabla}\phi_i d\Omega - \int_{\Gamma} k_h(T^{\tau-1} - T_a)\phi_i d\Gamma + \int_{\Omega} q^{\tau}\phi_i d\Omega$$

$$- \begin{cases} \int_{\Gamma} h_a k_m(\rho^{\tau} - \rho_a)\phi_i d\Gamma, & \text{if } \mathbf{v}^{\tau-1} \cdot \hat{\mathbf{n}} < 0, \\ \sum_{j=1}^{n} s_j^{\tau}\int_{\Gamma} \phi_i\phi_j\mathbf{v}^{\tau-1} \cdot \hat{\mathbf{n}}d\Gamma, & \text{if } \mathbf{v}^{\tau-1} \cdot \hat{\mathbf{n}} \geq 0. \end{cases} \tag{4.36}$$

Again, this equation is written in the matrix form, as follows

$$M^{(2)}\mathbf{s}^{\tau} + \Delta t S^{(2)}\mathbf{s}^{\tau} = M^{(2)}\mathbf{s}^{\tau-1} + \Delta t\mathbf{f}^{(2)}. \tag{4.37}$$

The elements of the global matrices are defined as

$$S_{ij}^{(2)} = \int_{\Omega} \phi_j\mathbf{v}^{\tau-1} \cdot \mathbf{\nabla}\phi_i d\Omega - \begin{cases} 0, & \text{if } \mathbf{v} \cdot \hat{\mathbf{n}} < 0, \\ \int_{\Gamma} \phi_i\phi_j\mathbf{v}^{\tau-1} \cdot \hat{\mathbf{n}}d\Gamma, & \text{if } \mathbf{v} \cdot \hat{\mathbf{n}} \geq 0, \end{cases} \tag{4.38}$$

$$f_i^{(2)} = - \int_{\Omega} D\mathbf{\nabla}T \cdot \mathbf{\nabla}\phi_i d\Omega + \int_{\Omega} q\phi_i d\Omega - \int_{\Gamma} k_h(T^{\tau-1} - T_a)\phi_i d\Gamma$$

$$- \begin{cases} \int_{\Gamma} h_a k_m(\rho^{\tau} - \rho_a)\phi_i d\Gamma, & \text{if } \mathbf{v} \cdot \hat{\mathbf{n}} < 0, \\ 0, & \text{if } \mathbf{v} \cdot \hat{\mathbf{n}} \geq 0. \end{cases} \tag{4.39}$$

4.1.5 The mass equation with SUPG method

The reasons to use SUPG (Streamline Upwind Petrov-Galerkin) method and the introduction of artificial diffusion into the system are discussed in the previous two chapters. Therefore, we briefly explain the SUPG part of the algorithm as applied for the $2D$ case. Let us consider Equation (4.20) with a test function $w = \phi + \psi$ where ϕ is the classical test function which ensures the consistency of the scheme and ψ denotes a correction term in order to take care of the upwind behavior. We obtain

$$
\int_\Omega \frac{\rho^\tau - \rho^{\tau-1}}{\Delta t} \phi d\Omega + \int_\Omega \frac{\rho^\tau - \rho^{\tau-1}}{\Delta t} \psi d\Omega = - \int_\Omega \boldsymbol{\nabla} \cdot (\rho^\tau \boldsymbol{v}^{\tau-1}) \phi d\Omega
$$
$$
- \int_\Omega \boldsymbol{\nabla} \cdot (\rho^\tau \boldsymbol{v}^{\tau-1}) \psi d\Omega, \qquad (4.40)
$$

or

$$
\int_\Omega \frac{\rho^\tau - \rho^{\tau-1}}{\Delta t} \phi d\Omega + \int_\Omega \frac{\rho^\tau - \rho^{\tau-1}}{\Delta t} \psi d\Omega = - \int_\Omega \boldsymbol{\nabla} \cdot (\rho^\tau \boldsymbol{v}^{\tau-1}) \phi d\Omega
$$
$$
- \int_\Omega \left\{ \rho^\tau \boldsymbol{\nabla} \cdot \boldsymbol{v}^{\tau-1} + \boldsymbol{v}^{\tau-1} \cdot \boldsymbol{\nabla}\rho \right\} \psi d\Omega. \quad (4.41)
$$

The first integral on the right-hand side can be written as

$$
- \int_\Omega \boldsymbol{\nabla} \cdot (\rho^\tau \boldsymbol{v}^{\tau-1}) \phi d\Omega = - \int_\Gamma \rho^\tau \boldsymbol{v}^{\tau-1} \cdot \hat{\boldsymbol{n}} \phi d\Gamma + \int_\Omega \rho^\tau \boldsymbol{v}^{\tau-1} \cdot \boldsymbol{\nabla}\phi d\Omega. \qquad (4.42)
$$

We neglect the term $\rho^\tau \boldsymbol{\nabla} \cdot \boldsymbol{v}^{\tau-1}$ because it has no significant effect on the numerical results [12]. Now, Equation (4.41) can be written as

$$
\int_\Omega \frac{\rho^\tau - \rho^{\tau-1}}{\Delta t} \phi d\Omega + \int_\Omega \frac{\rho^\tau - \rho^{\tau-1}}{\Delta t} \psi d\Omega = - \int_\Gamma \rho^\tau \boldsymbol{v}^\tau \cdot \hat{\boldsymbol{n}} d\Gamma + \int_\Omega \rho^\tau \boldsymbol{v}^{\tau-1} \cdot \boldsymbol{\nabla}\phi d\Omega
$$
$$
- \int_\Omega \left(\boldsymbol{v}^{\tau-1} \cdot \boldsymbol{\nabla}\rho^\tau \right) \psi d\Omega. \qquad (4.43)
$$

We choose

$$
\psi = \frac{\tilde{d}}{2} \frac{\boldsymbol{v} \cdot \boldsymbol{\nabla}\phi_i}{|\boldsymbol{v}|}, \quad |\boldsymbol{v}| > 0.
$$

We do not have to use SUPG in case of $|\boldsymbol{v}| = 0$. The value of $\tilde{d}$ depends on the direction of the velocity and element dimensions as shown in Figure 4.4. Its minimum possible value is the length of a side (Δx or Δy) and the maximum value can be the diagonal of the rectangular element ($\sqrt{(\Delta x)^2 + (\Delta y)^2}$). Using ψ and following the same steps as in the SGA method, we get a system of difference equations of the form

$$
M \frac{\rho^\tau - \rho^{\tau-1}}{\Delta t} = S^{(\rho)} \rho^\tau + \mathrm{f}^{(\rho)}, \qquad (4.44)
$$

where the mass matrix $M = M(\boldsymbol{v}^{\tau-1})$, for $i, j = \{1, ..., N\}$, is

$$M_{ij} = M_{ij}^{(1)} + \int_\Omega \left(\frac{\tilde{d}}{2} \frac{\boldsymbol{v}^{\tau-1} \cdot \boldsymbol{\nabla}\phi_i}{|\boldsymbol{v}^{\tau-1}|} \right) \phi_j d\Omega,$$

The stiffness matrix $S^{(\rho)}$ is given by

$$S_{ij}^{(\rho)} = S_{ij}^{(1)} - \int_\Omega \left(\boldsymbol{v}^{\tau-1} \cdot \boldsymbol{\nabla}\phi_j \right) \left(\frac{\tilde{d}}{2} \frac{\boldsymbol{v}^{\tau-1} \cdot \boldsymbol{\nabla}\phi_i}{|\boldsymbol{v}^{\tau-1}|} \right) d\Omega, \tag{4.45}$$

whereas the vector $\boldsymbol{f}^{(\rho)} = \boldsymbol{f}^{(1)}$.
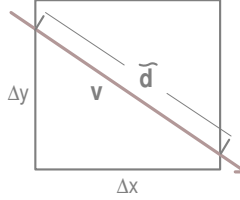
Figure 4.4: The value of $\tilde{d}$ depends on the direction of the velocity and element dimensions

4.1.6 The energy equation with SUPG method

For the energy equation, we get another system of difference equations of the form

$$M \frac{\boldsymbol{s}^\tau - \boldsymbol{s}^{\tau-1}}{\Delta t} = S^{(h)} \boldsymbol{s}^\tau + \boldsymbol{f}^{(h)}, \tag{4.46}$$

where M is already defined. The elements of $S^{(h)}$ and $\boldsymbol{f}^{(h)}$ are given as

$$S_{ij}^{(h)} = S_{ij}^{(2)} - \int_\Omega \left(\boldsymbol{v}^{\tau-1} \cdot \boldsymbol{\nabla}\phi_j \right) \left(\frac{\tilde{d}}{2} \frac{\boldsymbol{v}^{\tau-1} \cdot \boldsymbol{\nabla}\phi_i}{|\boldsymbol{v}^{\tau-1}|} \right) d\Omega, \tag{4.47}$$

$$f_i^{(h)} = f_i^{(2)} + \int_\Omega q_\tau \left(\frac{\tilde{d}}{2} \frac{\boldsymbol{v}^{\tau-1} \cdot \boldsymbol{\nabla}\phi_i}{|\boldsymbol{v}^{\tau-1}|} \right) d\Omega, \tag{4.48}$$

4.1.7 Darcy's law and thermodynamics relations

Once the pair (ρ, h) is determined, T, P, and X_G are computed by the numerical ρ-h diagrams as given in Figure 3.1. For the velocity variable, Darcy's law $\boldsymbol{v} = -\frac{K}{\mu}\boldsymbol{\nabla}P$ is discretized and written as a matrix equation

$$M^{(1)}\boldsymbol{v}^\tau = \boldsymbol{f}^{(v)}, \tag{4.49}$$

where

$$f_i^{(v)} = -\frac{K}{\mu} \int_\Omega \boldsymbol{\nabla} \cdot P^\tau \phi_i d\Omega.$$

Equation (4.44), (4.46) and (4.49) are solved by Gaussian elimination (i.e., a direct solver).

4.2 Numerical Experiments

For the $2D$ numerical experiments, we used $\Delta x = \Delta y = 1/40[m]$, $\Delta t = \frac{(\Delta x)^2}{10}$, and $k_m = k_h = 0$. This is already an excessively large computation. The purpose of the following experiments is to show that the model actually works in $2D$ and it is consistent with the $1D$ model.

4.2.1 Case Study 1: Inwardly isolated system

We set the following initial conditions

$$\begin{aligned} T(\boldsymbol{x}, 0) &= 291 - x, & \boldsymbol{x} \in \Omega, \\ X_G(\boldsymbol{x}, 0) &= 0.1, & \boldsymbol{x} \in \Omega. \end{aligned}$$

In this numerical experiment, we use $1D$ flow conditions and hence, it is possible to compare the results with the $1D$ model. The solution results of density and total enthalpy are provided in Figure 4.5 at two time instants. Other plots for the solution variables (like P, $\boldsymbol{v}$, X_G, etc), for this example (and for other examples) are given in [6]. The interpretation of the numerical results is given in Section 3.3.3. In Figure 4.6, we make a comparison between $1D$ and $2D$ models. For this purpose, we compute $\boldsymbol{\rho}^{(1D)}$ and $\boldsymbol{\rho}^{(2D)}$ and determine their relative difference as defined by Equation 2.5. Here $\boldsymbol{\rho}^{1D} = [\rho_j^{1D}]$ is the same as given by Figure 3.3(a) (Case Study 1) and ρ^{2D} is the cross-section of $\boldsymbol{\rho}$ as given in Figure 4.5(a). The relative difference in this case is less than 1 percent.

4.2.2 Inwardly isolated system with an initially inward velocity

In this experiment, we apply real $2D$ initial conditions $T(\boldsymbol{x}, 0)$ and $X_G(\boldsymbol{x}, 0)$ as shown in Figure 4.7. Again, the system is inwardly insolated ($k_m = k_h = 0$). The temperature and pressure is low at the central part of Ω therefore, heat and mass flow from all sides toward the central region due to Fourier and Darcy's laws. Such flow increases density and total enthalpy (and decreases X_G) in the central region with the progression of time. In Figure 4.8, we provide initial and steady-state values of variables ρ and s. For the plots of other variables, we refer to [6].
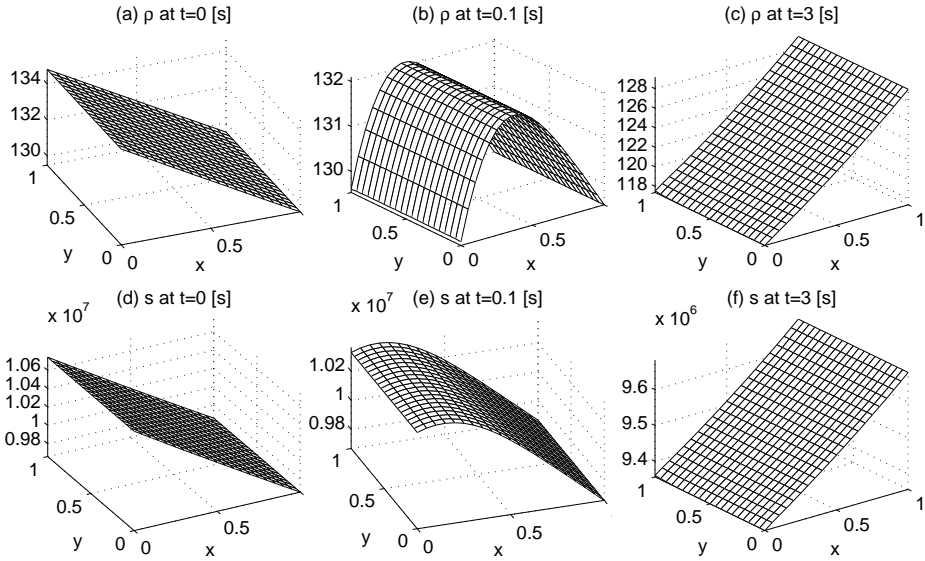
Figure 4.5: Inwardly isolated system with $k_m = 0$, $k_h = 0$. Solution plots of (a) density at 0.1 [s], (b) density at 3.0 [s], (c) total enthalpy at 0.1 [s], and (d) total enthalpy at 3.0 [s].
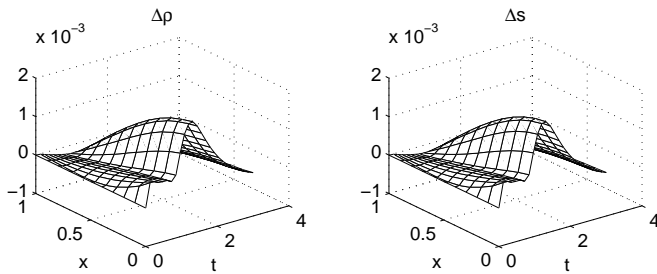
Figure 4.6: Inwardly isolated system with $k_m = 0$, $k_h = 0$. Solution plots of (left) point-wise relative difference of ρ^{1D} and ρ^{2D} defined by equation 2.5 and (right) relative total enthalpy Δs.
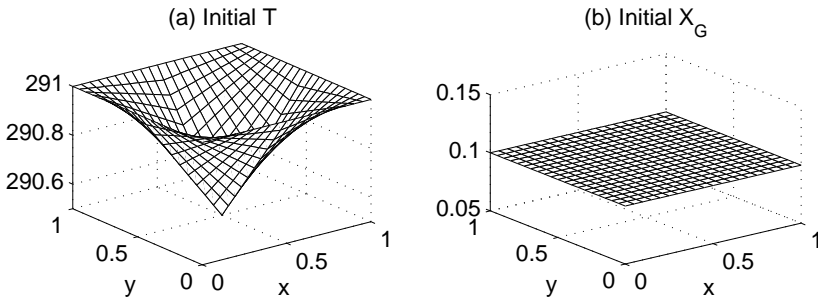
Figure 4.7: Case Study 2: Initial conditions for the inwardly isolated system ($k_m = k_h = 0$) with an initially inward velocity.
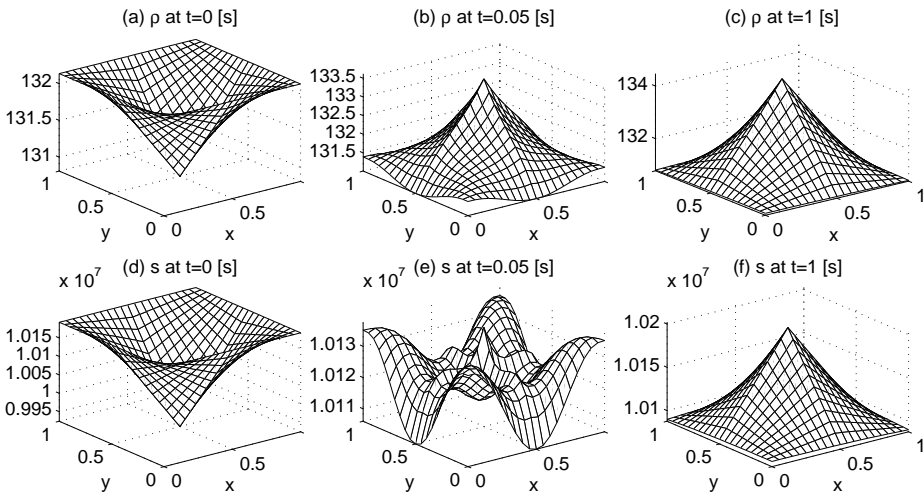
Figure 4.8: Case Study 2: Solution plots of (left) initial density and (right) density at 1.0 [s].

Chapter 5

An efficient time integration method

In this chapter, we discuss why it is necessary to use a small time-step. A small Δt is required for convergence, if an IMEX or the backward Euler time integration with the Picard's method to solve the resulting nonlinear problem are used. In the simulation sections, we show that the new solution algorithm works well, with large time-steps, and that it is consistent with respect to the dimensionality ($1D$ versus $2D$ model) and rotation (i.e., swapping the initial conditions along x- and y-axes). Furthermore, the position of the phase-front is compared with the position of a moving boundary based on a Stefan problem. The algorithm is tested on regular, quadrilateral and stretched grids. One test problem is provided where we include a gravity term in Darcy's law.

5.1 Time integration schemes

For the given system of nonlinear equations, we applied two linearization schemes in Chapters 3 and 4. A short review of these methods, in the context of the ρ-h model, is given in the following sections.

5.1.1 The time-step in IMplicit-EXplicit (IMEX) method

Let u^τ denote the approximation of the variable $u(\boldsymbol{x}, t)$ at $t = \tau \, \Delta t$. In this case the mass and energy equations are integrated in time, in the following manner

$$\frac{1}{\Delta t}(\rho^\tau - \rho^{\tau-1}) + \boldsymbol{\nabla} \cdot (\rho^\tau \boldsymbol{v}^{\tau-1}) = 0, \qquad \text{(mass equation)}, \qquad (5.1)$$

$$\frac{1}{\Delta t}(s^\tau - s^{\tau-1}) + \boldsymbol{\nabla} \cdot (s^\tau \boldsymbol{v}^{\tau-1}) - D\boldsymbol{\nabla} \cdot \boldsymbol{\nabla} T^{\tau-1} = 0, \qquad \text{(energy equation)}. \qquad (5.2)$$

With this linearization scheme, these equations are quasi-hyperbolic PDEs in the sense that the second order spatial derivatives only mimic a source term. Hence, the boundary conditions apply only when the mass flows into the system, i.e., if $v \cdot \hat{n} < 0$, where $\hat{n}$ is the unit normal at the boundary. The no-flux boundary conditions we used in Chapter 4, are written as

$$\rho^{\tau} v^{\tau-1} \cdot \hat{n} = \begin{cases} 0, & \text{if } v^{\tau-1} \cdot \hat{n} < 0, \\ \rho^{\tau} v^{\tau-1} \cdot \hat{n}, & \text{if } v^{\tau-1} \cdot \hat{n} > 0, \end{cases}$$

$$-D\frac{\partial T^{\tau-1}}{\partial \hat{n}} + s^{\tau} v^{\tau-1} \cdot \hat{n} = \begin{cases} 0, & \text{if } v^{\tau-1} \cdot \hat{n} < 0, \\ s^{\tau} v^{\tau-1} \cdot \hat{n}, & \text{if } v^{\tau-1} \cdot \hat{n} > 0. \end{cases}$$

Since the diffusion term in Equation (5.2) is treated explicitly, the time step Δt is bounded by some δ_b i.e.,

$$\Delta t \leq \delta_b.$$

For a linear diffusion PDE

$$\frac{\partial \rho}{\partial t} - D\mathbf{\nabla} \cdot \mathbf{\nabla}\rho = 0,$$

a necessary condition for the solution convergence is [17]

$$\delta_b = \frac{(\Delta x)^2 (\Delta y)^2}{2D[(\Delta x)^2 + (\Delta y)^2]}.$$

This is true for a rectangular mesh with finite differences, where Δx and Δy are spatial step sizes in respective directions. A similar relation can be derived for finite-element discretization. The upper bound for Δt as determined for a convection-diffusion equation, serves as an estimate for Δt to be used in our nonlinear system of PDEs, with the IMEX time integration. This relation shows that a high resolution mesh would result in a small time step which leads to an excessive computation time. In order to overcome this difficulty with the choice of Δt, we tried Picard iteration in Chapter 3.

5.1.2 The time step in Picard's iteration method

By using the Picard method, the time integration of the energy equation is given by

$$\frac{1}{\Delta t}(s^{\tau,p} - s^{\tau-1}) + \mathbf{\nabla} \cdot (s^{\tau,p} v^{\tau,p-1}) - D\mathbf{\nabla} \cdot \mathbf{\nabla}T^{\tau,p-1} = 0,$$

where τ is the current value of the time loop index and p is the Picard loop index. Note that the diffusion term is taken at the previous Picard iteration. For the weak formulation and standard Galerkin algorithm for this equation, we refer to Chapter 4. At the start of a Picard iteration, an initial guess for the solution variables is required. In our solution algorithm, the initial guess is the solution variables at $\tau - 1$ (e.g., the

variable $T^{\tau,p-1}$ is assigned the value $T^{\tau-1}$). Therefore the energy equation has actually the following form at the start of each Picard loop, when $p = 1$

$$\frac{1}{\Delta t}(s^{\tau,1} - s^{\tau-1}) + \boldsymbol{\nabla} \cdot (s^{\tau,1} \, \boldsymbol{v}^{\tau-1}) - D\boldsymbol{\nabla} \cdot \boldsymbol{\nabla} T^{\tau-1} = 0.$$

Again, the diffusion term is explicit in τ and therefore the upper bound for Δt as discussed in the IMEX case applies here as well. Hence, the Picard iteration in this case does not offer any advantage over IMEX with respect to choosing a larger Δt. Again, we have $\Delta t = O(\Delta x^2) + O(\Delta y^2)$. This motivates us to use a fully-implicit time integration scheme, for example the Newton-Raphson method.

5.1.3 Newton-Raphson iteration

Let the nonlinearly coupled system of equations as given in Section 4.1 be arranged in the homogeneous form

$$\boldsymbol{F}(\boldsymbol{G}) = \boldsymbol{0},$$

where $\boldsymbol{F}$ and $\boldsymbol{G}$ are vectors of the same dimension. The vector $\boldsymbol{G}$ is the required solution set and $\boldsymbol{F}$ represents the set of relations between them (Equations (4.1) to (4.5)). The Taylor expansion of $\boldsymbol{F}(\boldsymbol{G})$ about $\boldsymbol{G}^k$ (for some k) is expressed as

$$\boldsymbol{F}(\boldsymbol{G}^k) + \frac{\partial \boldsymbol{F}}{\partial \boldsymbol{G}}\bigg|_{\boldsymbol{G}=\boldsymbol{G}^k} \delta\boldsymbol{G} + \frac{1}{2} \, \delta\boldsymbol{G}^T \, \frac{\partial^2 \boldsymbol{F}}{\partial \boldsymbol{G}^2}\bigg|_{\boldsymbol{G}=\boldsymbol{G}^k} \delta\boldsymbol{G} + ... = \boldsymbol{0},$$

where $\delta\boldsymbol{G} = \boldsymbol{G}^{k+1} - \boldsymbol{G}^k$, $J = \frac{\partial \boldsymbol{F}}{\partial \boldsymbol{G}}\big|_{\boldsymbol{G}=\boldsymbol{G}^k}$ is the Jacobian matrix, and $\frac{\partial^2 \boldsymbol{F}}{\partial \boldsymbol{G}^2}\big|_{\boldsymbol{G}=\boldsymbol{G}^k}$ is the Hessian matrix. Assuming that $\boldsymbol{F}(\boldsymbol{G})$ is sufficiently smooth in the neighborhood of $\boldsymbol{G}^k$, we approximate $\boldsymbol{F}(\boldsymbol{G})$ by the first two terms of its Taylor's expansion. This leads to

$$\boldsymbol{F}(\boldsymbol{G}^k) + J \, (\boldsymbol{G}^{k+1} - \boldsymbol{G}^k) = \boldsymbol{0},$$

or

$$\boldsymbol{G}^{k+1} = \boldsymbol{G}^k - J^{-1}\boldsymbol{F}(\boldsymbol{G}^k).$$

Hence, the linearization actually leads to a Newton-Raphson iteration making k as index of the Newton loop. For a programming point of view, we execute the Newton loop for each time iteration τ. Depending on the running error ϵ_r and the error tolerance ϵ_{min}, we examine whether convergence has been reached or whether the loop should be continued or stopped if the solution diverges.

5.2   Newton-Raphson method applied to the $2D$ system

The mathematical model for the $2D$ flow system is mentioned in Section 4.1. The boundary conditions, in the continuous form are the following

$$\rho \mathbf{v} \cdot \hat{\mathbf{n}} = 0, \qquad \text{(for mass equation)}, \qquad (5.3)$$

$$-D\frac{\partial T}{\partial \hat{\mathbf{n}}} + s\mathbf{v} \cdot \hat{\mathbf{n}} = 0, \qquad \text{(for energy equation)}, \qquad (5.4)$$

Now, we show that the mass and energy equations do not have a quasi-hyperbolic structure in the continuous problem. Consequently, it is necessary to use boundary conditions on each point of the boundary. To make this point clear, consider the mass equation

$$\frac{\partial \rho}{\partial t} + \mathbf{\nabla} \cdot (\rho \mathbf{v}) = 0.$$

Using $\mathbf{v} = -\frac{K}{\mu}\mathbf{\nabla}P$ in this equation. We get

$$\frac{\partial \rho}{\partial t} - \frac{K}{\mu}\mathbf{\nabla} \cdot (\rho \, \mathbf{\nabla}P) = 0. \qquad (5.5)$$

Using the differential of $P(\rho, h)$

$$\mathbf{\nabla}P = \frac{\partial P}{\partial \rho}\mathbf{\nabla}\rho + \frac{\partial P}{\partial h}\mathbf{\nabla}h,$$

into Equation (5.5). This yields

$$\frac{\partial \rho}{\partial t} - \frac{K}{\mu}\mathbf{\nabla} \cdot \left[\rho\left(\frac{\partial P}{\partial \rho}\mathbf{\nabla}\rho + \frac{\partial P}{\partial h}\mathbf{\nabla}h\right)\right] = 0.$$

Hence, we have shown that the mass equation indirectly contains a diffusion term in ρ and therefore it can not be considered as a hyperbolic partial differential equation. The same holds for a purely implicit time integration. An analogous derivation can be carried out for the energy equation.

5.2.1   Numerical treatment of the mass equation

We use the Euler backward method for time integration of the mass equation (Equation (4.1)) and take all the variables implicitly

$$\frac{1}{\Delta t}(\rho^\tau - \rho^{\tau-1}) + \mathbf{\nabla} \cdot (\rho^\tau \mathbf{v}^\tau) = 0, \quad \tau = \{1, 2, .., \tau_{max}\}, \qquad (5.6)$$

In order to get the weak formulation, we multiply the above equation by a test function ϕ, and integrate over Ω

$$\frac{1}{\Delta t}\int_\Omega (\rho^\tau - \rho^{\tau-1})\phi \, d\Omega + \int_\Omega \mathbf{\nabla} \cdot (\rho^\tau \mathbf{v}^\tau)\phi \, d\Omega = 0, \qquad (5.7)$$

where τ is a time index. By using the vector product rule and the divergence theorem (see Section 4.1.3), we obtain

$$\frac{1}{\Delta t} \int_\Omega (\rho^\tau - \rho^{\tau-1})\phi d\Omega + \int_\Gamma \rho^\tau \boldsymbol{v}^\tau \phi \cdot \hat{\boldsymbol{n}} d\Gamma - \int_\Omega \rho^\tau \boldsymbol{v}^\tau \cdot \boldsymbol{\nabla}\phi d\Omega = 0. \qquad (5.8)$$

We apply the boundary condition, which makes the second integral equal to zero, and then linearize this equation about $\rho^{\tau,k}$ and $\boldsymbol{v}^{\tau,k}$. The resulting nonlinear partial differential equation is solved by a Newton method based on successive linearization of the PDE. This gives

$$\frac{1}{\Delta t} \int_\Omega \delta\rho\, \phi(\boldsymbol{x})\, d\Omega + \frac{1}{\Delta t} \int_\Omega (\rho^k - \rho^{\tau-1})\phi(\boldsymbol{x})\, d\Omega - \int_\Omega (\rho^k v_x^k + v_x^k \delta\rho + \rho^k \delta v_x)\frac{\partial\phi}{\partial x}\, d\Omega$$

$$- \int_\Omega (\rho^k v_y^k + v_y^k \delta\rho + \rho^k \delta v_y)\frac{\partial\phi}{\partial y}\, d\Omega = 0,$$

where $\delta\rho = \rho^{k+1} - \rho^k$, $\delta v_x = v_x^{k+1} - v_x^k$, and $\delta v_y = v_y^{k+1} - v_y^k$. For a better readability, we omit the index τ but it is understood to be there (e.g., ρ^k actually represents $\rho^{\tau,k}$). We choose a set of basis functions $\{\phi_i\}_N$ and apply the approximation $\delta\rho(\boldsymbol{x},\tau) \approx \sum_{j=1}^N \delta\rho_j(\tau)\,\phi_j(\boldsymbol{x})$, $\delta v_x(\boldsymbol{x},\tau) \approx \sum_{j=1}^N \delta v_{x,j}(\tau)\,\phi_j(\boldsymbol{x})$, and $\delta v_y(\boldsymbol{x},\tau) \approx \sum_{j=1}^N \delta v_{y,j}(\tau)\,\phi_j(\boldsymbol{x})$. After substitution into the weak form and choosing $\phi = \phi_i$, for $i = 1, ..., N$, we obtain

$$\frac{1}{\Delta t}\sum_{j=1}^N \delta\rho_j \int_\Omega \phi_i\phi_j\, d\Omega + \frac{1}{\Delta t}\int_\Omega (\rho^k - \rho^{\tau-1})\phi_i\, d\Omega$$

$$- \int_\Omega \rho^k v_x^k \frac{\partial\phi_i}{\partial x} d\Omega - \sum_{j=1}^N \delta\rho_j \int_\Omega v_x^k \phi_j \frac{\partial\phi_i}{\partial x}\, d\Omega - \sum_{j=1}^N \delta v_{x,j} \int_\Omega \rho^k \phi_j \frac{\partial\phi_i}{\partial x}\, d\Omega$$

$$- \int_\Omega \rho^k v_y^k \frac{\partial\phi_i}{\partial y} d\Omega - \sum_{j=1}^N \delta\rho_j \int_\Omega v_y^k \phi_j \frac{\partial\phi_i}{\partial y}\, d\Omega - \sum_{j=1}^N \delta v_{y,j} \int_\Omega \rho^k \phi_j \frac{\partial\phi_i}{\partial y}\, d\Omega = 0. \quad (5.9)$$

The matrix form of the above equation is given by

$$S^{(11)}\,\delta\boldsymbol{\rho} + S^{(12)}\,\delta\boldsymbol{v}_x + S^{(13)}\,\delta\boldsymbol{v}_y + \boldsymbol{f}^{(\rho)} = \boldsymbol{0}. \qquad (5.10)$$

By comparing Equations (5.9) and (5.10), the elements of the global matrices and vector are defined as

$$S_{ij}^{(11)} = \frac{1}{\Delta t}\int_\Omega \phi_i\phi_j d\Omega - \int_\Omega v_x^k \phi_j \frac{\partial\phi_i}{\partial x} d\Omega - \int_\Omega v_y^k \phi_j \frac{\partial\phi_i}{\partial y} d\Omega,$$

$$S_{ij}^{(22)} = -\int_\Omega \rho^k \phi_j \frac{\partial\phi_i}{\partial x}\, d\Omega,$$

$$S_{ij}^{(23)} = -\int_\Omega \rho^k \phi_j \frac{\partial\phi_i}{\partial y}\, d\Omega,$$

$$\boldsymbol{f}_i^{(\rho)} = \frac{1}{\Delta t}\int_\Omega (\rho^k - \rho^{\tau-1})\phi_i\, d\Omega - \int_\Omega \rho^k v_x^k \frac{\partial\phi_i}{\partial x} d\Omega - \int_\Omega \rho^k v_y^k \frac{\partial\phi_i}{\partial y} d\Omega.$$

We use the Newton-Cotes quadrature rule given by Equation (4.19), to determine the integrals in the above expressions, on a unit square. Iso-parametric transformation is discussed in Chapter 4.

5.2.2   Integration of the energy equation

We denote $s = \rho h$ and proceed analogously, as mentioned for the mass equation, in order to obtain the weak formulation for the $2D$ energy equation (Equation (4.2)). We start with the time integration (Euler Backward method),

$$\frac{s^\tau - s^{\tau-1}}{\Delta t} + \boldsymbol{\nabla} \cdot (s^\tau \boldsymbol{v}^\tau) - \boldsymbol{\nabla} \cdot (D\boldsymbol{\nabla} T^\tau) = 0. \tag{5.11}$$

No heat source is considered, i.e. $q = 0$. The weak form is given by

$$\int_\Omega \frac{s^\tau - s^{\tau-1}}{\Delta t} \phi d\Omega + \int_\Omega \boldsymbol{\nabla} \cdot (s^\tau \boldsymbol{v}^\tau) \phi d\Omega - \int_\Omega \boldsymbol{\nabla} \cdot (D\boldsymbol{\nabla} T^\tau) \phi d\Omega = 0. \tag{5.12}$$

By substituting

$$\int_\Omega \boldsymbol{\nabla} \cdot (s\boldsymbol{v}) \phi d\Omega = -\int_\Gamma s\phi \boldsymbol{v} \cdot \hat{\boldsymbol{n}} d\Gamma + \int_\Omega s\boldsymbol{v} \cdot \boldsymbol{\nabla}\phi d\Omega, \tag{5.13}$$

and using

$$\int_\Omega \boldsymbol{\nabla} \cdot (D\boldsymbol{\nabla} T)\phi d\Omega = \int_\Gamma D\frac{\partial T}{\partial \hat{\boldsymbol{n}}} \phi d\Gamma - \int_\Omega D\boldsymbol{\nabla} T \cdot \boldsymbol{\nabla}\phi d\Omega, \tag{5.14}$$

into equation (5.12), we get

$$\int_\Omega \frac{s^\tau - s^{\tau-1}}{\Delta t} \phi d\Omega + \int_\Gamma s^\tau \phi \boldsymbol{v}^\tau \cdot \hat{\boldsymbol{n}} d\Gamma - \int_\Omega s^\tau \boldsymbol{v}^\tau \cdot \boldsymbol{\nabla}\phi d\Omega$$
$$- \int_\Gamma D\frac{\partial T^\tau}{\partial \hat{\boldsymbol{n}}} \phi d\Gamma + \int_\Omega D\boldsymbol{\nabla} T^\tau \cdot \boldsymbol{\nabla}\phi d\Omega = 0. \tag{5.15}$$

We apply the boundary condition as given by Equation (5.4) which eliminates integrals containing boundary terms. Hence, we obtain

$$\int_\Omega \frac{s^\tau - s^{\tau-1}}{\Delta t} \phi d\Omega - \int_\Omega s^\tau v_x^\tau \frac{\partial \phi}{\partial x} d\Omega - \int_\Omega s^\tau v_y^\tau \frac{\partial \phi}{\partial y} d\Omega + D \int_\Omega \left(\frac{\partial T}{\partial x} \frac{\partial \phi}{\partial x} + \frac{\partial T}{\partial y} \frac{\partial \phi}{\partial y} \right) d\Omega = 0.$$

We linearize these terms about s^k, T^k, v_x^k and v_y^k to get

$$\frac{1}{\Delta t} \int_\Omega \delta s\, \phi d\Omega \ + \frac{1}{\Delta t} \int_\Omega (s^k - s^{\tau-1}) \phi d\Omega \ - \int_\Omega (s^k v_x^k + v_x^k \delta s + s^k \delta v_x) \frac{\partial \phi}{\partial x} d\Omega$$
$$- \int_\Omega (s^k v_y^k + v_y^k \delta s + s^k \delta v_y) \frac{\partial \phi}{\partial y} d\Omega \ + D \int_\Omega \left[\frac{\partial}{\partial x} \left(\delta T + T^k \right) \frac{\partial \phi}{\partial x} + \frac{\partial}{\partial y} \left(\delta T + T^k \right) \frac{\partial \phi}{\partial y} \right] d\Omega = 0,$$

where δv_x and δv_y were defined previously whereas $\delta s = s^{k+1} - s^k$ and $\delta T = T^{k+1} - T^k$. We apply the approximations $\delta s(\boldsymbol{x}, \tau) \approx \sum_{j=1}^N \delta s_j(\tau)\phi_j(\boldsymbol{x})$ and $\delta T(\boldsymbol{x}, \tau) \approx \sum_{j=1}^N \delta T_j(\tau)\phi_j(\boldsymbol{x})$

to the weak form and hence we obtain

$$\frac{1}{\Delta t}\sum_{j=1}^{N}\delta s_j \int_{\Omega}\phi_i\phi_j\,d\Omega+\frac{1}{\Delta t}\int_{\Omega}(s^k-s^{\tau-1})\phi_i\,d\Omega$$

$$-\int_{\Omega}s^k v_x^k \frac{\partial\phi_i}{\partial x}d\Omega-\sum_{j=1}^{N}\delta s_j\int_{\Omega}v_x^k\phi_j\frac{\partial\phi_i}{\partial x}\,d\Omega-\sum_{j=1}^{N}\delta v_{x,j}\int_{\Omega}s^k\phi_j\frac{\partial\phi_i}{\partial x}\,d\Omega$$

$$-\int_{\Omega}s^k v_y^k \frac{\partial\phi_i}{\partial y}d\Omega-\sum_{j=1}^{N}\delta s_j\int_{\Omega}v_y^k s_j\frac{\partial\phi_i}{\partial y}\,d\Omega-\sum_{j=1}^{N}\delta v_{y,j}\int_{\Omega}s^k\phi_j\frac{\partial\phi_i}{\partial y}\,d\Omega$$

$$+D\sum_{j=1}^{N}\delta T_j\int_{\Omega}\left(\frac{\partial\phi_i}{\partial x}\frac{\partial\phi_j}{\partial x}+\frac{\partial\phi_i}{\partial y}\frac{\partial\phi_j}{\partial y}\right)d\Omega+D\int_{\Omega}\left(\frac{\partial T^k}{\partial x}\frac{\partial\phi_i}{\partial x}+\frac{\partial T^k}{\partial y}\frac{\partial\phi_i}{\partial y}\right)d\Omega=0.$$

The equivalent matrix form of the above equation is given by

$$S^{(21)}\,\delta s+S^{(22)}\,\delta v_x+S^{(23)}\,\delta v_y+f^{(s)}+S^{(24)}\,\delta T=0, \qquad (5.16)$$

where $S^{(21)}=S^{(11)}$ is already defined. The remaining element matrices and vector are determined in the following way

$$S_{ij}^{(22)}=-\int_{\Omega}s^k\phi_j\frac{\partial\phi_i}{\partial x}\,d\Omega,$$

$$S_{ij}^{(23)}=-\int_{\Omega}s^k\phi_j\frac{\partial\phi_i}{\partial y}\,d\Omega,$$

$$S_{ij}^{(24)}=D\int_{\Omega}\left(\frac{\partial\phi_i}{\partial x}\frac{\partial\phi_j}{\partial x}+\frac{\partial\phi_i}{\partial y}\frac{\partial\phi_j}{\partial y}\right)d\Omega,$$

$$f_i^{(s)}=\frac{1}{\Delta t}\int_{\Omega}(s^k-s^{\tau-1})\phi_i d\Omega-\int_{\Omega}s^k v_x^k\frac{\partial\phi_i}{\partial x}d\Omega$$

$$-\int_{\Omega}s^k v_y^k\frac{\partial\phi_i}{\partial y}d\Omega+D\int_{\Omega}\left(\frac{\partial T^k}{\partial x}\frac{\partial\phi_i}{\partial x}+\frac{\partial T^k}{\partial y}\frac{\partial\phi_i}{\partial y}\right)d\Omega.$$

5.2.3 The treatment of Darcy's law

The horizontal component of Darcy's law is given by

$$v_x+\frac{K}{\mu}\frac{\partial P}{\partial x}=0.$$

At time step τ, the weak formulation is given by

$$\int_{\Omega}v_x^{\tau}\phi d\Omega+\frac{K}{\mu}\int_{\Omega}\frac{\partial P^{\tau}}{\partial x}\phi d\Omega=0.$$

The linearization of this equation gives

$$\int_{\Omega}\left(\delta v_x+v_x^k\right)\phi d\Omega+\frac{K}{\mu}\int_{\Omega}\frac{\partial}{\partial x}(\delta P+P^k)\phi d\Omega=0.$$

The spatial discretization applied to the above equation yields

$$\sum_{j=1}^{N} \delta v_{x,j} \int_{\Omega} \phi_i \phi_j d\Omega + \int_{\Omega} v_x^k \phi_i d\Omega$$

$$+ \frac{K}{\mu} \sum_{j=1}^{N} \delta P_j \int_{\Omega} \frac{\partial \phi_j}{\partial x} \phi_i d\Omega + \frac{K}{\mu} \int_{\Omega} \frac{\partial P^k}{\partial x} \phi_i d\Omega = 0,$$

with the following matrix form

$$S^{(31)} \delta v_x + S^{(32)} \delta P + f^{(u)} = 0.$$

The elements of the matrices and vector are given by

$$S_{ij}^{(31)} = \int_{\Omega} \phi_i \phi_j d\Omega,$$

$$S_{ij}^{(32)} = \frac{K}{\mu} \int_{\Omega} \frac{\partial \phi_j}{\partial x} \phi_i d\Omega,$$

$$f_i^{(u)} = \int_{\Omega} v_x^k \phi_i d\Omega + \frac{K}{\mu} \int_{\Omega} \frac{\partial P^k}{\partial x} \phi_i d\Omega.$$

The treatment of the vertical component of Darcy's Law is analogous, and gives the matrix form

$$S^{(41)} \delta v_x + S^{(42)} \delta P + f^{(v)} = 0,$$

where $S^{(41)} = S^{(31)}$. The elements of the matrix $S^{(42)}$ and the vector $f^{(v)}$ are given by

$$S_{ij}^{(42)} = \frac{K}{\mu} \int_{\Omega} \frac{\partial \phi_j}{\partial y} \phi_i d\Omega,$$

$$f_i^{(v)} = \int_{\Omega} v_y^k \phi_i d\Omega + \frac{K}{\mu} \int_{\Omega} \frac{\partial P^k}{\partial y} \phi_i d\Omega.$$

In a later section, we add the gravity term to the y-component of the Darcy's law.

5.2.4 Thermodynamical relations for the temperature and pressure

We obtain the temperature (and pressure) vector by using the density and enthalpy values through available phase diagrams, i.e.,

$$T = T(\rho, h).$$

In this case, the linearization step results into

$$T^k - T(\rho^k, h^k) + \delta T - \frac{\partial T}{\partial \rho} \delta \rho - \frac{\partial T}{\partial h} \delta h = 0,$$

where $\frac{\partial T}{\partial \rho}$ is approximated by

$$\frac{\partial T}{\partial \rho} \approx \frac{T(\rho^k + \epsilon, h^k) - T(\rho^k, h^k)}{\epsilon}.$$

Here ϵ is a suitable small number (we use $\epsilon = .001$). The approximation for $\frac{\partial T}{\partial h}$ is analogous. Now, the spatial discretization takes the following form

$$I \, \delta T + S^{(51)} \, \delta \rho + S^{(52)} \, \delta h + f^{(T)} = 0. \tag{5.17}$$

Here I is an identity matrix whereas $S^{(51)}$ and $S^{(52)}$ are diagonal matrices

$$S_{ij}^{(51)} = -\frac{\partial T}{\partial \rho} \quad = -\frac{T(\rho_i^k + \epsilon, h_i^k) - T(\rho_i^k, h_i^k)}{\epsilon} \delta_{ij},$$

$$S_{ij}^{(52)} = -\frac{\partial T}{\partial h} \quad = -\frac{T(\rho_i^k, h_i^k + \epsilon) - T(\rho_i^k, h_i^k)}{\epsilon} \delta_{ij},$$

$$f_i^{(T)} = T_i^k - T(\rho_i^k, h_i^k),$$

where δ_{ij} represents the Kronecker Delta. For the pressure variable, we have

$$P = P(\rho, h).$$

The linearization procedure is similar to the temperature case, i.e.,

$$P^k - P(\rho^k, h^k) + \delta P - \frac{\partial P}{\partial \rho} \delta \rho - \frac{\partial P}{\partial h} \delta h = 0,$$

The matrix form is

$$I \, \delta P + S^{(61)} \, \delta \rho + S^{(62)} \, \delta h + f^{(P)} = 0. \tag{5.18}$$

Again, $S^{(61)}$ and $S^{(62)}$ are diagonal matrices. These matrices and the vector $f^{(P)}$ are defined as

$$S_{ij}^{(61)} = -\frac{\partial P}{\partial \rho} \quad = -\frac{P(\rho_i^k + \epsilon, h_i^k) - P(\rho_i^k, h_i^k)}{\epsilon} \delta_{ij},$$

$$S_{ij}^{(62)} = -\frac{\partial P}{\partial h} \quad = -\frac{P(\rho_i^k, h_i^k + \epsilon) - P(\rho_i^k, h_i^k)}{\epsilon} \delta_{ij},$$

$$f_i^{(P)} = P_i^k - P(\rho_i^k, h_i^k).$$

5.2.5 The density, enthalpy and total enthalpy relation

The relation between the density, enthalpy, and total enthalpy is given by

$$s = \rho h. \tag{5.19}$$

Linearization of this equation is given as

$$s^k - \rho^k h^k + \delta s - \rho^k \delta h - h^k \delta \rho = 0. \tag{5.20}$$

The matrix form is

$$I \, \delta s + S^{(71)} \, \delta \rho + S^{(72)} \, \delta h + f^{(h)} = 0, \tag{5.21}$$

where

$$S_{ij}^{(71)} = -h_i^k \delta_{ij},$$
$$S_{ij}^{(72)} = -\rho_i^k \delta_{ij},$$
$$f_i^{(h)} = s_i^k - \rho_i^k h_i^k.$$

5.2.6   Implementation of the Newton iteration scheme

To summarize, we solve the following set of equations

$$
\begin{aligned}
S^{(11)} \, \delta\rho + S^{(12)} \, \delta v_x + S^{(13)} \, \delta v_y + f^{(\rho)} &= 0, & \text{(mass equation)}, \\
S^{(21)} \, \delta s + S^{(22)} \, \delta v_x + S^{(23)} \, \delta v_y + S^{(24)} \, \delta T + f^{(s)} &= 0, & \text{(energy equation)}, \\
S^{(31)} \, \delta v + S^{(32)} \, \delta P + f^{(u)} &= 0, & \text{(Darcy's law, x-axis)}, \\
S^{(41)} \, \delta v + S^{(42)} \, \delta P + f^{(v)} &= 0, & \text{(Darcy's law, y-axis)}, \\
I \, \delta T + S^{(51)} \, \delta\rho + S^{(52)} \, \delta h + f^{(T)} &= 0, & (T = T(\rho, h)), \\
I \, \delta P + S^{(61)} \, \delta\rho + S^{(62)} \, \delta h + f^{(P)} &= 0, & (P = P(\rho, h)), \\
I \, \delta s + S^{(71)} \, \delta\rho + S^{(72)} \, \delta h + f^{(h)} &= 0, & (s = \rho h).
\end{aligned}
$$

For a Newton Raphson loop, the Jacobian is expressed in the following block matrix form

$$
J = \begin{bmatrix}
S^{(11)} & 0 & S^{(12)} & S^{(13)} & 0 & 0 & 0 \\
0 & S^{(21)} & S^{(22)} & S^{(23)} & S^{(24)} & 0 & 0 \\
0 & 0 & S^{(31)} & 0 & 0 & S^{(32)} & 0 \\
0 & 0 & 0 & S^{(41)} & 0 & S^{(42)} & 0 \\
S^{(51)} & 0 & 0 & 0 & I & 0 & S^{(52)} \\
S^{(61)} & 0 & 0 & 0 & 0 & I & S^{(62)} \\
S^{(71)} & I & 0 & 0 & 0 & 0 & S^{(72)}
\end{bmatrix}_{7N \times 7N},
$$

$$
F = \begin{bmatrix}
f^{(\rho)} \\
f^{(s)} \\
f^{(u)} \\
f^{(v)} \\
f^{(T)} \\
f^{(P)} \\
f^{(h)}
\end{bmatrix}_{7N \times 1}, \qquad
G^k = \begin{bmatrix}
\rho^k \\
s^k \\
v_x^k \\
v_y^k \\
T^k \\
P^k \\
h^k
\end{bmatrix}_{7N \times 1}.
$$

Finally, the Newton Raphson loop is given by,

$$G^{k+1} = G^k - J^{-1}F. \tag{5.22}$$

where J^{-1} is computed by Gaussian elimination.

5.3   Numerical Experiments

A number of case studies are provided and discussed in this section. We assume no heat source ($q = 0$) for the given examples. The stability of the PDE-problem is investigated in Chapter 6. For the test problems presented in this chapter, the method is found to be unconditionally stable. The value of Δt can be chosen equal to the process time (t_p) and hence the system can be solved in one time step (with few Newton-Raphson iterations). So the reasons to choose a relatively small Δt are only given by accuracy or the desire to follow the kinetics of the process. Therefore, we select a suitably small Δt to observe the variables profile in the transitional stage.

   To highlight the computation time gain in Newton-Raphson approach with respect to Picard iteration, we solve a flow example by these two approaches. We summarize the settings (parameters, initial conditions etc.) and the result (the simulation times) in Table 5.1. The upper part of the table is divided into three columns. The first column contains the labels for the parameters and the simulation time. The second and third column belong to Picard and Newton-Raphson approaches, respectively. Since the Picard approach, for our system, requires a small time step for convergence, the simulation time is very large[1] (≈ 86400 [s]) as compared to the simulation time with Newton approach (120 [s]). In other words, the Picard approach takes 24 hours, whereas the Newton-Raphson scheme requires two minutes for solving a problem with the same grid size.

   For a 100×100 grid, the Picard approach is impractical to be used, due to a very large computation time. On the other hand, the Newton-Raphson approach allows a time-step which is independent of the grid size. The grid size used for the simulation examples in the following sections is up to 200×200 nodes. All the following examples are computed using the Newton-Raphson iteration for linearization.

   Furthermore, we apply initial conditions consistent to the no-flux boundary conditions. That is, we set $X_G(\boldsymbol{x}, 0)$ and $T(\boldsymbol{x}, 0)$ such that $\hat{\boldsymbol{n}} \cdot \boldsymbol{v}(\boldsymbol{x}, 0) = 0$ for $\boldsymbol{x} \in \Gamma$. Note that dynamics of the system variables are already explained in Section 4.2. Therefore, in the current section, we will focus on other aspects of the numerical ρ-h approach such as consistency, phase front tracking, and a qualitative comparison with the solution of a Stefan problem for multi-phase problems.

5.3.1   Case Study 1. Piecewise linear $1D$ conditions with $2D$ model

In this case study, we show that the solution algorithm for $1D$ and $2D$ models are consistent. For this purpose, we use $1D$ initial conditions. These conditions and other

---

[1]The simulation times are obtained by using a 2.4 GHz processor, Windows 7 operating system and Matlab 7.3

Table 5.1: Example: Comparing Picard and Newton approaches

	Picard Approach	Newton Approach
N_x	41	41
N_y	41	41
Δt	1/16000	1/10
Process time t_p [s]	1	1
Simulation time [s]	86400	120
Stability condition	$\Delta t \leq \min(\Delta x, \Delta y)^2/10$	nil

$$T(x,0) = 290 + 2x$$
$$X_G(x,0) = 0.1$$

Table 5.2: Case Study 1

N_x	N_y	Δt	ϵ_r	K [m^2]	μ [$Pa.s$]
100	100	1/10	10^{-6}	5×10^{-11}	5×10^{-5}

$$T(\boldsymbol{x},0) = \begin{cases} 290, & \text{for } x \in [0, 0.05], \ y \in [0,1], \\ 290 + \frac{10}{9}x - \frac{1}{18}, & \text{for } x \in]0.05, 0.95], \ y \in [0,1], \\ 291, & \text{for } x \in]0.95, 1], \ y \in [0,1], \end{cases}$$
$$X_G(x,0) = 0.1$$
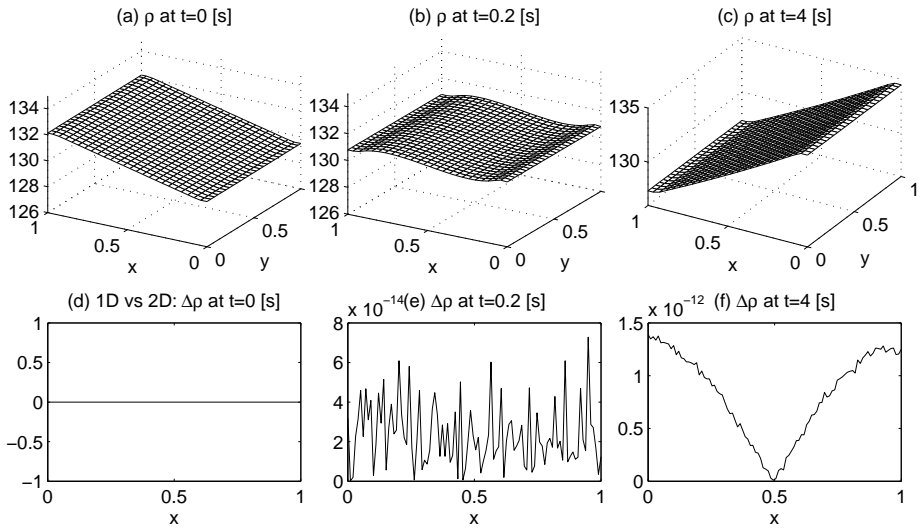
Figure 5.1: Case study 1. Solution plots of the 2D fluid system with piecewise linear initial conditions in T along x-axis, with $\Delta t = 1/10$, $\Delta x = 1/99$, and $\epsilon_r = 10^{-6}$. The solution plots are (a) the density ρ at $t = 0$ [s], (b) ρ at $t = 0.2$ [s], (c) ρ at $t = 4$ [s], (d) Relative difference $\Delta\rho$ (definition of Equation (2.5)) between ρ^{2D} and ρ^{1D} at $t = 0$, (e) $\Delta\rho$ at $t = 0.2$ [s], and (f) $\Delta\rho$ at $t = 4$ [s].
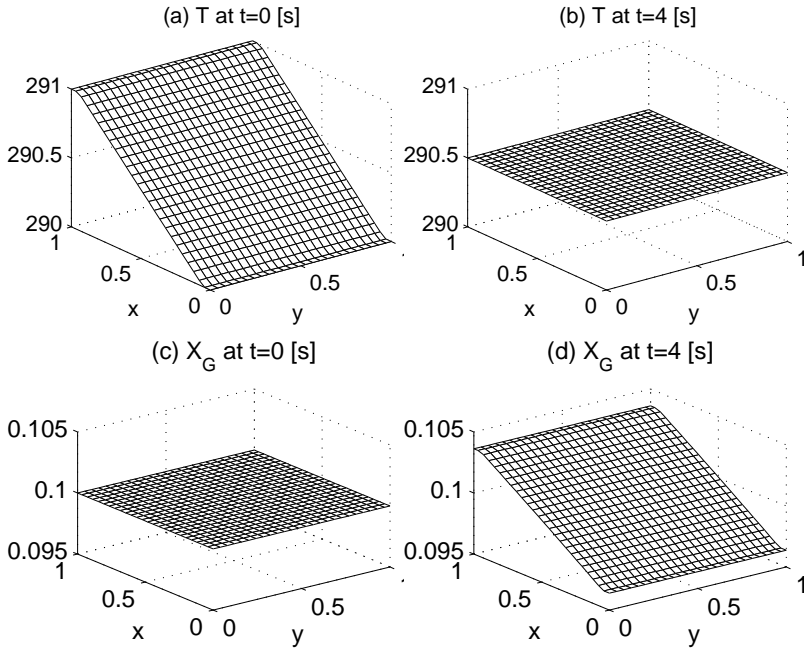
Figure 5.2: Case Study 1. (a) The temperature T at $t = 0$ [s], (b) T at $t = 0.2$ [s], (c) The gas mass fraction X_G at $t = 0.2$ [s], (d) T at $t = 4.0$ [s].

parameters are given in Table 5.2, with homogeneous boundary conditions everywhere on the boundary. With these conditions the density plots are given in Figure 5.1(a) to (c). System dynamics of this example has a similar interpretation, as given in Section 3.3.3. A comparison of the cross-section of density plots (denoted by ρ^{2D}) is made with the solution obtained from the $1D$ model (represented by ρ^{1D}). We use Equation (2.5) for computing the relative difference $\Delta\rho$. These results are given in Figure 5.1(d) to (f). The relative difference is negligible. The temperature and gas mass fraction plots are shown in Figure 5.2(a)-(c) and in Figure 5.2(d)-(f), respectively. The temperature and gas mass fraction plots are also compared with the plots obtained from the $1D$ model (not shown here), the relative difference found is again negligible.

In order to test the solution algorithm for rotation consistency, we repeat the above experiment with similar conditions in the y-direction, that is

$$T(\boldsymbol{x}, 0) = \begin{cases} 290, & \text{for } y \in [0, 0.05], \ x \in [0, 1], \\ 290 + \frac{10}{9}y - \frac{1}{18}, & \text{for } y \in]0.05, 0.95], \ x \in [0, 1], \\ 291, & \text{for } y \in]0.95, 1], \ x \in [0, 1]. \end{cases}$$

Further, we compared the solution results with the case when conditions are in x-direction. The relative difference is negligible again (not shown), as expected.

Table 5.3: Case Study 2

N_x	N_y	Δt	ϵ_r	$K\ [m^2]$	$\mu\ [Pa.s]$
100	100	1/10	10^{-6}	10^{-11}	5×10^{-5}

$T(\boldsymbol{x}, 0) = 290 + I_P$

$$I_P = \begin{cases} -\frac{20}{9}x + \frac{10}{9}, & \text{for } x \in [0.05, 0.5],\ y \in [0.5, 1-x] \cup [x, 0.5], \\ \frac{20}{9}x - \frac{10}{9}, & \text{for } x \in [0.5, 0.95],\ y \in [1-x, 0.5] \cup [0.5, x], \\ -\frac{20}{9}y + \frac{10}{9}, & \text{for } y \in [0.05, 0.5],\ x \in [0.5, 1-y] \cup [y, 0.5], \\ \frac{20}{9}y - \frac{10}{9}, & \text{for } y \in [0.5, 0.95],\ x \in [1-y, 0.5] \cup [0.5, y], \\ 1, & \text{for other } (x, y) \in \Omega, \end{cases}$$

$X_G(x, 0) = 0.1$
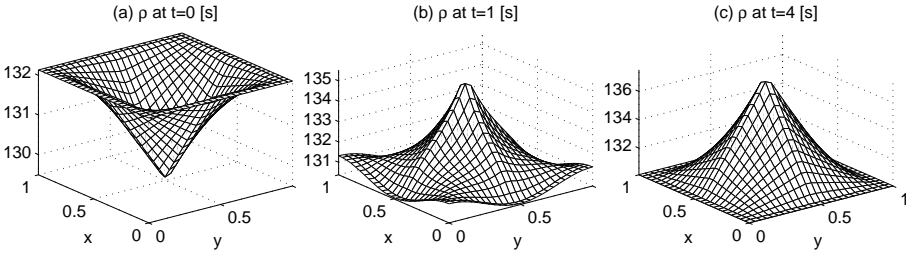
Figure 5.3: Case study 2. Solution plots for $2D$ model with $2D$ conditions. $\Delta t = 1/20$, $\Delta x = 1/99$, $\Delta y = 1/99$, $\epsilon_r = 10^{-6}$. The plots are (a) ρ at $t = 0$ [s], (b) ρ at $t = 1$ [s], and (c) ρ at $t = 4$ [s].

5.3.2   Case Study 2. The solution of $2D$ model with $2D$ conditions

In this case study, we test the working of the solution algorithm with $2D$ flow conditions given in Table 5.3, together with the homogeneous boundary conditions. Here, I_p is a stretched inverted pyramid function with unit height. The boundary is located at a height $z = 1$ and center point at $(x = 0.5,\ y = 0.5,\ z = 0)$. The pyramid fits within the domain $x \in [0.05, 0.95]$, $y \in [0.05, 0.95]$. The remaining 0.05 wide strip is a constant height function $z = 1$. This ensures an initially zero velocity normal to the boundary. A similar example is discussed in Section 4.2.2, where the system dynamics are also explained. Our algorithm works fine for the $2D$ flow systems. Plots for the solution variables are given in Figures 5.3 to 5.8

5.3.3   Case Study 3. Tracking of a sharp phase interface

In this case study, we show that the position of the phase-front follows a square-root law for a certain time period, which is an indication of mass diffusion. For our purpose, we set initial value of X_G equal to a step function and T is set piecewise linear so that
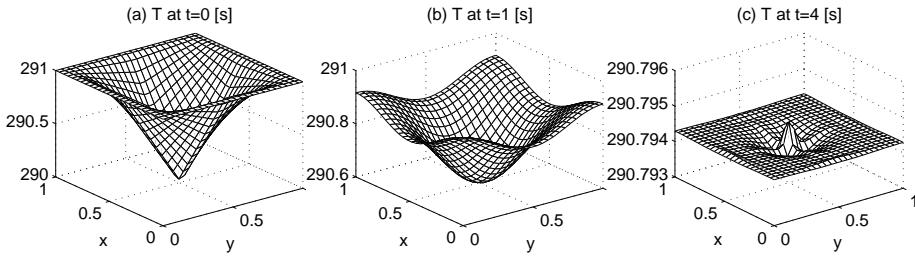
Figure 5.4: Case Study 2. The plots for T at $t = 0, \ 1, \ 4 \ [s]$.
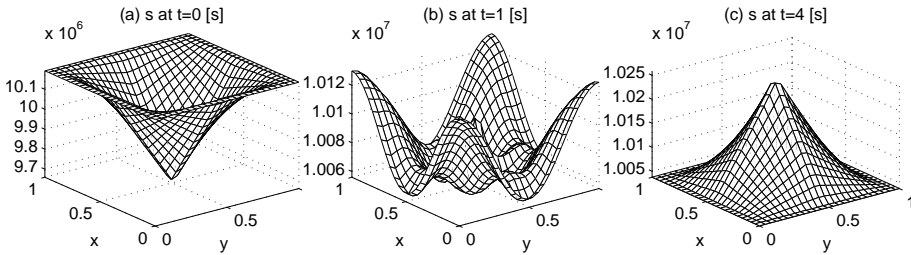
Figure 5.5: Case Study 2. The plots for s at $t = 0, \ 1, \ 4 \ [s]$.
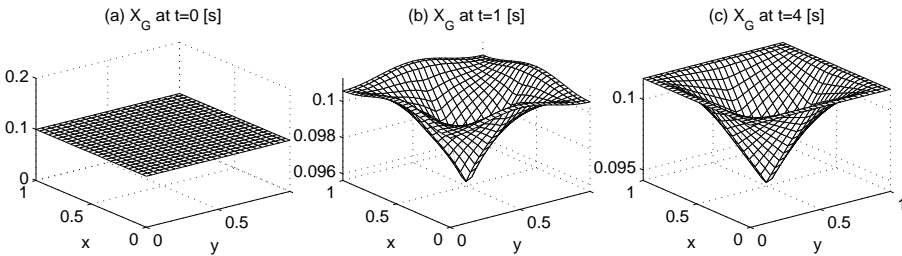
Figure 5.6: Case Study 2. The plots for X_G at $t = 0, \ 1, \ 4 \ [s]$.
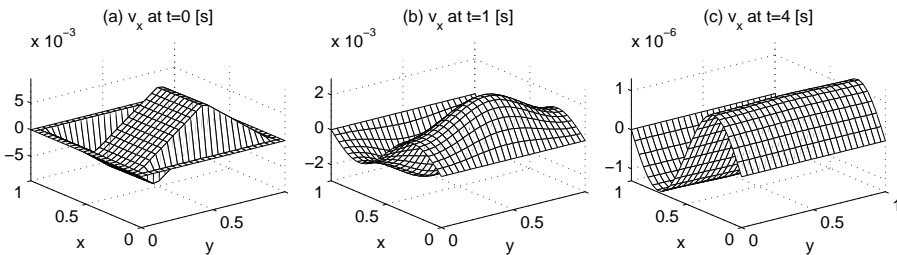
Figure 5.7: Case Study 2. The plots for v_x at $t = 0, \ 1, \ 4 \ [s]$.
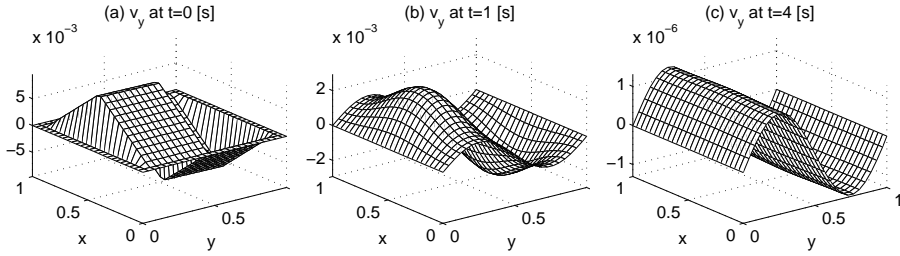
Figure 5.8: Case Study 2. The plots for v_y at $t = 0, \ 1, \ 4 \ [s]$.

we obtain a nonzero velocity for the phase interface. Let $\Gamma(t)$ be a function which represents the position of the phase front at time t i.e.,

$$\Gamma(t) := \left\{ x \in \Omega | X_G(x, t) = \hat{X}_G \right\}, \quad \text{for } t \geq 0.$$

We use the initial setting, as given in Table 5.4, where t_p is the process time. For

Table 5.4: Case Study 3

N_x	Δt	$\hat{X}_G$	$K \ [m^2]$	$\mu \ [Pa.s]$
1000	1/50	0.15	5×10^{-11}	5×10^{-5}

$$T(x, 0) = \begin{cases} 285, & \text{for } x \in [0, 0.05], \\ 285 + \frac{200}{9}x - \frac{20}{18}, & \text{for } x \in]0.05, 0.95], \\ 305, & \text{for } x \in]0.95, 1]. \end{cases}$$

$$X_G(x, 0) = \begin{cases} 0.1, & \text{for } x \in [0, 0.5], \\ 0.2, & \text{for } x \in]0.5, 1], \end{cases}$$

a discontinuous initial X_G, the problem cannot be solved in one time-step but $\Delta t = 1/50 \ [s]$ is still a large number as compared to the value of Δt used for Picard iteration and the IMEX method. After a few time iterations (e.g., 3), the X_G profile becomes smooth and Δt can be adapted to a larger value. In Figure 5.9, we provide, (a) the initial value for T, (b) the initial and steady-state values for X_G, and (c) a comparison between $\Gamma(t)$ and $g(t) = \alpha + \beta \sqrt{t}$ for empirically chosen $\alpha = 0.5515$ and $\beta = -0.37$. The phase tracking as part of the solution in moving boundary problems, such as Stefan problem, gives a function of the form $g(t) = \alpha + \beta \sqrt{t}$. Since we consider an isolated system, with no heat source in it, it attains a steady-state asymptotically. This means that there is a $\Gamma^\infty \in (0, 1)$ such that $\Gamma(t) \to \Gamma^\infty$ as $t \to \infty$. Hence, we do not expect $\Gamma(t)$ to follow $g(t)$ for a longer time interval. The function $\Gamma(t)$ however approximately matches with $g(t)$ at early stages only. Although, near $t = 0$ (at the very early stage), there seems to be a different behavior. This deviation is acceptable at the first iteration because some of the variables are discontinuous at $t = 0$. As a result of the discontinuity, even the first weak derivative of ρ with respect to x, for instance,
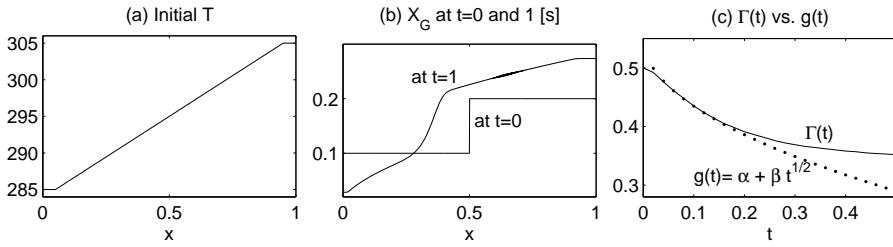
Figure 5.9: Case Study 3. Solution plots for (a) the initial T, (b) the initial and steady-state X_G, and (c) a comparison between $\Gamma(t)$ and $g(t) = \alpha - \beta \sqrt{t}$ with $\alpha = 0.5515$ and $\beta = 0.37$.

does not exist. Therefore, the approximation made from the Taylor series in Section 5.1.3, which was used to derive the Newton method, cannot give an accurate solution at $t = 0$. This fact is shown in Figure 5.9(c). We conclude that the ρ-h model can be used to solve sharp interface problems with diffusion-like mechanisms.

5.3.4   Case Study 4. Quarter-circle phase front

In this $2D$ example, we show that the displacement of the phase-front, for a given time interval, depends on its distance from the boundary. We set the following initial conditions.

$$X_G(\boldsymbol{x}, 0) = \begin{cases} 0.1 & \text{for } x^2 + y^2 \leq 0.5, \; x, y \geq 0, \\ 0.2 & \text{for } x^2 + y^2 > 0.5, \; 0 \leq x, y \leq 1, \end{cases}$$

$$T(\boldsymbol{x}, 0) = \frac{1}{2}(T_1 + T_2),$$

$$T_1 = \begin{cases} 305 & \text{for } x \in [0, 0.05], \; y \in [0, 1], \\ 305 - \frac{200}{9}x + \frac{20}{18} & \text{for } x \in]0.05, 0.95], \; y \in [0, 1], \\ 285 & \text{for } x \in]0.95, 1], \; y \in [0, 1], \end{cases}$$

$$T_2 = \begin{cases} 305 & \text{for } y \in [0, 0.05], \; x \in [0, 1], \\ 305 - \frac{200}{9}y + \frac{20}{18} & \text{for } y \in]0.05, 0.95], \; x \in [0, 1], \\ 285 & \text{for } y \in]0.95, 1], \; x \in [0, 1]. \end{cases}$$

Other parameters are given in Table 5.5. By setting T in this way, we ensure a $2D$

Table 5.5: Case Study 4

N_x	N_y	Δt	$\hat{X}_G$	t_p [s]
200	200	1/50	0.15	1

initial flow in general but a zero normal velocity at every boundary point. Figure

5.10 shows the initial values of T and X_G whereas the contour plot in Figure 5.11 contains the initial and steady-state position of the phase front. It can be seen that the displacement of the edge is most pronounced along the line $y = x$. This is a consequence of the fact that the distance to the boundaries is maximal at $y = x$, by which the fluids can be transported more rapidly by the nonlinear (cross) diffusion mechanism. In this example we show that the model works well for $2D$ conditions for the tracking of sharp interfaces.
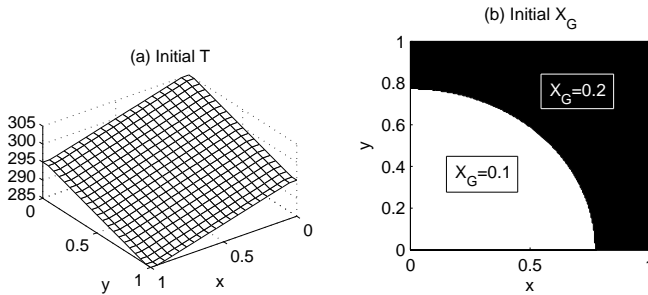
Figure 5.10: Case Study 4. Initial values of T and X_G.
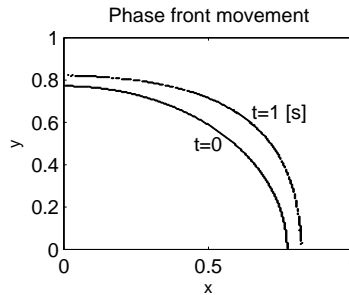
Figure 5.11: Case Study 4. The initial and steady-state values of the phase front.

5.3.5   The solution on a quadrilateral grid

In this section, we solve the $2D$ system on a quadrilateral grid, as shown in Figure 5.12(a). In the grid generation algorithm, we ensure convex elements. That is, no element contains an internal angle greater than 180°. In our case, the maximum possible interior angle (θ) is 157.38^o. For our test problem, the initial condition for X_G is given by
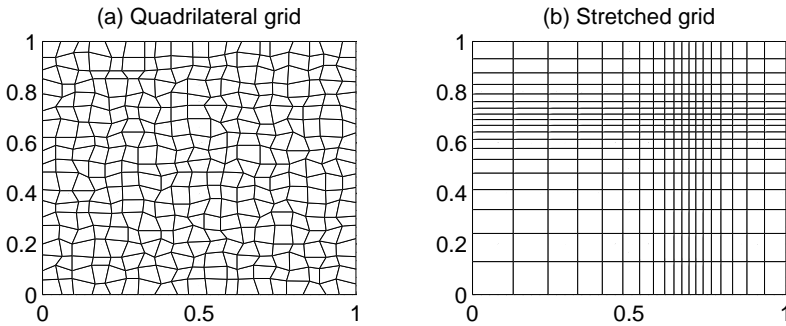
Figure 5.12: Quadrilateral and stretched grids.

Table 5.6: Example: Quadrilateral grid

r_1	r_2	r	G_1	G_2	m
0.63	0.7	$\sqrt{x^2 + y^2}$	0.1	0.2	$\frac{G_1 - G_2}{r_2 - r_1}$

$$X_G(x, 0) = \begin{cases} G_1, & \{(x,y)|r < r_1\}, \\ mr - mr_1 + G_1, & \{(x,y)|r_1 \leq r \leq r_2\}, \\ G_2 & \{(x,y)|r < r_1\}, \end{cases} \quad (5.23)$$

where the parameters, G_i, r_i, and m are given in Table 5.6. The initial conditions for the temperature are given in Figure 5.13(a). Note that $X_G(\boldsymbol{x}, 0)$ has a piecewise linear profile along a semicircular path. In this way the profile is close to a step function but gradients of all variables are finite, elementwise. At $t = 2$, the system approximately attains its steady-state. The steady-state values of T and X_G are provided in Figures 5.13(b) and (d), respectively. While the T profile is smooth in this case, the X_G profile has wiggles in the region where the system variables (e.g., ρ, h) exhibit high gradient values. The cause behind these wiggles is to be investigated in the future work. At this moment, we believe that this is due to the truncation error. In our experiments, it is found that, the magnitude of these wiggles reduces by decreasing θ or decreasing gradient values in $X_G(\boldsymbol{x}, 0)$, e.g., by taking higher $r_2 - r_1$. In Table 5.7, we show that the infinity norm of ΔX_G is affected (and unaffected) by a number of parameters over this kind of grid. The use of the $SUPG$ method is expected to reduce these wiggles. We do not see any improvement when Δt is reduced from $1/10$ to $1/100$ seconds. We compare the steady state variables obtained with this grid ($T^{(1)}$, $X_G^{(1)}$) by the ones that we obtain on a regular grid and by mapping onto the irregular grid, ($T^{(2)}$, $X_G^{(2)}$). The definition of relative differences ΔT and ΔX_G, is analogous to Equation (2.5). These relative differences are plotted in Figures 5.13(e) and (f). We have a small ΔT ($< 0.02\%$) but a large ΔX_G. We conclude that the solution algorithm, when applied on quadrilateral grids, works well for smooth system variables but we get large relative differences (with respect to the regular grid) where the gradients are large.
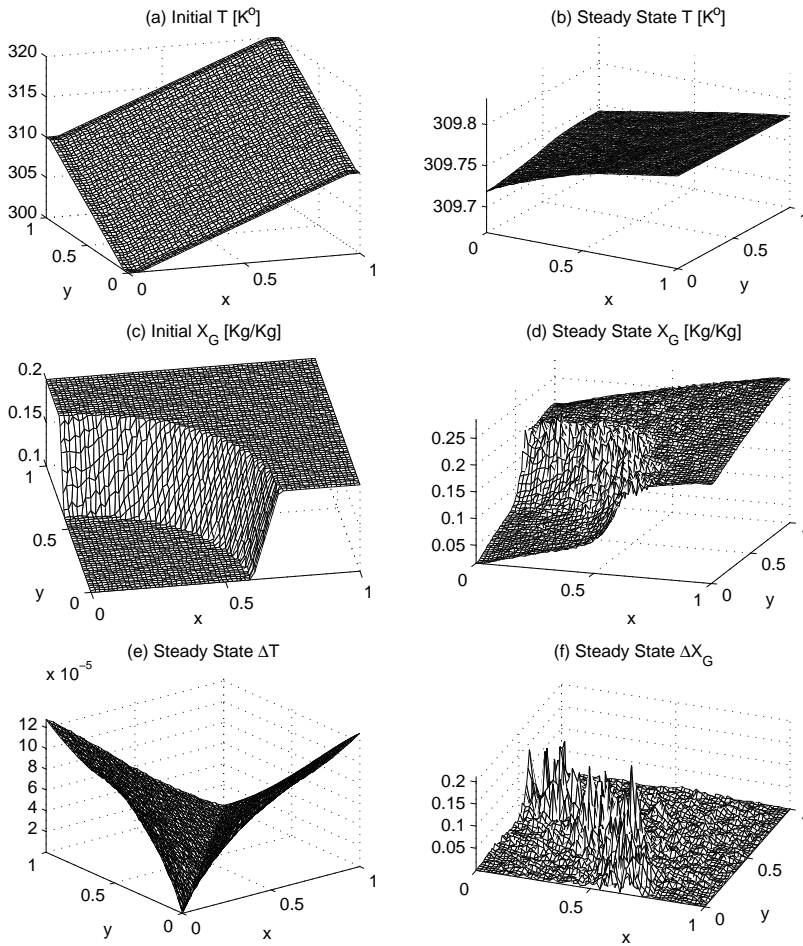
Figure 5.13: Quadrilateral grid example. Plots of (a) $T(\boldsymbol{x}, 0)$, (b) steady-state T (t=2), (c) $X_G(\boldsymbol{x}, 0)$, (d) steady-state X_G (t=2 [s]), (e) steady-state ΔT, and (f) steady-state ΔX_G.

Table 5.7: ΔX_G dependence on various factors

$r_2 - r_1$	θ	N_x	N_y	Δt	$\|\Delta X_G\|_\infty$
0.1	100	100	157.38	1/20	0.19143
0.2	100	100	157.38	1/20	0.14191
0.1	40	40	118.08	1/20	0.13724
0.1	60	60	118.08	1/20	0.11557
0.1	80	80	118.08	1/20	0.13412
0.1	100	100	118.08	1/20	0.09975
0.1	100	100	102.68	1/20	0.06559
0.1	100	100	118.08	1/20	0.09975
0.1	100	100	118.08	1/20	0.13412
0.1	100	100	136.40	1/20	0.15952
0.1	100	100	157.38	1/20	0.19143

5.3.6   The solution on a stretched grid

In this section, we solve the example given in the previous section, on a stretched grid (see Figure 5.14). Again, the purpose here is to test the solution algorithm on this kind of grid. The grid is constructed by applying the following scheme.

Let x be a vector of uniformly spaced number, with spacing Δx. It can be transformed to another vector $\tilde{x}$ such that the difference between its consecutive numbers follows a defined function. We use the following transformation

$$\tilde{x}_j = a\left[c(x_j - x_0)^3 + (x_j - x_0)\right] + b, \quad \forall x_j \in x,$$

where

$$a = \left[cx_0^3 + x_0 + c(1 - x_0)^3 + (1 - x_0)\right]^{-1},$$
$$b = (cx_0^3 - x_0)\left[cx_0^3 + x_0 + c(1 - x_0)^3 + (1 - x_0)\right]^{-1}.$$

The parameters x_0 and c are used to vary position of the higher resolution region and the degree of stretching, respectively. We apply this transformation to both dimensions of the 2D grid. The purpose of using this grid is to verify that our solution algorithm works for this kind of grid as well.

We use the initial and parametric values from the previous example, which are given by Equation (5.23) and Figure 5.13. Therefore, the solution set is approximately the same as obtained for the previous example. The relative differences of the steady state T and X_G values on the stretched grid with the solutions on the regular grid are provided in Figure 5.14. We have small steady-state relative differences, ΔT and ΔX_G, which can be reduced further by increasing grid size and other factors discussed in the previous example.
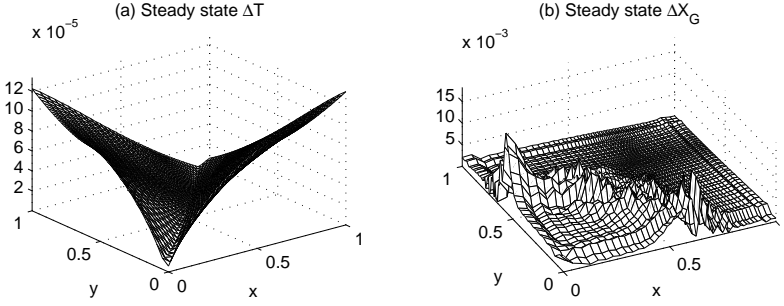
Figure 5.14: Stretched grid example. Plots of (a) steady-state ΔT and (b) steady-state ΔX_G.

5.4   Darcy's law with the gravity term

In this test example, we include the gravity term in the y-component of Darcy's law [36]. This gives

$$v_y = -\frac{K}{\mu}\left(\frac{\partial P}{\partial y} + \rho g\right), \quad \boldsymbol{x} \in \Gamma,\ t > 0, \tag{5.24}$$

where $g \approx 9.81\ [m/s^2]$ is the gravitational constant. Following the procedure of Section 5.2, (i.e., treating the above equation by the standard Galerkin algorithm) then, the equivalent matrix equation is given by

$$S^{(40)}\delta\boldsymbol{\rho} + S^{(41)}\delta\boldsymbol{v}_y + S^{(42)}\delta\boldsymbol{P} + \boldsymbol{f}^{(v)} = \boldsymbol{0}, \tag{5.25}$$

where the global matrix $S^{(40)}$ and the vector $\boldsymbol{f}^{(v)}$ are defined as

$$S^{(40)}_{ij} = -\frac{K}{\mu}g\int_\Omega \phi_i\phi_j d\Omega, \tag{5.26}$$

$$f^{(v)}_i = \frac{K}{\mu}\int_\Omega \frac{\partial P^k}{\partial y}\phi_i d\Omega + \int_\Omega v^k_y\phi_i d\Omega - \frac{K}{\mu}g\int_\Omega \rho^k\phi_i d\Omega. \tag{5.27}$$

With the parameters and the initial conditions used in the previous examples, the gravity term (ρg) is very small compared to the pressure gradient term ($\boldsymbol{\nabla}P$). In our test example, we use the following initial conditions

$$X_G(\boldsymbol{x}, 0) = 0.1,$$
$$T(\boldsymbol{x}, 0) = 300.$$

Since $\Delta t = 0$, this makes $\Delta P = 0$ (see Section 4.1.1). Therefore, the velocity is initiated by the gravity term. The plots of the solution variables are given in Figure 5.15. Note that Figure 5.15(a) depicts graphs of T for the entire spatial domain at $t = 0$
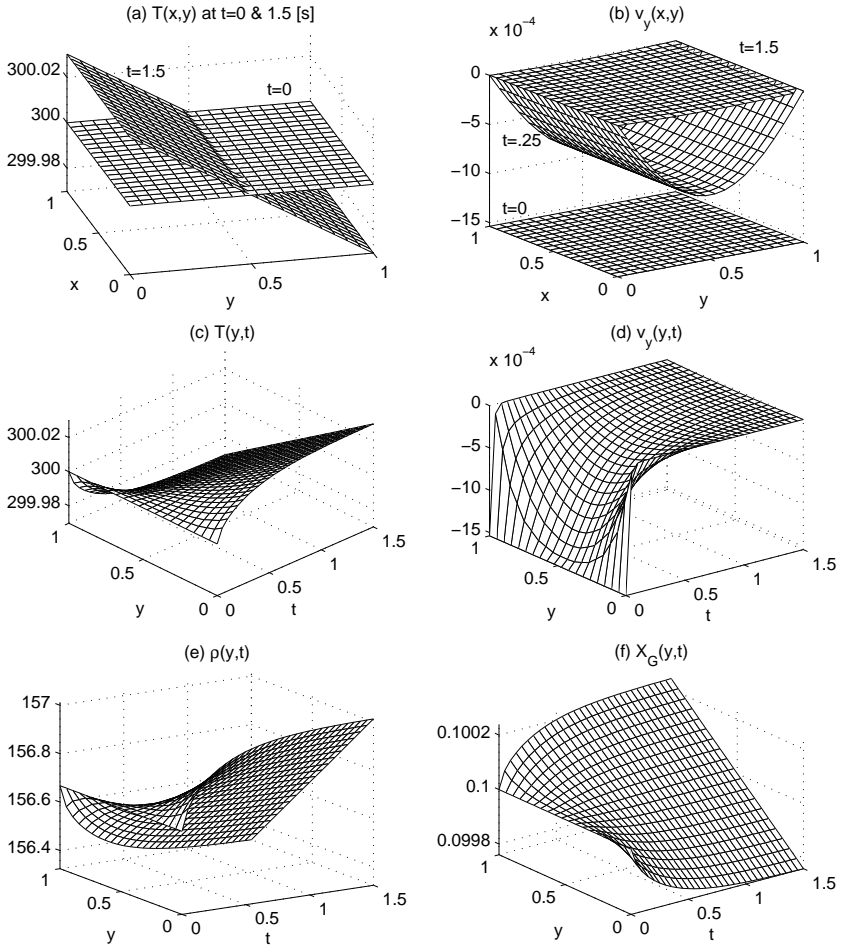
Figure 5.15: Flow due to gravity term. Plots of system variables.

and 1.0 [s]. These plots indicate that the flow is only in the y-direction. The plots for v_y (at $t = 0$, 0.25, and 1.5 [s]) are given in Figure 5.15(b). From Figure 5.15(c) to (f), the cross-sections of the solution variables (along y-axis) are plotted for the entire process time. We do not have any flow in the x-direction. Hence, $v_x(\boldsymbol{x}, t) = 0$, $\boldsymbol{x} \in \Omega$, $t > 0$. The velocity along y-axis starts with $v_y(\boldsymbol{x}, 0) = -g\rho$ but $\boldsymbol{v} \cdot \hat{\boldsymbol{n}}$ immediately goes to zero because the system is isolated. This is shown in Figure 5.15(b) and (d). A flow in the y-direction causes an increase in the density, near $y = 0$ boundary (Figure 5.15(e)) and an increase in the gas mass fraction near $y = 1$ boundary (Figure 5.15(f)). For the temperature evolution (Figure 5.15(c)), the Gibbs phase rule dictates that an increase in the density at a point should accompany an increase in temperature at that point. The Gibbs phase rule and its implications are discussed in Chapters 6 and 7. Since $P = P(T)$ (Figure 4.1), an increase in $\frac{\partial T}{\partial y}$ increase $\frac{K}{\mu} \frac{\partial P}{\partial y}$. After a certain period of time, $-\frac{K}{\mu} \frac{\partial T}{\partial y}$ cancels out the term, $-g\rho$, in the Darcy's law and hence results in a zero v_y. This is also a steady-state of the system. We conclude that the model and the solution algorithm works fine when the gravity term is added to Darcy's law.

5.5   Conclusions

We developed a successful strategy to solve the PDE's in the (ρ, h)-formulation of multi-phase flow. The Newton-Raphson linearization combined with the standard Galerkin algorithm allows to choose a large Δt with respect to stability and to solve the system efficiently. In the context of phase front tracking, this model shows a behavior that is similar to the solution of Stefan problems (e.g., moving boundary). We also see that the evolution of the density and enthalpy is diffusion-controlled. The solution algorithm is found to be consistent upon comparing the solution results of $1D$ and $2D$ models. The algorithm also works well for regular, quadrilateral and stretched grids at least for smooth conditions.

Chapter 6

Stability analysis of the density-enthalpy model

In this chapter, the convergence behavior of ρ-h model is investigated. We transform the original model to a system with only two equations. Subsequently, this two equation-model is linearized to perform a linear stability analysis. The eigenvalues of the linear model are used to investigate stability and convergence to steady-state solution. It is shown that the model is consistent with the Gibbs phase rule. Since linear stability is investigated, we limit ourselves to a $1D$ flow system.

6.1 An alternate set of state variables

In the previous chapters, we used the pair (ρ, h) as our state variables. However, we will use ρ and s as our state variables in this chapter, where s represents the total enthalpy with units $[J/m^3]$. This is because, they allow a more straightforward transformation. In Figure 6.1, three (ρ, s) phase-diagrams are shown for P, T, and X_G. We
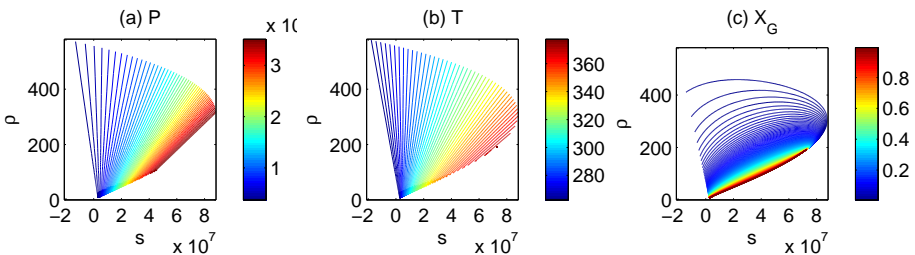
Figure 6.1: Partially negative total-enthalpy values corresponding to (a) pressure, (b) temperature, and (c) gas mass-fraction.

observe that these values are valid for a certain range of temperature values. To make this point clear, s is plotted as a function of T at constant X_G in Figure 6.2. From this graph (and other experiments), we conclude that currently available (ρ, s) or equivalently (ρ, h) diagrams are valid approximately for $275 \leq T \leq 360$. Outside this range, we encounter negative enthalpy and $\frac{\partial s}{\partial T} < 0$
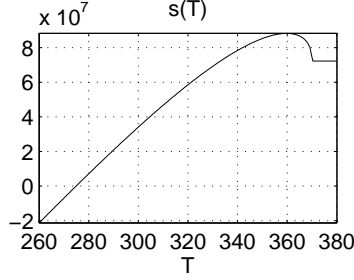
Figure 6.2: A plot of total enthalpy s as a function of T at constant X_G.

6.2   Transformation to two equations system

The $1D$ model is given in Chapter 3, Section 3.1. Consider the mass equation (Equation (3.1))

$$\frac{\partial \rho}{\partial t} + \frac{\partial (\rho v)}{\partial x} = 0, \qquad\qquad x \in \Omega, \ t > 0, \qquad\qquad (6.1)$$

Substitute v by its value as given by the Darcy's law (Equation (3.3)), we obtain

$$\frac{\partial \rho}{\partial t} + \frac{\partial}{\partial x}\left(-\frac{K}{\mu}\rho \frac{\partial P}{\partial x}\right) = 0. \qquad\qquad (6.2)$$

Using the chain rule for $\frac{\partial P}{\partial x}$,

$$\frac{\partial P}{\partial x} = \frac{\partial P}{\partial \rho}\frac{\partial \rho}{\partial x} + \frac{\partial P}{\partial s}\frac{\partial s}{\partial x},$$

in Equation (6.2), gives

$$\frac{\partial \rho}{\partial t} - \frac{K}{\mu}\frac{\partial}{\partial x}\left[\rho\left(\frac{\partial P}{\partial \rho}\frac{\partial \rho}{\partial x} + \frac{\partial P}{\partial s}\frac{\partial s}{\partial x}\right)\right] = 0. \qquad\qquad (6.3)$$

By making similar substitutions of v, $\frac{\partial P}{\partial x}$, and $\frac{\partial T}{\partial x}$, the energy equation takes the form

$$\frac{\partial s}{\partial t} - \frac{K}{\mu}\frac{\partial}{\partial x}\left[s\left(\frac{\partial P}{\partial \rho}\frac{\partial \rho}{\partial x} + \frac{\partial P}{\partial s}\frac{\partial s}{\partial x}\right)\right] - D\frac{\partial}{\partial x}\left[\frac{\partial T}{\partial \rho}\frac{\partial \rho}{\partial x} + \frac{\partial T}{\partial s}\frac{\partial s}{\partial x}\right] = 0. \qquad (6.4)$$

Hence the "many-equations" system given by Equations (3.1) to (3.5) is written in the following "two-equations" format

$$\frac{\partial \rho}{\partial t} = \frac{\partial}{\partial x}\left(D_{11}\frac{\partial \rho}{\partial x} + D_{12}\frac{\partial s}{\partial x}\right), \tag{6.5}$$

$$\frac{\partial s}{\partial t} = \frac{\partial}{\partial x}\left(D_{21}\frac{\partial \rho}{\partial x} + D_{22}\frac{\partial s}{\partial x}\right), \tag{6.6}$$

where D_{ij} are given by

$$D_{11} = \frac{K}{\mu}\rho\frac{\partial P}{\partial \rho}, \qquad\qquad D_{12} = \frac{K}{\mu}\rho\frac{\partial P}{\partial s},$$

$$D_{21} = \frac{K}{\mu}s\frac{\partial P}{\partial \rho} + D\frac{\partial T}{\partial \rho}, \qquad\qquad D_{22} = \frac{K}{\mu}s\frac{\partial P}{\partial s} + D\frac{\partial T}{\partial s}.$$

The natural boundary conditions are derived from Equations (3.8) and (3.9), with $k_m = k_h = 0$, which gives

$$\frac{K}{\mu}\rho\left(\frac{\partial P}{\partial \rho}\frac{\partial \rho}{\partial x} + \frac{\partial P}{\partial s}\frac{\partial s}{\partial x}\right) = 0, \tag{6.7}$$

$$\frac{K}{\mu}s\left(\frac{\partial P}{\partial \rho}\frac{\partial \rho}{\partial x} + \frac{\partial P}{\partial s}\frac{\partial s}{\partial x}\right) - D\left(\frac{\partial T}{\partial \rho}\frac{\partial \rho}{\partial x} + \frac{\partial T}{\partial s}\frac{\partial s}{\partial x}\right) = 0. \tag{6.8}$$

6.3 Numerical solution algorithm for two-equations model

To verify that the two approaches (many-equations versus two-equations models) are indeed equivalent, we solve the system given by equations (6.5) and (6.6) by the standard Galerkin algorithm. In this section, we will present this method applied to the "two-equation" model.

6.3.1 Discretization of the first equation

We start the solution algorithm by considering the transformed mass equation (i.e., equation (6.3)) and write down its weak form

$$\int_{\Omega}\frac{\partial \rho}{\partial t}\phi d\Omega - \frac{K}{\mu}\int_{\Omega}\frac{\partial}{\partial x}\left[\rho\left(\frac{\partial P}{\partial \rho}\frac{\partial \rho}{\partial x} + \frac{\partial P}{\partial s}\frac{\partial s}{\partial x}\right)\right]\phi d\Omega = 0.$$

Apply integration by parts to the second integral in the above equation, we have

$$\int_{\Omega}\frac{\partial \rho}{\partial t}\phi d\Omega - \left[\frac{K}{\mu}\rho\left(\frac{\partial P}{\partial \rho}\frac{\partial \rho}{\partial x} + \frac{\partial P}{\partial s}\frac{\partial s}{\partial x}\right)\phi\right]_0^1 + \frac{K}{\mu}\int_{\Omega}\rho\left(\frac{\partial P}{\partial \rho}\frac{\partial \rho}{\partial x} + \frac{\partial P}{\partial s}\frac{\partial s}{\partial x}\right)\frac{d\phi}{dx}d\Omega = 0.$$

The boundary term vanishes (see Equation (6.7)). By using the Euler backward time integration, the above equation is written as

$$\frac{1}{\Delta t}\int_{\Omega}(\rho^{\tau} - \rho^{\tau-1})\phi dx + \frac{K}{\mu}\int_{\Omega}\rho^{\tau}\frac{\partial P^{\tau}}{\partial \rho}\frac{\partial \rho^{\tau}}{\partial x}\frac{d\phi}{dx}dx + \frac{K}{\mu}\int_{\Omega}\rho^{\tau}\frac{\partial P^{\tau}}{\partial s}\frac{\partial s^{\tau}}{\partial x}\frac{d\phi}{dx}dx = 0.$$

For ease of notation, we use the following convention for $\frac{\partial P}{\partial \rho}$, $\frac{\partial P}{\partial s}$, $\frac{\partial T}{\partial \rho}$, and $\frac{\partial T}{\partial s}$

$$\frac{\partial P^\tau}{\partial \rho} \text{ for } \frac{\partial P}{\partial \rho}(\rho^\tau, s^\tau),$$

$$\frac{\partial P^k}{\partial \rho} \text{ for } \frac{\partial P}{\partial \rho}(\rho^{\tau,k}, s^{\tau,k}),$$

$$\frac{\partial P_i^k}{\partial \rho} \text{ for } \frac{\partial P}{\partial \rho}(\rho_i^{\tau,k}, s_i^{\tau,k}).$$

The convention used for $\frac{\partial P}{\partial s}$, $\frac{\partial T}{\partial \rho}$, and $\frac{\partial T}{\partial s}$ is analogous. The linearization about ρ^k and s^k is given by the following equation where we omit the index τ for brevity, except for explicit terms and use the notation $\delta\rho = \rho^{k+1} - \rho^k$ and $\delta s = s^{k+1} - s^k$.

$$\frac{1}{\Delta t} \int_\Omega (\rho^k - \rho^{\tau-1} + \delta\rho)\phi dx$$

$$+ \frac{K}{\mu} \int_\Omega \left[\rho^k \frac{\partial P^k}{\partial \rho} \frac{\partial \rho^k}{\partial x} + \delta\rho \frac{\partial P^k}{\partial \rho} \frac{\partial \rho^k}{\partial x} + \rho^k \left(\frac{\partial P^{k+1}}{\partial \rho} - \frac{\partial P^k}{\partial \rho} \right) \frac{\partial \rho^k}{\partial x} + \rho^k \frac{\partial P^k}{\partial \rho} \frac{\partial(\delta\rho)}{\partial x} \right] \frac{d\phi}{dx} dx$$

$$+ \frac{K}{\mu} \int_\Omega \left[\rho^k \frac{\partial P^k}{\partial s} \frac{\partial s^k}{\partial x} + \delta\rho \frac{\partial P^k}{\partial s} \frac{\partial s^k}{\partial x} + \rho^k \left(\frac{\partial P^{k+1}}{\partial s} - \frac{\partial P^k}{\partial s} \right) \frac{\partial s^k}{\partial x} + \rho^k \frac{\partial P^k}{\partial s} \frac{\partial(\delta s)}{\partial x} \right] \frac{d\phi}{dx} dx$$

$$= 0. \tag{6.9}$$

We use the central difference approximation for the density and enthalpy derivatives, given by the following expressions

$$\frac{\partial P_i^k}{\partial \rho} = \frac{\partial P}{\partial \rho}(\rho_i^k, s_i^k) = \frac{1}{2\epsilon_\rho}[P(\rho_i^k + \epsilon_\rho, s_i^k) - P(\rho_i^k - \epsilon_\rho, s_i^k)],$$

$$\frac{\partial^2 P_i^k}{\partial \rho^2} = \frac{1}{\epsilon_\rho^2}[P(\rho_i^k + \epsilon_\rho, s_i^k) - 2P(\rho_i^k, s_i^k) + P(\rho_i^k - \epsilon_\rho, s_i^k)],$$

$$\frac{\partial^2 P_i^k}{\partial \rho \partial s} = \frac{1}{4\epsilon_\rho\epsilon_s}[P(\rho_i^k + \epsilon_\rho, s_i^k + \epsilon_s) - P(\rho_i^k + \epsilon_\rho, s_i^k - \epsilon_s)$$

$$- P(\rho_i^k - \epsilon_\rho, s_i^k + \epsilon_s) + P(\rho_i^k - \epsilon_\rho, s_i^k - \epsilon_s)],$$

with respective errors of $\Theta(\epsilon_\rho^2)$, $\Theta(\epsilon_h^2)$, and $\Theta(\epsilon_\rho\epsilon_h)$. Furthermore, ϵ_ρ and ϵ_s are suitable small numbers (in our case, $\epsilon_\rho = 0.1$ and $\epsilon_s = 100$). The approximations for $\frac{\partial P_i^k}{\partial s}$ and $\frac{\partial^2 P_i^k}{\partial s^2}$ are analogous. The approximation for $\frac{\partial P}{\partial \rho}$ from Taylor series expansion about (ρ^k, s^k) leads to

$$\frac{\partial P^{k+1}}{\partial \rho} - \frac{\partial P^k}{\partial \rho} = (\rho^{k+1} - \rho^k)\frac{\partial^2 P^k}{\partial \rho^2} + (s^{k+1} - s^k)\frac{\partial^2 P^k}{\partial \rho \partial s}.$$

The expression $\left(\frac{\partial T^{k+1}}{\partial s} - \frac{\partial T^k}{\partial s}\right)$ is defined in a similar way. Using these values in equation (6.9), yields

$$
\frac{1}{\Delta t} \int_\Omega (\rho^k - \rho^{\tau-1} + \delta\rho)\phi dx
$$

$$
+ \frac{K}{\mu} \int_\Omega \left[\rho^k \frac{\partial P^k}{\partial \rho} \frac{\partial \rho^k}{\partial x} + \frac{\partial P^k}{\partial \rho} \frac{\partial \rho^k}{\partial x}\delta\rho \right.
$$

$$
+ \rho^k \frac{\partial \rho^k}{\partial x}\left(\delta\rho \frac{\partial^2 P^k}{\partial \rho^2} + \delta s \frac{\partial^2 P^k}{\partial\rho\partial s}\right) + \rho^k \frac{\partial P^k}{\partial \rho}\frac{\partial(\delta\rho)}{\partial x}\left.\right] \frac{d\phi}{dx}dx
$$

$$
+ \frac{K}{\mu} \int_\Omega \left[\rho^k \frac{\partial P^k}{\partial s}\frac{\partial s^k}{\partial x} + \frac{\partial P^k}{\partial s}\frac{\partial s^k}{\partial x}\delta\rho \right.
$$

$$
+ \rho^k \frac{\partial s^k}{\partial x}\left(\delta\rho \frac{\partial^2 P^k}{\partial\rho\partial s} + \delta s \frac{\partial^2 P^k}{\partial s^2}\right) + \rho^k \frac{\partial P^k}{\partial s}\frac{\partial(\delta s)}{\partial x}\left.\right] \frac{d\phi}{dx}dx = 0.
$$

Next, we rearrange these terms into explicit and implicit parts

$$
\frac{1}{\Delta t}\int_\Omega \delta\rho\phi dx + \frac{K}{\mu}\int_\Omega \left(\frac{\partial P^k}{\partial \rho}\frac{\partial \rho^k}{\partial x}\delta\rho + \rho^k \frac{\partial \rho^k}{\partial x}\frac{\partial^2 P^k}{\partial \rho^2}\delta\rho + \rho^k \frac{\partial P^k}{\partial \rho}\frac{\partial(\delta\rho)}{\partial x}\right.
$$

$$
+ \frac{\partial P^k}{\partial s}\frac{\partial s^k}{\partial x}\delta\rho + \rho^k \frac{\partial s^k}{\partial x}\frac{\partial^2 P^k}{\partial\rho\partial s}\delta\rho \left.\right)\frac{d\phi}{dx}dx
$$

$$
+ \frac{K}{\mu}\int_\Omega \left(\rho^k \frac{\partial \rho^k}{\partial x}\frac{\partial^2 P^k}{\partial\rho\partial s}\delta s + \rho^k \frac{\partial s^k}{\partial x}\frac{\partial^2 P^k}{\partial s^2}\delta s + \rho^k \frac{\partial P^k}{\partial s}\frac{\partial(\delta s)}{\partial x}\right)\frac{d\phi}{dx}dx
$$

$$
+ \frac{1}{\Delta t}\int_\Omega (\rho^k - \rho^{\tau-1})\phi dx + \frac{K}{\mu}\int_\Omega \left(\rho^k \frac{\partial P^k}{\partial \rho}\frac{\partial \rho^k}{\partial x} + \rho^k \frac{\partial P^k}{\partial s}\frac{\partial s^k}{\partial x}\right)\frac{d\phi}{dx}dx = 0.
$$

We apply the standard Galerkin discretization by using the approximations, $\delta\rho \approx \sum_{j=1}^N \delta\rho_j\phi_j$, $\delta s \approx \sum_{j=1}^N \delta s_j\phi_j$ and by choosing $\phi = \phi_i$

$$
\frac{1}{\Delta t}\sum_{j=1}^N \delta\rho_j \int_\Omega \phi_i\phi_j dx + \frac{K}{\mu}\sum_{j=1}^N \delta\rho_j \int_\Omega \left(\frac{\partial P^k}{\partial \rho}\frac{\partial \rho^k}{\partial x}\phi_j + \rho^k \frac{\partial \rho^k}{\partial x}\frac{\partial^2 P^k}{\partial \rho^2}\phi_j + \rho^k \frac{\partial P^k}{\partial \rho}\frac{d\phi_j}{dx}\right.
$$

$$
+ \frac{\partial P^k}{\partial s}\frac{\partial s^k}{\partial x}\phi_j + \rho^k \frac{\partial s^k}{\partial x}\frac{\partial^2 P^k}{\partial\rho\partial s}\phi_j \left.\right)\frac{d\phi_i}{dx}dx
$$

$$
+ \frac{K}{\mu}\sum_{j=1}^N \delta s_j \int_\Omega \left(\rho^k \frac{\partial \rho^k}{\partial x}\frac{\partial^2 P^k}{\partial\rho\partial s}\phi_j + \rho^k \frac{\partial s^k}{\partial x}\frac{\partial^2 P^k}{\partial s^2}\phi_j + \rho^k \frac{\partial P^k}{\partial s}\frac{d\phi_j}{dx}\right)\frac{d\phi_i}{dx}dx
$$

$$
+ \frac{1}{\Delta t}\int_\Omega (\rho^k - \rho^{\tau-1})\phi_i dx + \frac{K}{\mu}\int_\Omega \left(\rho^k \frac{\partial P^k}{\partial \rho}\frac{\partial \rho^k}{\partial x} + \rho^k \frac{\partial P^k}{\partial s}\frac{\partial s^k}{\partial x}\right)\frac{d\phi_i}{dx}dx = 0.
$$

An equivalent matrix form of the above equation is given by

$$
S^{(11)}\,\delta\rho + S^{(12)}\,\delta s + f^{(1)} = \mathbf{0}. \tag{6.10}
$$

The stiffness matrices and the vector $\boldsymbol{f}^{(1)}$ are defined as

$$S_{ij}^{(11)} = \frac{1}{\Delta t} \int_{\Omega} \phi_i \phi_j dx + \frac{K}{\mu} \int_{\Omega} \left(\frac{\partial P^k}{\partial \rho} \frac{\partial \rho^k}{\partial x} \phi_j + \rho^k \frac{\partial \rho^k}{\partial x} \frac{\partial^2 P^k}{\partial \rho^2} \phi_j + \rho^k \frac{\partial P^k}{\partial \rho} \frac{d\phi_j}{dx} \right.$$
$$\left. + \frac{\partial P^k}{\partial s} \frac{\partial s^k}{\partial x} \phi_j + \rho^k \frac{\partial s^k}{\partial x} \frac{\partial^2 P^k}{\partial \rho \partial s} \phi_j \right) \frac{d\phi_i}{dx} dx,$$

$$S_{ij}^{(12)} = \frac{K}{\mu} \int_{\Omega} \left(\rho^k \frac{\partial \rho^k}{\partial x} \frac{\partial^2 P^k}{\partial \rho \partial s} \phi_j + \rho^k \frac{\partial s^k}{\partial x} \frac{\partial^2 P^k}{\partial s^2} \phi_j + \rho^k \frac{\partial P^k}{\partial s} \frac{d\phi_j}{dx} \right) \frac{d\phi_i}{dx} dx,$$

$$f_i^{(1)} = \frac{1}{\Delta t} \int_{\Omega} (\rho^k - \rho^\tau) \phi_i dx + \frac{K}{\mu} \int_{\Omega} \left(\rho^k \frac{\partial P^k}{\partial \rho} \frac{\partial \rho^k}{\partial x} + \rho^k \frac{\partial P^k}{\partial s} \frac{\partial s^k}{\partial x} \right) \frac{d\phi_i}{dx} dx.$$

6.3.2 Transformation of the second equation

As a next step, we treat the transformed energy equation (equation (6.4)) and write down its weak formulation

$$\int_{\Omega} \frac{\partial s}{\partial t} \phi dx - \frac{K}{\mu} \int_{\Omega} \frac{\partial}{\partial x} \left[s \left(\frac{\partial P}{\partial \rho} \frac{\partial \rho}{\partial x} + \frac{\partial P}{\partial s} \frac{\partial s}{\partial x} \right) \right] \phi dx$$
$$- D \int_{\Omega} \frac{\partial}{\partial x} \left[\frac{\partial T}{\partial \rho} \frac{\partial \rho}{\partial x} + \frac{\partial T}{\partial s} \frac{\partial s}{\partial x} \right] \phi dx = 0.$$

Applying integration by parts to the second and third integral in the above equation, we have

$$\int_{\Omega} \frac{\partial s}{\partial t} \phi dx + \frac{K}{\mu} \int_{\Omega} \left[s \left(\frac{\partial P}{\partial \rho} \frac{\partial \rho}{\partial x} + \frac{\partial P}{\partial s} \frac{\partial s}{\partial x} \right) \right] \frac{d\phi}{dx} dx + D \int_{\Omega} \left[\frac{\partial T}{\partial \rho} \frac{\partial \rho}{\partial x} + \frac{\partial T}{\partial s} \frac{\partial s}{\partial x} \right] \frac{d\phi}{dx} dx$$
$$+ \frac{K}{\mu} \left[s \left(\frac{\partial P}{\partial \rho} \frac{\partial \rho}{\partial x} + \frac{\partial P}{\partial s} \frac{\partial s}{\partial x} \right) \phi \right]_0^1 - D \left[\frac{\partial T}{\partial \rho} \frac{\partial \rho}{\partial x} + \frac{\partial T}{\partial s} \frac{\partial s}{\partial x} \right]_0^1 = 0.$$

The boundary terms vanish by applying the boundary conditions (equation (6.8)). For the time integration, we use Euler Backward formula

$$\frac{1}{\Delta t} \int_{\Omega} (s^\tau - s^{\tau-1}) \phi dx + \frac{K}{\mu} \int_{\Omega} s^\tau \frac{\partial P^\tau}{\partial \rho} \frac{\partial \rho^\tau}{\partial x} \frac{d\phi}{dx} dx + \frac{K}{\mu} \int_{\Omega} s^\tau \frac{\partial P^\tau}{\partial s} \frac{\partial s^\tau}{\partial x} \frac{d\phi}{dx} dx$$
$$+ D \int_{\Omega} \frac{\partial T^\tau}{\partial \rho} \frac{\partial \rho^\tau}{\partial x} \frac{d\phi}{dx} dx + D \int_{\Omega} \frac{\partial T^\tau}{\partial s} \frac{\partial s^\tau}{\partial x} \frac{d\phi}{dx} dx = 0.$$

Using linearization about ρ^k and s^k, gives

$$\frac{1}{\Delta t} \int_\Omega \left(s^k + \delta s - s^{\tau-1} \right) \phi dx$$

$$+ \frac{K}{\mu} \int_\Omega \left[s^k \frac{\partial P^k}{\partial \rho} \frac{\partial \rho^k}{\partial x} + \delta s \frac{\partial P^k}{\partial \rho} \frac{\partial \rho^k}{\partial x} + s^k \left(\delta \rho \frac{\partial^2 P^k}{\partial \rho^2} + \delta s \frac{\partial^2 P^k}{\partial \rho \partial s} \right) \frac{\partial \rho^k}{\partial x} + s^k \frac{\partial P^k}{\partial \rho} \frac{\partial(\delta \rho)}{\partial x} \right] \frac{d\phi}{dx} dx$$

$$+ \frac{K}{\mu} \int_\Omega \left[s^k \frac{\partial P^k}{\partial s} \frac{\partial s^k}{\partial x} + \delta s \frac{\partial P^k}{\partial s} \frac{\partial s^k}{\partial x} + s^k \left(\delta \rho \frac{\partial^2 P^k}{\partial \rho \partial s} + \delta s \frac{\partial^2 P^k}{\partial s^2} \right) \frac{\partial s^k}{\partial x} + s^k \frac{\partial P^k}{\partial s} \frac{\partial(\delta s)}{\partial x} \right] \frac{d\phi}{dx} dx$$

$$+ D \int_\Omega \left[\frac{\partial T^k}{\partial \rho} \frac{\partial \rho^k}{\partial x} + \left(\delta \rho \frac{\partial^2 T^k}{\partial \rho^2} + \delta s \frac{\partial^2 T^k}{\partial \rho \partial s} \right) \frac{\partial \rho^k}{\partial x} + \frac{\partial T^k}{\partial \rho} \frac{\partial(\delta \rho)}{\partial x} \right] \frac{d\phi}{dx} dx$$

$$+ D \int_\Omega \left[\frac{\partial T^k}{\partial s} \frac{\partial s^k}{\partial x} + \left(\delta \rho \frac{\partial^2 T^k}{\partial \rho \partial s} + \delta s \frac{\partial^2 T}{\partial s^2} \right) \frac{\partial s^k}{\partial x} + \frac{\partial T^k}{\partial s} \frac{\partial(\delta s)}{\partial x} \right] \frac{d\phi}{dx} dx = 0.$$

Rearranging this equation so that the terms containing $\delta \rho$ come first, which are followed by the terms having δs, and lastly, the explicit terms, yields

$$\frac{K}{\mu} \int_\Omega \left(s^k \delta \rho \frac{\partial^2 P^k}{\partial \rho^2} \frac{\partial \rho^k}{\partial x} + s^k \frac{\partial P^k}{\partial \rho} \frac{\partial(\delta \rho)}{\partial x} + s^k \delta \rho \frac{\partial^2 P^k}{\partial \rho \partial s} \frac{\partial s^k}{\partial x} \right) \frac{d\phi}{dx} dx$$

$$+ D \int_\Omega \left(\delta \rho \frac{\partial^2 T^k}{\partial \rho^2} \frac{\partial \rho^k}{\partial x} + \delta \rho \frac{\partial^2 T^k}{\partial \rho \partial s} \frac{\partial s^k}{\partial x} + \frac{\partial T^k}{\partial \rho} \frac{\partial(\delta \rho)}{\partial x} \right) \frac{d\phi}{dx} dx$$

$$+ \frac{1}{\Delta t} \int_\Omega \delta s \, \phi dx + \frac{K}{\mu} \int_\Omega \left(\delta s \frac{\partial P^k}{\partial \rho} \frac{\partial \rho^k}{\partial x} + s^k \delta s \frac{\partial^2 P^k}{\partial \rho \partial s} \frac{\partial \rho^k}{\partial x} \right.$$

$$\left. + \delta s \frac{\partial P^k}{\partial s} \frac{\partial s^k}{\partial x} + s^k \delta s \frac{\partial^2 P^k}{\partial s^2} \frac{\partial s^k}{\partial x} + s^k \frac{\partial P^k}{\partial s} \frac{\partial(\delta s)}{\partial x} \right) \frac{d\phi}{dx} dx$$

$$+ D \int_\Omega \left(\frac{\partial^2 T^k}{\partial \rho \partial s} \frac{\partial \rho^k}{\partial x} + \frac{\partial^2 T^k}{\partial s^2} \frac{\partial s^k}{\partial x} \right) \delta s \frac{d\phi}{dx} dx + D \int_\Omega \frac{\partial T^k}{\partial s} \frac{\partial(\delta s)}{\partial x} \frac{d\phi}{dx} dx$$

$$+ \frac{1}{\Delta t} \int_\Omega (s^k - s^{\tau-1}) \phi dx + \frac{K}{\mu} \int_\Omega s^k \left(\frac{\partial P^k}{\partial \rho} \frac{\partial \rho^k}{\partial x} + \frac{\partial P^k}{\partial s} \frac{\partial s^k}{\partial x} \right) \frac{d\phi}{dx} dx$$

$$+ D \int_\Omega \left(\frac{\partial T^k}{\partial \rho} \frac{\partial \rho^k}{\partial x} + \frac{\partial T^k}{\partial s} \frac{\partial s^k}{\partial x} \right) \frac{d\phi}{dx} dx = 0.$$

Applying the approximation for $\delta\rho$ and δs as defined in the case of mass equation, we have

$$\frac{K}{\mu}\sum_{j=1}^{N}\delta\rho_j\int_{\Omega}\left(s^k\frac{\partial^2 P^k}{\partial\rho^2}\frac{\partial\rho^k}{\partial x}\phi_j + s^k\frac{\partial P^k}{\partial\rho}\frac{\partial\phi_j}{\partial x} + s^k\frac{\partial^2 P^k}{\partial\rho\partial s}\frac{\partial s^k}{\partial x}\phi_j\right)\frac{d\phi_i}{dx}dx$$

$$+ D\sum_{j=1}^{N}\delta\rho_j\int_{\Omega}\left(\frac{\partial^2 T^k}{\partial\rho^2}\frac{\partial\rho^k}{\partial x} + \frac{\partial^2 T^k}{\partial\rho\partial s}\frac{\partial s^k}{\partial x}\right)\phi_j\frac{d\phi_i}{dx}dx + D\sum_{j=1}^{N}\delta\rho_j\int_{\Omega}\frac{\partial T^k}{\partial\rho}\frac{d\phi_i}{dx}\frac{d\phi_j}{dx}dx$$

$$+ \frac{1}{\Delta t}\sum_{j=1}^{N}\delta s_j\int_{\Omega}\phi_i\phi_j dx + \frac{K}{\mu}\sum_{j=1}^{N}\delta s_j\int_{\Omega}\left(\frac{\partial P^k}{\partial\rho}\frac{\partial\rho^k}{\partial x}\phi_j + s^k\frac{\partial^2 P^k}{\partial\rho\partial s}\frac{\partial\rho^k}{\partial x}\phi_j\right.$$

$$\left. + \frac{\partial P^k}{\partial s}\frac{\partial s^k}{\partial x}\phi_j + s^k\frac{\partial^2 P^k}{\partial s^2}\frac{\partial s^k}{\partial x}\phi_j + s^k\frac{\partial P^k}{\partial s}\frac{\partial\phi_j}{\partial x}\right)\frac{d\phi_i}{dx}dx$$

$$+ D\sum_{j=1}^{N}\delta s_j\int_{\Omega}\left(\frac{\partial^2 T^k}{\partial\rho\partial s}\frac{\partial\rho^k}{\partial x} + \frac{\partial^2 T^k}{\partial s^2}\frac{\partial s^k}{\partial x}\right)\phi_j\frac{d\phi_i}{dx}dx + D\sum_{j=1}^{N}\delta s_j\int_{\Omega}\frac{\partial T^k}{\partial s}\frac{d\phi_i}{dx}\frac{d\phi_j}{dx}dx$$

$$+ \frac{1}{\Delta t}\int_{\Omega}(s^k - s^{\tau-1})\phi_i dx + \frac{K}{\mu}\int_{\Omega}\left(s^k\frac{\partial P^k}{\partial\rho}\frac{\partial\rho^k}{\partial x} + s^k\frac{\partial P^k}{\partial s}\frac{\partial s^k}{\partial x}\right)\frac{d\phi_i}{dx}dx$$

$$+ D\int_{\Omega}\left(\frac{\partial T^k}{\partial\rho}\frac{\partial\rho^k}{\partial x} + \frac{\partial T^k}{\partial s}\frac{\partial s^k}{\partial x}\right)\frac{d\phi_i}{dx}dx = 0.$$

The equivalent matrix form is given by

$$S^{(21)}\,\delta\rho + S^{(22)}\,\delta s + f^{(2)} = 0. \tag{6.11}$$

The elements of these matrices and vector are defined as

$$S_{ij}^{(21)} = \frac{K}{\mu}\int_{\Omega}\left(s^k\frac{\partial^2 P^k}{\partial\rho^2}\frac{\partial\rho^k}{\partial x}\phi_j + s^k\frac{\partial P^k}{\partial\rho}\frac{\partial\phi_j}{\partial x} + s^k\frac{\partial^2 P^k}{\partial\rho\partial s}\frac{\partial s^k}{\partial x}\phi_j\right)\frac{d\phi_i}{dx}dx$$

$$+ D\int_{\Omega}\left(\frac{\partial^2 T^k}{\partial\rho^2}\frac{\partial\rho^k}{\partial x} + \frac{\partial^2 T^k}{\partial\rho\partial s}\frac{\partial s^k}{\partial x}\right)\phi_j\frac{d\phi_i}{dx}dx + D\int_{\Omega}\frac{\partial T^k}{\partial\rho}\frac{d\phi_i}{dx}\frac{d\phi_j}{dx}dx,$$

$$S_{ij}^{(22)} = \frac{1}{\Delta t}\int_{\Omega}\phi_i\phi_j dx + \frac{K}{\mu}\int_{\Omega}\left(\frac{\partial P^k}{\partial\rho}\frac{\partial\rho^k}{\partial x}\phi_j + s^k\frac{\partial^2 P^k}{\partial\rho\partial s}\frac{\partial\rho^k}{\partial x}\phi_j\right.$$

$$\left. + \frac{\partial P^k}{\partial s}\frac{\partial s^k}{\partial x}\phi_j + s^k\frac{\partial^2 P^k}{\partial s^2}\frac{\partial s^k}{\partial x}\phi_j + s^k\frac{\partial P^k}{\partial s}\frac{\partial\phi_j}{\partial x}\right)\frac{d\phi_i}{dx}dx$$

$$+ D\int_{\Omega}\left(\frac{\partial^2 T^k}{\partial\rho\partial s}\frac{\partial\rho^k}{\partial x} + \frac{\partial^2 T^k}{\partial s^2}\frac{\partial s^k}{\partial x}\right)\phi_j\frac{d\phi_i}{dx}dx + D\int_{\Omega}\frac{\partial T^k}{\partial s}\frac{d\phi_i}{dx}\frac{d\phi_j}{dx}dx,$$

$$f_i^{(2)} = \frac{1}{\Delta t}\int_{\Omega}(s^k - s^{\tau-1})\phi_i dx + \frac{K}{\mu}\int_{\Omega}\left(s^k\frac{\partial P^k}{\partial\rho}\frac{\partial\rho^k}{\partial x} + s^k\frac{\partial P^k}{\partial s}\frac{\partial s^k}{\partial x}\right)\frac{d\phi_i}{dx}dx$$

$$+ D\int_{\Omega}\left(\frac{\partial T^k}{\partial\rho}\frac{\partial\rho^k}{\partial x} + \frac{\partial T^k}{\partial s}\frac{\partial s^k}{\partial x}\right)\frac{d\phi_i}{dx}dx.$$

6.3.3 Comparison of numerical the results from two approaches

Equations (6.10) and (6.11) can be written in the following block matrix form

$$
\begin{bmatrix} S^{(11)} & S^{(12)} \\ S^{(21)} & S^{(22)} \end{bmatrix} \begin{bmatrix} \delta\rho \\ \delta s \end{bmatrix} = - \begin{bmatrix} f^{(1)} \\ f^{(2)} \end{bmatrix}. \tag{6.12}
$$

or

$$
G^{k+1} = G^k - J^{-1}F, \tag{6.13}
$$

where J is the Jacobian matrix. The matrices used in the above equation are defined as

$$
J = \begin{bmatrix} S^{(11)} & S^{(12)} \\ S^{(21)} & S^{(22)} \end{bmatrix}, \qquad F = \begin{bmatrix} f^{(1)} \\ f^{(2)} \end{bmatrix}, \qquad G^k = \begin{bmatrix} \rho^k \\ s^k \end{bmatrix}.
$$

Equation (6.13) is solved by a direct method (Gaussian elimination). In Figure 6.3(a)-(c), the relative difference of density, total enthalpy, and temperature with respect to the "many-equations" model are provided. For instance, $\Delta T(t)$ is defined as

$$
\Delta T(t) = \frac{\left| T^{(1)}(t) - T^{(2)}(t) \right|}{\|T^{(1)}(t)\|}, \quad \text{where } \|T^{(1)}(t)\| = \sqrt{\frac{\sum_{i=1}^{N} \left(T^{(1)}(t) \right)^2}{N}}, \tag{6.14}
$$

where $T(t)^{(1)}$ is the solution obtain by using the original "many-equation" model and $T(t)^{(2)}$ is the solution by "two-equation" approach. The definitions of $\Delta\rho$ and Δs are analogous. The number of Newton iterations per time step is also plotted over the time sequence. The error that we see is due to the numerical truncation errors. From these results, we conclude that the two-equations model is an equivalent representation of the system given by equations (3.1) to (3.5).

6.4 Approximation by a linear system

We approximate the two-equations model by a linear system in the following way. As a first step, the constants a, b, c, and d are computed from $\{(T, X_G)|280 \le T \le 360,\ 0 \le X_G \le 1\}$. Their values are given by

$$
A = \begin{bmatrix} a & b \\ c & d \end{bmatrix} = \begin{bmatrix} D_{11} & D_{12} \\ D_{21} & D_{22} \end{bmatrix} = \begin{bmatrix} \frac{K}{\mu}\rho\frac{\partial P}{\partial\rho} & \frac{K}{\mu}\rho\frac{\partial P}{\partial s} \\ \frac{K}{\mu}s\frac{\partial P}{\partial\rho} + D\frac{\partial T}{\partial\rho} & \frac{K}{\mu}s\frac{\partial P}{\partial s} + D\frac{\partial T}{\partial s} \end{bmatrix}.
$$

These constants are used in the approximate system, given as

$$
\frac{\partial\rho}{\partial t} = \frac{\partial}{\partial x}\left(a\frac{\partial\rho}{\partial x} + b\frac{\partial s}{\partial x} \right),
$$

$$
\frac{\partial s}{\partial t} = \frac{\partial}{\partial x}\left(c\frac{\partial\rho}{\partial x} + d\frac{\partial s}{\partial x} \right).
$$
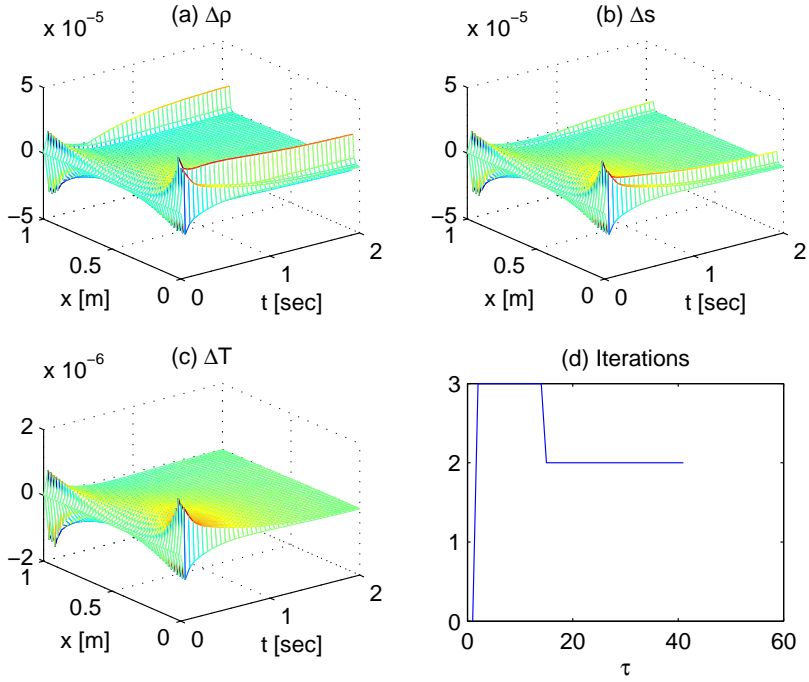
Figure 6.3: Comparison of two-equation model with the original system. The solution plots are (a) $\Delta\rho(t)$,(b) $\Delta s(t)$, (c) $\Delta T(t)$, and (d) Newton iterations/timestep

We compute the eigenvalues of A to determine the stability of this linear system. Let λ be an eigenvalue of A, then it is computed as

$$|A - \lambda I| = 0,$$

where I is a unity matrix of 2×2. Hence, we solve

$$(a - \lambda)(d - \lambda) - bc = 0,$$
$$\lambda^2 - (a + d)\lambda + ad - bc = 0.$$

The solution is given by

$$\lambda = \frac{1}{2}\left(a + d \pm \sqrt{(a + d)^2 - 4(ad - bc)}\right).$$

We show that $ad = bc$ in the following expressions. Here we make use of the fact that $P = P(T)$, i.e., $\frac{\partial P}{\partial \rho} = \frac{\partial P}{\partial T} \frac{\partial T}{\partial \rho}$ and $\frac{\partial P}{\partial s} = \frac{\partial P}{\partial T} \frac{\partial T}{\partial s}$.

$$
\begin{aligned}
ad &= \frac{K}{\mu} \rho \frac{\partial P}{\partial \rho} \left(\frac{K}{\mu} s \frac{\partial P}{\partial s} + D \frac{\partial T}{\partial s} \right), \\
&= \frac{K^2}{\mu^2} \rho s \frac{\partial P}{\partial \rho} \frac{\partial P}{\partial s} + D \frac{K}{\mu} \rho \frac{\partial P}{\partial \rho} \frac{\partial T}{\partial s}, \\
&= \frac{K^2}{\mu^2} \rho s \frac{\partial P}{\partial \rho} \frac{\partial P}{\partial s} + D \frac{K}{\mu} \rho \frac{\partial P}{\partial T} \frac{\partial T}{\partial \rho} \frac{\partial T}{\partial s}.
\end{aligned}
\tag{6.15}
$$

Similarly

$$
\begin{aligned}
bc &= \frac{K}{\mu} \rho \frac{\partial P}{\partial s} \left(\frac{K}{\mu} s \frac{\partial P}{\partial \rho} + D \frac{\partial T}{\partial \rho} \right), \\
&= \frac{K^2}{\mu^2} \rho s \frac{\partial P}{\partial s} \frac{\partial P}{\partial \rho} + D \frac{K}{\mu} \rho \frac{\partial P}{\partial s} \frac{\partial T}{\partial \rho}, \\
&= \frac{K^2}{\mu^2} \rho s \frac{\partial P}{\partial s} \frac{\partial P}{\partial \rho} + D \frac{K}{\mu} \rho \frac{\partial P}{\partial T} \frac{\partial T}{\partial s} \frac{\partial T}{\partial \rho}.
\end{aligned}
\tag{6.16}
$$

Comparing expressions (6.15) and (6.16), we have

$$ad = bc.$$

Therefore, the eigenvalues of A are given by $\{0, \ \frac{K}{\mu} \rho \frac{\partial P}{\partial \rho} + \frac{K}{\mu} s \frac{\partial P}{\partial s} + D \frac{\partial T}{\partial s}\}$ or equivalently

$$
\lambda = \begin{cases} \{0, \ 0\} & \text{for } a + d = 0, \\ \{0, \ a + d\} & \text{for } a + d \neq 0. \end{cases}
$$

It is difficult to determine $a + d$ analytically. We numerically computed this value for the entire $(\rho, \ s)$-diagram, and it is given by $0.073 < a + d < 2.344$ for $0 \leq X_G \leq 1$ and $280 \leq T \leq 360$. Since the eigenvalues of the Laplacian operator are non-positive, the original system is unconditionally stable. Therefore, the solution qualitatively behaves in the following way

$$
\rho(x, t) = \alpha(x) e^{-\lambda t} + \beta(x),
$$
$$
s(x, t) = \rho(x, t) h(x),
$$

where $h(x, t) = h(x)$ is determined experimentally.

6.4.1   Possibility of one state variable

Since $P = P(T)$, one of the eigenvalues is zero for the entire phase diagram. Hence, the linearized system can be reformulated such that only one variable is sufficient to describe system dynamics. This can be achieved by diagonalization of A. This conclusion can only be drawn for a linear system. However, we checked the possibility

Table 6.1: One state variable

Δx	Δt	$K\ [m^2]$	$\mu\ [P_a\ s]$	$D\ [W/m/K]$
1/100	1/100	5×10^{-11}	5×10^{-5}	0.05

$X_G(x, 0) = 0.2$		

$$T(x,0) = \begin{cases} 290 & \text{for } 0 \le x < .05, \\ 290 + \frac{20}{9}x - \frac{1}{9} & \text{for } 0.05 \le x \le 0.95, \\ 292 & \text{for } 0.95 < x \le 1. \end{cases}$$
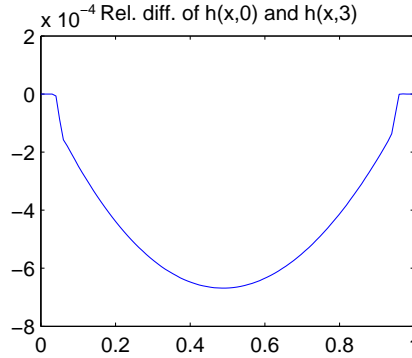
Figure 6.4: Relative difference Δh between initial $h^{(1)}$ and steady-state $h^{(2)}$ for original system. $\Delta h = \frac{|h^{(1)} - h^{(2)}|}{\|h^{(1)}\|}$, where $\|h^{(1)}\| = \sqrt{\frac{\sum_{i=1}^{N} (h^{(1)})^2}{N}}$.

of one state variable, experimentally. The initial conditions, which we use here, are given in Table 6.1. Figure 6.4 shows the relative difference between the initial and steady state value of h, when the initial conditions from Table 6.1 are used by the original (6-equation) model. The relative difference used in this section has the following definition

$$\Delta h = \frac{|h^{(1)} - h^{(2)}|}{\|h^{(1)}\|}, \quad \text{where } \|h^{(1)}\| = \sqrt{\frac{\sum_{i=1}^{N} \left(h_i^{(1)}\right)^2}{N}},$$

where $h^{(1)}$ is the initial enthalpy and $h^{(2)}$ is the enthalpy, when system approaches to a steady-state. No significant relative difference between the two values is observed.

In an another experiment, we only take the mass equation and ignore the energy equation. In other words, the original system is approximated by one equation only. The simulation results are comparable to the original model and they are given in Figure 6.5. The relative error for the temperature variable is small but wiggly. The reason behind these wiggles is not known at present.
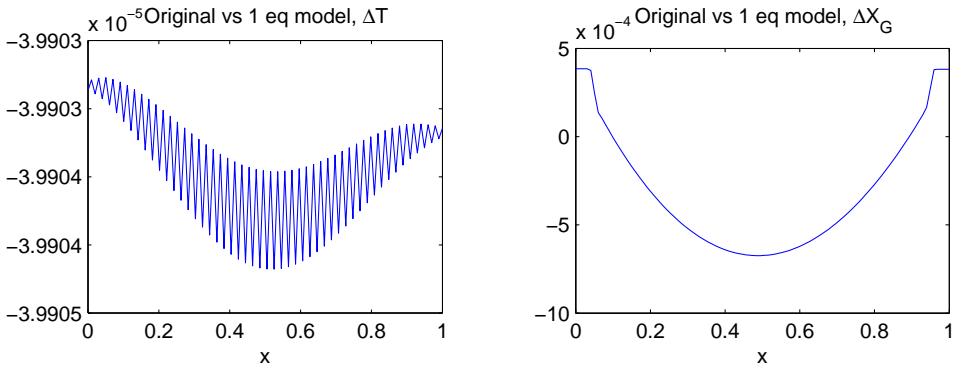
Figure 6.5: Comparison of variables from the original system and one-equation model at steady-state. (left) Relative difference in T and (right) relative difference in X_G.

The Gibbs phase rule

The Gibbs phase rule is given by the following relation [21]

$$F = C - \Phi + 2,$$

where

F = number of degrees of freedom,

C = number of component (or substances),

Φ = number of phases in thermodynamic equilibrium with each other.

For our system, $C = 1$ because the only substance here is Propane, $\Phi = 2$, for a two phase flow. Therefore, the results we obtained are consistent with the Gibbs phase rule, in which, one equation is sufficient to solve the system for a two phase flow.

6.5 Error estimation with Richardson's extrapolation

In Chapter 3 and 4, we face the necessity for a small time-step for convergence where, the IMEX or Picard methods are used. Therefore, the Richardson extrapolation can not be carried out satisfactorily. Therefore, we place this section (about the error estimate) in this chapter where the system stability is already investigated.

Let G be the analytical solution of the system given by Equation (3.1) to (3.5). Further, let $\hat{G}$ be the numerical solution obtained with a time-step Δt and a spatial step Δx (1D case). Since we use finite elements with linear basis function (for spatial discretization) and Euler backward scheme for time integration, the error $G - \hat{G}$ is of order $O(\Delta x^2 + \Delta t)$.

Table 6.2: Example for error estimation, initial conditions

Δx	Δt	$K\ [m^2]$	$\mu\ [P_a\ s]$	$D\ [W/m/K]$
1/5, 1/10	1/10000	5×10^{-11}	5×10^{-5}	0.05

$X_G(x, 0) = 0.1$		
$T(x, 0) = 301 + \sin(\pi x)$		

Table 6.3: Numerical values of a and c, dependence of Δx

Δx	Δt	a	c
1/5,	1/10000	2.3464	0.0332
1/10,	1/10000	2.1832	0.0063

To verify that above mentioned order of the error is correct for our case, we solve two examples. In the first example, we take a small Δt that is, $\Delta t \ll \Delta x^2$, so that $O(\Delta x^2)$ represents order of the error, satisfactorily. The initial conditions used for this example are given in Table 6.2. Note that the same example is solved for two values of Δx.

We select one of the solution variables (say T) for the error estimation. We represent the temperature values by $T^{(1)}$, $T^{(2)}$, and $T^{(3)}$ computed by using Δx, $\Delta x/2$, and $\Delta x/4$, respectively. Following the procedure given in [38], we model the error by the following equations

$$T - T^{(1)} = c(\Delta x)^a, \tag{6.17}$$

$$T - T^{(2)} = c(\Delta x/2)^a, \tag{6.18}$$

$$T - T^{(3)} = c(\Delta x/4)^a, \tag{6.19}$$

Subtract the first two and last two relations to eliminate T. We have

$$T^{(2)} - T^{(1)} = c(\Delta x)^a \left(1 - \left(\frac{1}{2}\right)^a\right), \tag{6.20}$$

$$T^{(3)} - T^{(2)} = c(\Delta x/2)^a \left(1 - \left(\frac{1}{2}\right)^a\right). \tag{6.21}$$

Division of one expression by the other eliminates c. This gives

$$a = \log_2\left(\frac{T^{(2)} - T^{(1)}}{T^{(3)} - T^{(2)}}\right). \tag{6.22}$$

Once the value of a is known, c can be determined by using Equation (6.20). The values of a and c as determined for this example are summarized in Table 6.3. We compute a and c at all grid nodes and the scaled $\|.\|_2$ values are given in Table 6.3. Furthermore, the given values are computed at $t = 1$, where the system is close to its steady-state. Note that these results are for T but other system variables give similar values of a and c.

Table 6.4: Numerical values of b and d, dependence of Δt

Δt	Δx	b	d
1/10,	1/1000	0.9946	0.0350
1/20,	1/1000	1.0110	0.0177

In the next example, we take $\Delta x^2 \ll \Delta t$ so that the numerical error, approximately, is of order $O(\Delta t)$. Let the error in this case is modeled by

$$T - \hat{T} = d(\Delta t)^b, \tag{6.23}$$

where $\hat{T}$ is the numerical value of the temperature. The procedure to compute b and d is analogous to the earlier discussion of this section. The numerical values of b and d are given in Table 6.4 (for two values of Δt), computed at $t = 0.2$ [s]. The value of b increases with t. From the discussion and examples of this section, we conclude that the numerical error in our case is, approximately, of order $O(\Delta x^2 + \Delta t)$.

6.6 Conclusions

For stability analysis, the original system is transformed to a "two-equations" model. This can further be approximated by a linear "two-equations" system. The eigenvalues of the linear system suggest that the original nonlinear system is stable for the given range of T and X_G (or ρ and h). We also conclude that the system obeys the Gibbs phase rule, at least for a two-phase flow. Furthermore, we have shown that the error in the numerical solution is approximately of the order $O(\Delta x^2 + \Delta t)$.

7

Chapter

On nonhomogeneous Robin boundary conditions

In this chapter, nonhomogeneous Robin boundary conditions are used and therefore, we have mass and energy fluxes across the boundaries. Originally, the nonhomogeneous Robin boundary conditions are given in Chapter 3 (Equations (3.8) and (3.9)). But many of the simulation results there, exhibit steep gradients and abrupt changes near the boundary. In Chapter 4, we show that nonhomogeneous boundary conditions give an ill-posed problem, in most cases. In the current chapter, we reconsider these boundary conditions, with a better understanding of the selection criterion of the environmental parameters ρ_a, h_a, and T_a and the transfer coefficients, k_m and k_h. They are chosen in such a way that we obtain smooth results, which can be explained on the basis of physical laws.

A summary of the current chapter is as follows. We try to find certain conditions about the heat diffusion and the system enthalpy, so that the application of nonhomogeneous boundary conditions should not make the problem ill-posed. For this purpose, we observe the diffusion of heat within the system and across the boundaries, in the first two sections. In our experiments, the diffusion of heat is found insignificant for isolated systems. This motivated us to investigate the energy flux across the boundaries. A comparison of convective and diffusive terms in the boundary equations reveals that we have a very small (insignificant) diffusion of heat across the boundaries. For this comparison, we estimated k_h, by using initial conditions and other parameters. Furthermore, the system enthalpy is found approximately static, for an isolated system. This motivates us to avoid jumps in the enthalpy profile at the boundary, which is achieved by setting $h_a = h_\Gamma$. This choice of h_a and other ambient parameters, in a specific way, leads to smooth and physically acceptable solutions.

Note that the solution algorithm, given in Chapter 5, is used in this chapter. However, we will use $1D$ examples, because it is easier to show the complete time history, for spatially $1D$ variables. Therefore, $\boldsymbol{x} = (x, y)$ is mentioned during analytic treat-

ment of the boundary conditions. But, we only specify the x-axis in the sections with simulations.

7.1 Diffusion of heat within the system

For two phase flow, one state variable is sufficient to describe an isolated system (subject to conditions for the Gibbs phase rule). In other words, solving any of the mass or energy equations solves the system completely. In case, we solve the system by using the mass equation alone (Equation (3.1)), then clearly, the solution is independent of the value of D or $D\frac{\partial^2 T}{\partial x^2}$. For a consistent model, the energy equation alone (Equation (3.2)) or the both equations, taken together, should give the same results (i.e., a solution, independent of D).

In the following examples, we take the complete system (i.e., both, mass and energy equations) and demonstrate, by experiments, that the diffusion of T is negligible, for the parameters and conditions, that we use. We consider an isolated system ($k_m = 0$, $k_h = 0$). The $1D$ boundary conditions, in this case, are mentioned as

$$\rho v = 0, \quad x \in \Gamma, \ t > 0,$$

$$\rho h v - D\frac{\partial T}{\partial x} = 0, \quad x \in \Gamma, \ t > 0.$$

Furthermore, we solve the system for $\Delta x = 1/100$ but plot them with a reduced resolution for the sake of better printing.

7.1.1 Example: No flow conditions

We set the initial conditions and other parameters, as given in Table 7.1. With these

Table 7.1: Example: No flow conditions

Δx	Δt	D	k_m	k_h
1/100	1/20	1000	0	0

$T(x, 0) = 290$		
$X_G(x, 0) = \begin{cases} 0.1 & \text{for } 0 \leq x < .45, \\ x - 0.35 & \text{for } 0.45 \leq x \leq 0.55, \\ 0.2 & \text{for } 0.55 < x \leq 1. \end{cases}$		

initial conditions, the simulation results are provided in Figure 7.1. For a constant temperature, $\frac{\partial T}{\partial x}$ and $\frac{\partial^2 T}{\partial x^2}$ are zero. Therefore, we do not expect that D (in this case) will affect the solution variables. In Section 4.1.1, we mentioned that $P = P(T)$. Now, the velocity can be determined as

$$v = -\frac{K}{\mu}\frac{\partial P}{\partial x} = -\frac{K}{\mu}\frac{\partial P}{\partial T}\frac{\partial T}{\partial x} = 0.$$

For a zero velocity, the mass and energy equations reduce to

$$\frac{\partial \rho}{\partial t} = 0, \qquad \text{(mass equation with } v = 0\text{)},$$

$$\frac{\partial s}{\partial t} = 0, \qquad \text{(energy equation with } v = 0\text{)},$$

which shows that all the solution variables remain static even though X_G, ρ, and h are step functions in x. This is illustrated in Figure 7.1 (for X_G and ρ).
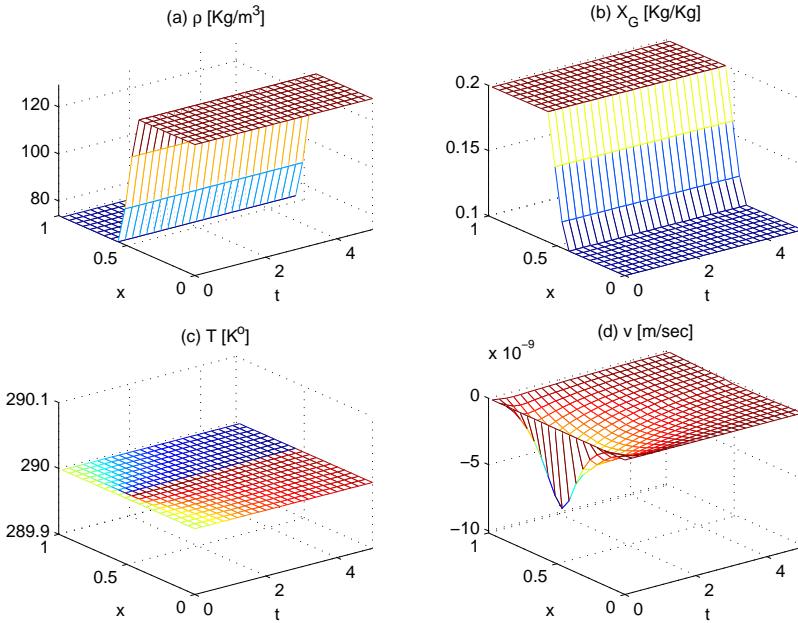
Figure 7.1: Example: No flow conditions. Initially, a step X_G and a constant T.

7.1.2 Example: Nonzero initial velocity

In this example, we show that D or $D\frac{\partial^2 T}{\partial x^2}$ play an insignificant role for the solution we get in the setting that is used in this thesis. We use a piecewise linear $T(x, 0)$ (consistent with the boundary conditions) and a constant $X_G(x, 0)$, as given in Table 7.2. For comparison, we compute the solution with two values of diffusivity, $D = 0.1$ and $D = 10$. In Figure 7.2(a) and (b), actual variables are plotted, where $D = 0.1$ is used. But, the plots are the same (by an eyeball norm) when $D = 10$ is used. In Figure 7.2(c), the maximum value of the relative difference at each time step, of $\rho^{(1)}$ and $\rho^{(2)}$, is plotted. Here, $\rho^{(1)}$ is the density with $D = 0.1$ and $\rho^{(2)}$ is computed with $D = 10$.

Table 7.2: Example: Nonzero initial velocity

Δx	Δt	D	k_m	k_h
1/100	1/20	0.1 and 10	0	0

$$T(x,0) = \begin{cases} 290, & \text{for } x \in [0, 0.05], \\ 290 + \frac{20}{9}x - \frac{1}{9}, & \text{for } x \in]0.05, 0.95], \\ 292, & \text{for } x \in]0.95, 1], \end{cases}$$

$$X_G(x,0) = 0.15$$

Figure 7.2: Example: Nonzero initial velocity. (a) Density (ρ) for $D = 0.1$. (b) Gas mass fraction (X_G). (c) Maximum of relative difference, $\Delta\rho(t)$, of $\rho^{(1)}(t)$ and $\rho^{(2)}(t)$ defined by Equation (7.2). (d) Maximum relative difference, $\Delta X_G(t)$, of $X_G^{(1)}(t)$ and $X_G^{(2)}(t)$, analogous to $\Delta\rho(t)$

Their relative difference $\Delta\boldsymbol{\rho}^{(3)}$ is defined as

$$\Delta\boldsymbol{\rho}^{(3)}(t) = \frac{\left|\boldsymbol{\rho}^{(1)}(t) - \boldsymbol{\rho}^{(2)}(t)\right|}{\|\boldsymbol{\rho}^{(1)}(t)\|}, \quad \text{where } \|\rho^{(1)}(t)\| = \sqrt{\frac{\sum_{i=1}^{N}\left(\rho_i^{(1)}(t)\right)^2}{N}}. \tag{7.1}$$
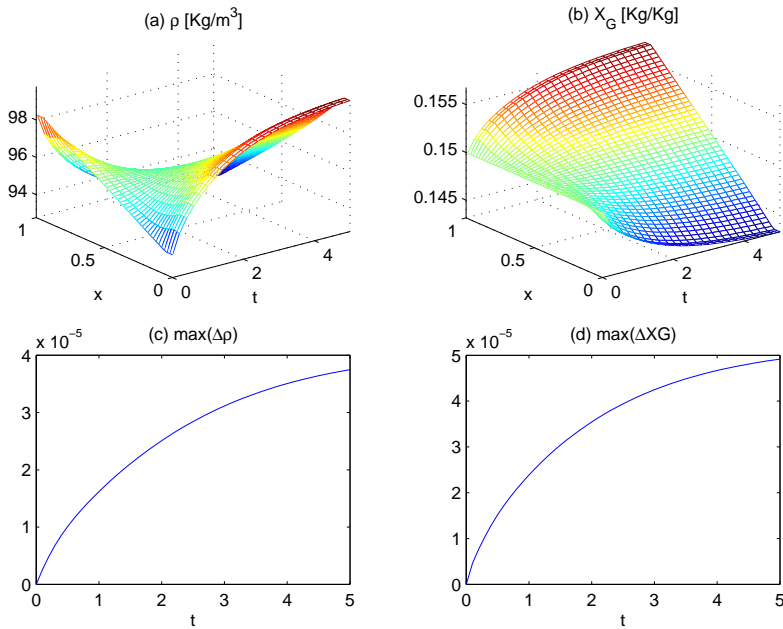
We take the maximum value from each element of this vector. This gives us the maximum relative difference between $\boldsymbol{\rho}^{(1)}$ and $\boldsymbol{\rho}^{(2)}$ at t.

$$\Delta\rho(t) = \max(\Delta\boldsymbol{\rho}^{(3)}(t)). \tag{7.2}$$

From Figure 7.2 we observe that changing the heat diffusion coefficient D, by a factor of one hundred, does not alter the solution variables significantly. We conclude that $D\frac{\partial^2 T}{\partial x^2}$ plays a very insignificant role in this case. Note that, there is some diffusion of ρ because of the diffusion terms in Equations (6.5) and (6.6). Furthermore, in Section 5.3.3 the phase front is found to obey a square-root law which indicates mass diffusion.

7.2 Diffusion of heat across the boundaries

We start with the $2D$ boundary conditions (Equations (4.9) and (4.10))

$$\rho\boldsymbol{v} \cdot \hat{\boldsymbol{n}} = k_m(\rho - \rho_a), \quad x \in \Gamma, \quad t > 0, \tag{7.3}$$

$$-D\boldsymbol{\nabla}T \cdot \hat{\boldsymbol{n}} + s\boldsymbol{v} \cdot \hat{\boldsymbol{n}} = k_h(T - T_a) + \begin{cases} h_\Gamma k_m(\rho - \rho_a), & \text{for } \boldsymbol{v} \cdot \hat{\boldsymbol{n}} < 0, \\ h_a k_m(\rho - \rho_a), & \text{for } \boldsymbol{v} \cdot \hat{\boldsymbol{n}} > 0, \end{cases} \tag{7.4}$$

We choose $h_a = h_\Gamma$ and hence, Equation (7.4) is written as

$$-D\boldsymbol{\nabla}T \cdot \hat{\boldsymbol{n}} + \rho h_\Gamma \boldsymbol{v} \cdot \hat{\boldsymbol{n}} = k_h(T - T_a) + h_\Gamma k_m(\rho - \rho_a). \tag{7.5}$$

Multiply Equation (7.3) by h_Γ and subtract it from Equation (7.8), to obtain

$$-D\boldsymbol{\nabla}T \cdot \hat{\boldsymbol{n}} = k_h(T - T_a). \tag{7.6}$$

In Section 4.1.1, we show that $P = P(T)$ is a monotonic function, therefore, T is also a function of P i.e., $T = T(P)$. Now, we estimate k_h[1], for the given values of k_m, ρ_a, h_a, and T_a. Note that ρ_a is selected such that $T_a = T(\rho_a, h_a)$ is the desired temperature at the boundary. When T_a is a constant, it is also the steady state temperature value of the system. The value of k_m depends on a desired mass flux. In our simulation examples, a typical value of k_m is between zero and 5. From these values and the initial conditions $T(x, 0)$ and $\rho(x, 0)$, we can estimate k_h. In Chapter 4, we show that an arbitrary value of k_h results in an ill posed problem. From Equation (7.6), we have

$$k_h(T - T_a) = -D\boldsymbol{\nabla}T \cdot \hat{\boldsymbol{n}} = -D\frac{\partial T}{\partial P}\boldsymbol{\nabla}P \cdot \hat{\boldsymbol{n}} = D\frac{\mu}{K}\frac{\partial T}{\partial P}\boldsymbol{v} \cdot \hat{\boldsymbol{n}}.$$

---

[1]The value of k_h should be determined physically. In Chapter 4, however, we have shown that arbitrary value of k_h makes the problem ill-posed.

We use the value of $v \cdot \hat{n}$ from Equation (7.3)

$$k_h(T - T_a) = D\frac{\mu}{K}k_m\frac{\rho - \rho_a}{\rho}\frac{\partial T}{\partial P},$$

or

$$k_h = k_m\frac{D\mu}{K\rho}\frac{(\rho - \rho_a)}{(T - T_a)}\frac{\partial T}{\partial P}.$$

In this estimation, we use the initial values of ρ and T. The typical value of k_h in our examples, comes out, is less than one. For the data set given in Table 7.3, we get

Table 7.3: Estimation of k_h

k_m	T_a	$T(x,0)$	$X_G(x,0)$	μ [$P_a.s$]	K [m^2]
2	305	295	0.2	5×10^{-5}	10^{-10}

$h_a = 1.35 \times 10^5$ [J/K_g] and $k_h = 0.44$ [$W/m^2/K$]. Therefore, the contribution of the diffusive and convective terms, in the boundary condition for the energy equation, is given by

$$k_h|T - T_a| \approx 4.4,$$

$$h_a k_m|\rho - \rho_a| \approx 5 \times 10^6.$$

Practically, the boundary conditions act as if there is no diffusion of T i.e.,

$$\rho h v \cdot \hat{n} - D\nabla T \cdot \hat{n} = h_\Gamma k_m(\rho - \rho_a).$$

We conclude that, the diffusion of heat does not play a significant role in our setting of numerical experiments (i.e., for Propane, the given phase diagrams, and other parameters). For other substances, or parameter settings, the diffusion of heat might be larger[2].

7.3   The choice of h_a and T_a

In general, we observe a static enthalpy, h, for isolated systems even if all other variables are dynamic. h varies very slightly at relatively high velocities. A static h is consistent with the Gibbs Phase Rule which allows only one of the variables between (ρ, h) to be dynamic for a two phase flow.

A static enthalpy within the system motivated us to investigate the choice of h_a. Consider the boundary conditions for an inflow (i.e., $\rho v \cdot \hat{n} < 0$)

$$\rho v \cdot \hat{n} = k_m(\rho - \rho_a), \quad x \in \Gamma, \quad t > 0, \tag{7.7}$$

$$-D\nabla T \cdot \hat{n} + \rho h_\Gamma v \cdot \hat{n} = k_h(T - T_a) + h_a k_m(\rho - \rho_a). \tag{7.8}$$

---

[2]Currently, the available database is for Propane and the physical parameters, which we use, are taken from [12].
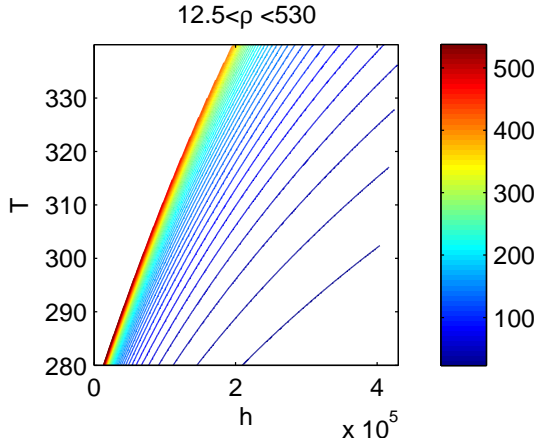
Figure 7.3: Constant density curves, used to select ρ_a for a desired T_a.

Table 7.4: Example: Large jump in the enthalpy

k_m	$T(x,0)$	$X_G(x,0)$	h_a
1.5	290	0.2	$2h(0,0)$

In the first two sections of this chapter, we found that the diffusion terms ($D\frac{\partial T}{\partial x}$ and $k_h(T - T_a)$), in our case, are very small as compared to the other terms. Hence, we can write

$$\rho h_\Gamma \boldsymbol{v} \cdot \hat{\boldsymbol{n}} \approx h_a k_m (\rho - \rho_a). \tag{7.9}$$

We use the value of $\rho \boldsymbol{v} \cdot \hat{\boldsymbol{n}}$ (from Equation (7.3)), into the above equation, to obtain

$$h_\Gamma k_m (\rho - \rho_a) \approx h_a k_m (\rho - \rho_a), \tag{7.10}$$

which implies

$$h_\Gamma = h_a.$$

Therefore, the ambient enthalpy should be selected equal to the enthalpy at the boundary. A large difference between h_Γ and h_a leads to an ill-posed problem. For the outflow case the ambient enthalpy, h_a, does not play a role.

In our view, the ambient parameters ρ_a, T_a, and h_a can not be chosen arbitrarily. Furthermore, inflow and outflow can not be separated. For inflow, h_a should be equal to h_Γ. The value of ρ_a should be selected such that $T_a = T(\rho_a, h_a)$ is the desired temperature at the boundary. In our case, we can determine ρ_a only approximately for a particular T_a, by using the phase diagram given in Figure 7.3. In case of a constant ρ_a, the steady state temperature of the system is T_a.
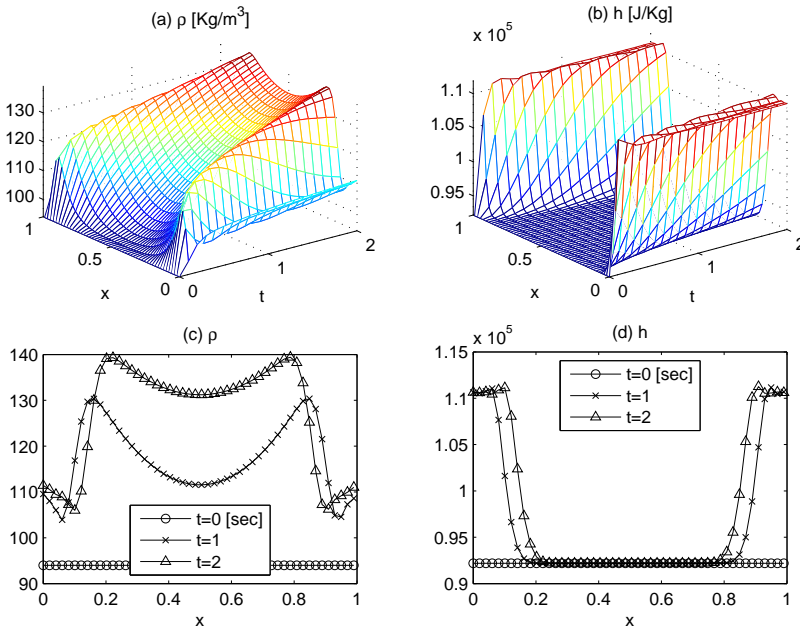
Figure 7.4: Example: Small jump in the enthalpy. (a), (b) Graphs of ρ and h with complete time history. (c), (d) Plots of ρ and h, at $t = 0,\ 1,\ 2[s]$.

Example: Large jump in the enthalpy at the boundary

In this example, it is demonstrated experimentally that, taking h_a different from h_Γ may cause problem in the system convergence. We use the data given in Table 7.4. We set $h_a = 2h_\Gamma$, to make the enthalpy profile discontinuous at the boundary. We do not get convergence in 100 Newton iterations in the first time step. This is not totally unexpected because, in this case, we have an ill-posed problem.

Example: Small jump in the enthalpy at the boundary

We repeat the above example, except that, $h_a = 1.2h(x, 0), x \in \Gamma$ is used. In Figure 7.4(a) and (b), we plot the two state variables, ρ and h, for entire time domain. In Figure 7.4(c) and (d), the same variables are provided at three time instances. Both variables, ρ and h, exhibit steep gradients, near the boundary. They do not become smooth even at steady state. The value of X_G has a similar profile (not shown). We conclude that a discontinuous enthalpy at the boundary, may result in steep gradients in the solution variables, which is physical. This example also shows that an ill-posed problem may converge to some value.
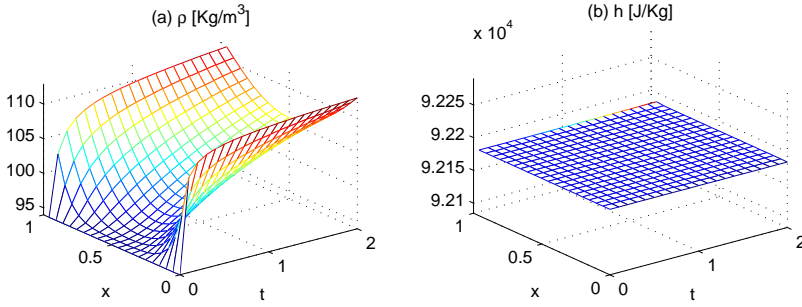
Figure 7.5: Example: No jump in the enthalpy at the boundary. Plots of ρ and h.

Example: No jump in the enthalpy at the boundary

In this example, we use a continuous enthalpy at the boundary i.e., $h_a = h(x, 0), \ x \in \Gamma$. Other parameters are the same as used in the last two examples. Solution plots, for the two state variables, are given in Figure 7.5. All solution variables, in this case, are smooth. The system enthalpy remains constant over entire spatial and temporal domain.

7.4   Simulation results for the open system

In order to open up the system for mass and energy fluxes, we consider the nonhomogeneous Robin boundary conditions. The solution algorithm is provided in Chapter 5, for a $2D$ isolated flow system. Rewriting Equations (5.10) and (5.16) from Sections 5.2.1 and 5.2.2 respectively, we have

$$S^{(11)} \, \boldsymbol{\delta\rho} + S^{(12)} \, \boldsymbol{\delta v_x} + S^{(13)} \, \boldsymbol{\delta v_y} + \boldsymbol{f}^{(\rho)} = \boldsymbol{0}, \qquad (7.11)$$

$$S^{(20)} \, \boldsymbol{\delta\rho} + S^{(21)} \, \boldsymbol{\delta s} + S^{(22)} \, \boldsymbol{\delta v_x} + S^{(23)} \, \boldsymbol{\delta v_y} + \boldsymbol{f}^{(s)} + S^{(24)} \, \boldsymbol{\delta T} = \boldsymbol{0}. \qquad (7.12)$$

The modified definitions of the global matrices and vectors are given as

$$S_{ij}^{(11)} = \frac{1}{\Delta t} \int_\Omega \phi_i \phi_j d\Omega - \int_\Omega v_x^k \phi_j \frac{\partial \phi_i}{\partial x} d\Omega - \int_\Omega v_y^k \phi_j \frac{\partial \phi_i}{\partial y} d\Omega + \int_\Gamma k_m \phi_i \phi_j \, d\Gamma,$$

$$f_i^{(\rho)} = \frac{1}{\Delta t} \int_\Omega (\rho^k - \rho^{\tau-1}) - \int_\Omega \rho^k v_x^k \frac{\partial \phi_i}{\partial x} d\Omega - \int_\Omega \rho^k v_y^k \frac{\partial \phi_i}{\partial y} d\Omega + \int_\Gamma k_m (\rho^k - \rho_a) \phi_i \, d\Gamma,$$

$$S_{ij}^{(20)} = h_a k_m \int_\Gamma \phi_i \phi_j d\Gamma,$$

$$S_{ij}^{(21)} = \frac{1}{\Delta t} \int_\Omega \phi_i \phi_j d\Omega - \int_\Omega v_x^k \phi_j \frac{\partial \phi_i}{\partial x} d\Omega - \int_\Omega v_y^k \phi_j \frac{\partial \phi_i}{\partial y} d\Omega + \int_\Gamma k_m \phi_i \phi_j \, d\Gamma,$$

$$S_{ij}^{(24)} = D \int_\Omega \left(\frac{\partial \phi_i}{\partial x} \frac{\partial \phi_j}{\partial x} + \frac{\partial \phi_i}{\partial y} \frac{\partial \phi_j}{\partial y} \right) d\Omega + k_h \int_\Gamma \phi_i \phi_j d\Gamma,$$

$$f_i^{(s)} = \frac{1}{\Delta t} \int_\Omega (s^k - s^{\tau-1}) \phi_i d\Omega - \int_\Omega s^k v_x^k \frac{\partial \phi_i}{\partial x} d\Omega - \int_\Omega s^k v_y^k \frac{\partial \phi_i}{\partial y} d\Omega$$

$$+ D \int_\Omega \left(\frac{\partial T^k}{\partial x} \frac{\partial \phi_i}{\partial x} + \frac{\partial T^k}{\partial y} \frac{\partial \phi_i}{\partial y} \right) d\Omega + h_a k_m \int_\Gamma (\rho^k - \rho_a) \phi_i d\Gamma + k_h \int_\Gamma (T^k - T_a) d\Gamma.$$

Note that only those matrices and vectors are redefined here which contain boundary integrals. These boundary integrals appear because of the nonhomogeneous boundary conditions their use in the weak forms of mass and energy equations (Equations (5.8) and (5.15)). The remaining matrices are given in Section 5.2.1 and 5.2.2. In the following 1D examples, we show that the modified solution algorithm for the flow system works well.

7.4.1   Example. Steady state velocity

In this example, we set two different values of T_a, at two boundary nodes (Table 7.5), where $T_a = T(\rho_a, h_a)$ and ρ_a is determined from Figure 7.3. This establishes a velocity profile which varies initially but approaches to a steady-state value. Ideally, $\lim_{t\to\infty} v(x,t) = v(x)$, but approximately, $v(x,2)$ attains a steady-state value. We provide plots of v at three time instants in Figure 7.6(b). The steady state velocity at two boundary nodes is different because of a difference in the densities at the corresponding nodes, as shown in Figure 7.6(a).

Table 7.5: Example: Steady state velocity

k_m	$T(x,0)$	$X_G(x,0)$	ρ_a at $x = 0$	ρ_a at $x = 1$
1.5	290	0.15	114	74

7.4.2   Example: Cyclic boundary conditions

In this example, we set the environmental parameter ρ_a such that $T(\rho_a, h_a)$ varies sinusoidally with time (Table 7.6). As a result, the velocity is from the right to the
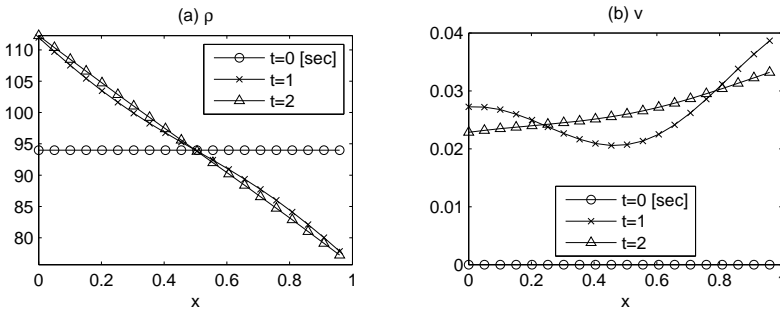
Figure 7.6: Example: Steady state velocity. (a) The density plots at $t = 0, 1, 2[s]$. (b) The velocity plots at $t = 0, 1, 2[s]$. The velocity approaches (approximately) a steady-state value after $t = 2[s]$.

Table 7.6: Example: Cyclic boundary conditions

k_m	$T(x,0)$	$X_G(x,0)$	ρ_a at $x = 0$	ρ_a at $x = 1$
1.5	290	0.15	94+10 $sin(\pi t)$	94-10$sin(\pi t)$

left for some time and vice-versa for other times. The cyclic behavior is shown in Figure 7.7. The purpose here is to show that the solution algorithm and its computer implementation work well for the cyclic boundary conditions. In our view, the results shown in Figure 7.7 are consistent with a sinusoidally varying fluxes of mass and energy.

7.4.3   Example: Pure gas flow

We initially take pure gas in the system and set outflow conditions, as provided in Table 7.7. The outflow conditions keep the system in gaseous form. The solution results are physically explainable and acceptable. In this example, we demonstrate that

Table 7.7: Example: Pure gas flow

k_m	$T(x,0)$	$X_G(x,0)$	ρ_a
1.5	310	1	$\rho(0,0) - 10$

the method is applicable to situations, where we have a pure gas flow ($X_G = 1$). An outflow of mass causes a decrease in the system density, ρ, as shown in Figure 7.8(a). A decreasing ρ keeps the gaseous state within the system. This can be understood by realizing $X_G = X_G(\rho, h)$ and by the fact that h, in this case, varies very slightly (Figure 7.8(e)). Therefore, a decreasing ρ maintains a pure gas phase within the system. Alternatively, the ρ-h diagram (Figure 3.1(c)) can be used to verify the value for the
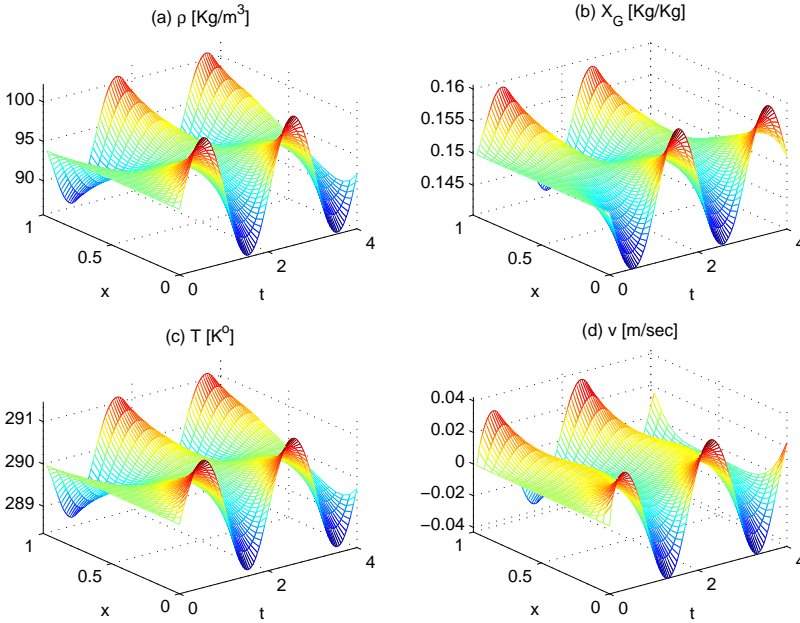
Figure 7.7: Example: Cyclic boundary conditions. Plots of system variables.

gas mass fraction, i.e., $X_G(x,t) = 1 \; \forall (x \in \Omega, t)$, once the system is solved for the state variables (ρ, h).

7.4.4 Example: Pure liquid flow

In this example, the initial values of X_G are taken very small. That is, the system is very close to a pure liquid state. We the set inflow conditions given in Table 7.8. Plots for the solutions variables are given in Figure 7.9(a)-(f). In Figure 7.9(b), a transition from the two-phase flow to one-phase flow is clearly visible. During this transition, other system variables attain constant spatial profiles. In other words, a pure liquid state acts like a spatially zero dimensional system. In our view, the available database supports an incompressible Propane, when it is pure liquid.

Table 7.8: Example: Pure liquid flow

k_m	$T(x,0)$	$X_G(x,0)$	ρ_a	$T_a = T(\rho_a, h_a)$
1.5	295	5×10^{-4}	$\rho(0,0) - 10$	295.11
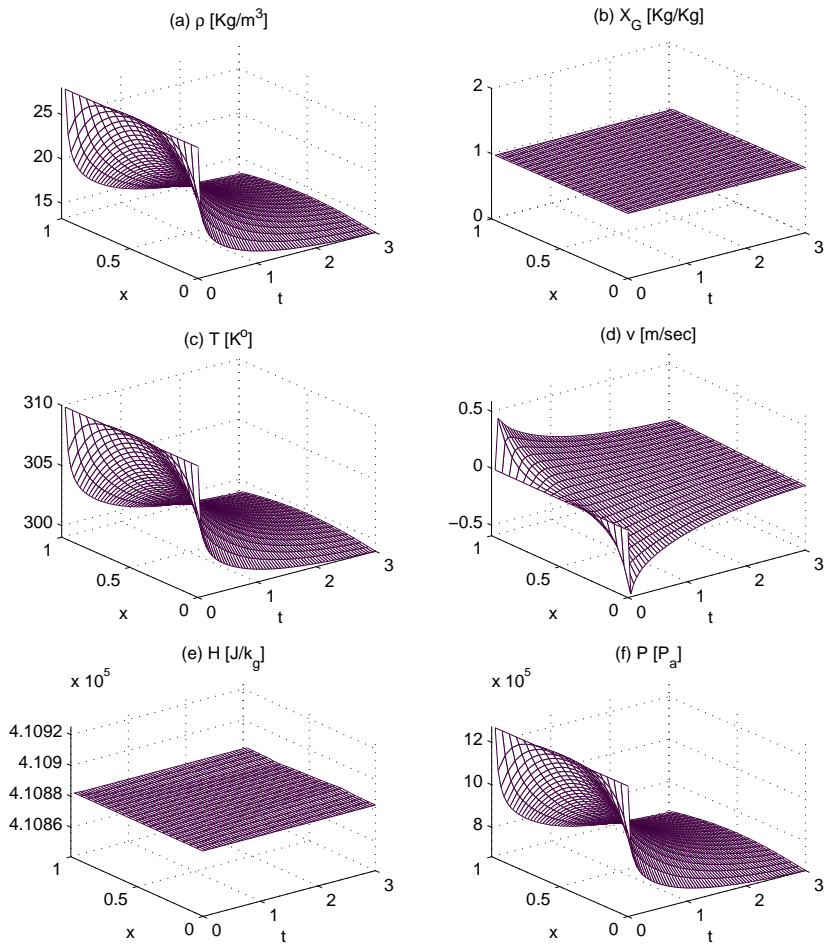
Figure 7.8: Example: Pure gas flow. Plots of system variables.
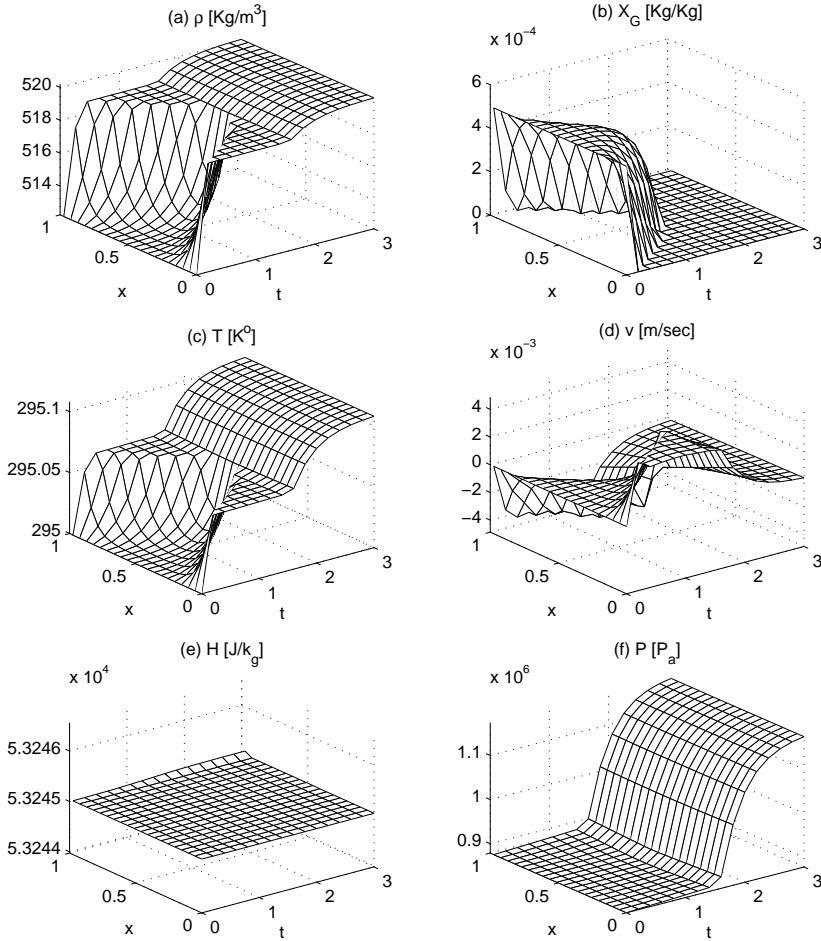
Figure 7.9: Example: Transition from two-phase to pure liquid. Plots of system variables.

7.5   Conclusions

It is concluded that the selection of the ambient and system parameters, in a specific way, enables us to use nonhomogeneous boundary conditions, for acceptable solutions. The use of $h_a = h_\Gamma$ and an estimation of k_h from k_m, in our algorithm, provides smooth and physically explainable solution results. It seems that the available database supports an incompressible flow, for the pure liquid phase.

Chapter 8

Conclusions and future research

We numerically solve a more recent model (the density–enthalpy method), for solving two–phase flow, whose origin, merits, and a comparison with other approaches are given in the first chapter of the thesis. The density–enthalpy method uses mass and energy balances in the model and hence the physical basis are complete. The use of enthalpy as primary variable is consistent with the previous works in the literature whereas the choice of density as the primary variable means that the model represents the actual evolution of mass in a relatively simple formulation. Darcy's law and the density-enthalpy phase diagrams are also important components in the model. Arendsen *et al.* uses an efficient algorithm to construct these phase diagrams where, the total Gibbs free energy as a function of thermodynamic variables is minimized implicitly.

In this thesis, the solution algorithm is extended to two dimensions. As our understanding for the model advanced with time, the solution algorithm is also developed, updated and modified, accordingly. In its latest form, the algorithm is very efficient and can be used to solve isolated as well as open system to mass and energy fluxes. The stability and error analysis is also carried out. Further, it is found that the non–homogeneous boundary conditions make the problem ill-posed. A criterion for the parameters selection is proposed to prevent ill-posedness. In our view, the results are physically acceptable.

By using finite elements, the solution algorithm works well for structured, unstructured, and stretched meshes. Initially, it seemed that SUPG is necessary because of large gradients in the solution variables, near the boundary (Chapters 3 and 4). Later on, however, ill-posed boundary conditions were found responsible for the steep (nonphysical) gradients. Eventually, the standard Galerkin algorithm is used instead of SUPG because of its simplicity and accuracy. It works well for all examples, where we do not have any ill-posed problems due to the boundary conditions.

The IMEX and Euler backward time integration, with a Picard scheme to solve the nonlinear problem, provide physically acceptable solutions. However, they require a small time step ($\Delta t < (\Delta x)^2/10$) for convergence. A small time-step forces computa-

tions to be excessively large. For this reason, it is concluded that a semi-implicit time integration scheme is not suitable for the model we use. Instead, a fully-implicit time integration scheme with a Newton-Raphson iteration for the nonlinear problem is recommended because it permits the use of large time steps. This is a major advantage to minimize computation time.

For the sake of a stability analysis, the original model is linearized to a "two-equation" system. The eigenvalues of the linearized system suggest that the continuous system is unconditionally stable. It is also observed that the isolated system can be solved with one equation provided that the velocity is small. That is, one state variable is sufficient to compute all the system variables. One state variable for the isolated system is consistent with the Gibbs phase rule.

The fact that pressure can be prescribed by temperature alone, (and vice versa) plays an important role in the thesis. For example, the nonhomogeneous boundary conditions make the problem ill-posed because $P = P(T)$. The same fact enables us to estimate k_h, numerically. Furthermore, it enables us to show that diffusion of heat within the system and across the boundaries is very small, as compared to the other terms. The knowledge of small heat diffusion enabled us to use nonzero boundary fluxes.

On the basis of this analysis, it is concluded that the numerical density-enthalpy method can be used for solving two-phase flow problems efficiently.

8.1 Future research

One of the important components of the density-enthalpy method are the pre-computed phase diagrams i.e., a database containing relations among certain variables at different phases. The database available to us is limited to pure Propane and it is valid for a limited range of T and X_G. Developing databases for other substances will enable us to apply the model on these substances and to have generalized results for the density-enthalpy model.

Comparison of the solution set, as obtained by the density-enthalpy method, with other traditional techniques, like the phase-field or level-set method, will provide an alternative test for the consistency of these results. Furthermore, the use of adaptive mesh size and adaptive time stepping is expected to improve solution results in terms of accuracy and efficiency. For unstructured grids, we experience wiggles near high gradient regions. In such cases, SUPG is expected to give smooth results.

The thesis contains two-phase examples, predominantly. One reason for this practise is that, the available phase diagrams lie in this range. The pure phases, liquid or gas, lie at the edge of the reliable region of the phase diagrams. A further investigation of one-phase flow problems, even with the available phase-diagrams, might be fruitful.

In [1, 2] the density-enthalpy method is applied to multi-component $0D$ flow systems (such as food processing and boiler system). Once the database of desired components are available, the multi-component model may be used to solve such systems.

We expect that it will further show the applicability of the model.

In the development of the solution algorithm, we mainly focussed on the discretization part i.e., going from continuous model to the discrete form $Ax = b$. We use a direct solver to find x, because we used small systems (i.e., suitable number of variables) in our examples. For larger systems, it is necessary to look for an iterative solver.

Bibliography

[1] A. R. J. Arendsen, A. I. van Berkel, A. B. M. Heesink, and G. F. Versteeg. Dynamic modelling of thermal processes with phase transitions by means of a density-enthalpy phase diagram. 7th World Congress of Chemical Engineering, Glasgow, Scotland, 2005.

[2] A. R. J. Arendsen and G. F. Versteeg. Dynamic modelling of refrigeration cycles using density and enthalpy as state variables. 17th International Congress of Chemical and Process Engineering, Prague, The Czech Republic, 2006.

[3] A. R. J. Arendsen and G. F. Versteeg. Dynamic Thermodynamics with Internal Energy, Volume, and Amount of Moles as States: Application to Liquefied Gas Tank. Ind. Eng. Chem. Res. 48, pp. 3167-3176, 2009.

[4] Ibrahim, F. J. Vermolen, and C. Vuik. Application of the numerical density-enthalpy method to the multi-phase flow through a porous medium. Procedia Computer Science 1 (2010) 781-790, Amsterdam, The Netherlands, 2010.

[5] Ibrahim, C. Vuik, F.J. Vermolen, D. Hegen. Numerical Methods for Industrial Flow Problems (I). Delft University of Technology, Report 08-13, 2008.

[6] Ibrahim, C. Vuik, F.J. Vermolen, D. Hegen. Numerical Methods for Industrial Flow Problems (II). Delft University of Technology, Report 09-10, 2009.

[7] Ibrahim, C. Vuik, F.J. Vermolen. Numerical Methods for Industrial Flow Problems (III). Delft University of Technology, Report 10-23, 2010.

[8] Ibrahim, C. Vuik, F.J. Vermolen. Numerical Methods for Industrial Flow Problems(IV). Delft University of Technology, Report 11-03, 2011.

[9] M. Fabbri and V. R. Voller. The Phase-Field Method in the Sharp-Interface Limit: A comparison between Model Potentials. Journal of Computational Physics, 1997.

[10] V. R. Voller. An enthalpy method for convection-diffusion phase change. International Journal for Numerical Method in Engineering, Vol. 24, pp. 271-284, 1987.

[11] V. R. Voller and C. R. Swaminathan. Fixed grid techniques for phase change problems: A review. International Journal for Numerical Mehtod in Engineering, Vol. 30, pp. 875-898, 1990.

[12] A. Abouhafç. Finite Element Modeling Of Thermal Processes With Phase Transitions. Master Thesis, 2007, Delft University of Technology.

[13] E. Javierre, C. Vuik, F. J. Vermolen, S. van der Zwaag. A comparison of numerical models for one-dimensional Stefan problems. J. Comp. Appl. Math., 192, 445-459, 2006.

[14] H. Emmerich. The Diffuse Interface Approach in Materials Science, Thermodynamic Concepts and Applications of Phase-Field Models. Springer, Berlin, 2003.

[15] J.H. Brusche, A. Segal, and C. Vuik. An efficient numerical method for solid-liquid transitions in optical rewritable recording. International Journal for Numerical Methods in Engineering, 77, pp. 702-718, 2009.

[16] O.C. Zienkiewicz, R.L. Taylor, & J.Z. Zhu. The Finite Element Method, Its Basis & Fundamentals. 6e, Butterworth-Heinemann, Oxford, 2005.

[17] K. A. Hoffmann, S. T. Chiang. Computational Fluid Dynamics, Vol I. 4e, EES, Wichita, USA, 2000.

[18] J. van Kan, A Segal, F. Vermolen. Numerical Methods in Scientific Computing. VSSD, Delft, 2005.

[19] R. J. Leveque. Finite Volume Methods for Hyperbolic Problems. Cambridge University Press, Cambridge, 2002.

[20] J.N. Reddy. An Introduction to the Finite Element Method. 2e, McGraw-Hill, New York, 1993.

[21] A. Faghri, Y. Zhang. Transport phenomena in multiphase systems. Elsevier Inc., pp. 111, London, 2006.

[22] H. S. Udaykumar, R. Mittal, and W. Shyy. Computation of Solid-Liquid Phase Fronts in the Sharp Interface Limit on Fixed Grids. Journal of Computational Physics 153, pp. 535-574, 1999.

[23] S. Chen, B. Merriman, S. Osher, P. Smereka. A simple level set method for solving Stefan problems. Journal of Computational Physics, v.135 n.1, p.8-29, July 15, 1997.

[24] S. Osher, J. A. Sethian. Fronts propagating with curvature-dependent speed: algorithms based on Hamilton-Jacobi formulations. Journal of Computational Physics, v.79, pp.12-49, Nov. 1988.

[25] A. Faghri, Y. Zhang, J. Howell. Advanced Heat and Mass Transfer. Global Digital Press, Columbia, 2010.

[26] B. Nedjar. An enthalpy-based finite element method for nonlinear heat problems involving phase change. Computers and Structures, Vol. 80, Issue 1, pp. 9-21, 2002.

[27] G. Comini, S. DelGiudice, B. W. Lewis, O. C. Zienkiewicz. Finite element solution of non-linear heat conduction problems with special reference to phase change. Int. J. Numer. Meth. Engng., 8, pp. 613624, 1974.

[28] G. Segal, C. Vuik and F. J. Vermolen. A conserving discretization for the free boundary in a two-dimensional Stefan problem. J. Comp. Phys., 141, pp. 1-21, 1998.

[29] K. Atkinson, W. Han. Theoretical Numerical Analysis. Springer, pp. 209, Berlin, 2009.

[30] G. I. Barenblatt. Scaling, Self-similarity, and Intermediate Asymptotics. Cambridge University Press New York, 2005, page 181.

[31] L. J. Christiansen, M. L. Michelsen, A. Fredenslund. Naphtali-Sandholm Distillation Calculations For NGL Mixtures Near The Critical Region. Computers & Chem. Engng, Vol. 3, pp. 535-542, 1979.

[32] M. L. Michelsen. Calculation of phase envelopes and critical points for multicomponent mixtures. Fluid phase equilibria, 4(1980) 1-10., 1980.

[33] M. L. Michelsen. The isothermal flash problem. Part I. Stability. Fluid phase equilibria, 9(1982) 1-19, 1982.

[34] M. L. Michelsen. The isothermal flash problem. Part II. Phase-split calculation. Fluid Phase Equilibria, 9 (1982) 2 l-40, 1982.

[35] M. L. Michelsen. Calculation of multiphase equilibrium. Computers Chem. Engng Vol. 18. No. 7. pp. 545-550. 1994.

[36] J. Bear. Dynamics of fluids in porous media. American Elsevier Publishing Company Inc., New York, 1972.

[37] Z. Chen, G. Huan, Y. Ma. Computational methods for multiphase flow in porous media. SIAM, 2006.

[38] C. Vuik, P. van Beek, F. J. Vermolen, J. van Kan. Numerical methods for ordinary differential equations. VSSD, Delft, 2007.

[39] D. Braess. Finite Elements, Theory, Fast Solvers, and Applications in Elasticity Theory. Cambridge University Press, New York, 2007.

[40] G. F. Pinder, W. G. Gray. Essentials of multiphase flow and transport in porous media. Jonn Wiley & Sons, Inc., New Jersey, 2008.

[41] C. T. Crowe. Multiphase flow handbook. Taylor & Francis Group, LLC, Florida, 2006.

[42] D. Y. Peng and D. B. Robinson. A new two-constant equation of state. Industrial and Engineering Chemistry Fundamentals 15(1) pp. 59-64, 1976.

[43] I. Garrido, G. E. Fladmark and M. Espedal. An improved numerical simulator for multiphase in porous media. Int. J. Numer. Meth. Fluids Vol. 44, pp. 447-461, 2004.

[44] J. W. Murdock. Fundamental fluid mechanics for the practicing engineer. CRC Press, pp. 25-27, 1993.

[45] O. Redllich, J. N. S. Kwong. On the thermodynamics of solutions (V). An equation of state. Chem. Rev. Vol. 44, pp. 233-244, 1949.

[46] G. Han, G. P. Rangaiah. A method for multiphase equilibrium calculations. Computers & Chemical Engineering, Volume 22, Issues 78, pp. 897-911, 1998.

[47] S. Saha, J. J. Carroll. The isoenergetic-isochoric flash. Fluid Phase Equilibria, Volume 138, Issues 1-2, Pages 23-41, 1997.

[48] D. Muller and W. Marquardt. Dynamic MultiplePhase Flash Simulation: Global Stability Analysis versus Quick Phase Determination. Computers & Chemical Engineering (1997), Volume 21, Issue Supplement 1, Elsevier, pp. S817-S822.

[49] L. E. Baker, A. C. Pierce, and K. D. Luks. Gibbs energy analysis of phase equilibria. Society of Petroleum Engineering Journal, 22, pp. 731-748.

[50] K. S. Zadeh. A mass-conservative switching algorithm for modeling fluid flow in variably saturated porous media. J. Comput. Phys. 230 (3), pp. 664-679, 2011.

[51] P.C.D. Milly. A mass conservative procedure for time stepping in models of unsaturated flow. Adv. Water Resour. Volume 8, pp. 32-36, 1985.

[52] M.A. Celia, E.T. Bouloutas, R.L. Zarba. A general mass conservative numerical solution for unsaturated flow equation. Water Resour. Res. 26, pp. 1483-1496, 1990.

[53] N. R. Eyres, D. R. Hartree, J. Ingham, R. Jackson, R. J. Sarjant and J. B. Wagstaff. The Calculation of Variable Heat Flow in Solids. Philosophical Transactions of the Royal Society of London. Series A, Mathematical and Physical Sciences, Vol. 240, No. 813, 1946.

[54] J. Crank. Free and Moving Boundary Problems. Oxford University Press, New York, 1984.

[55] P. H. Price, M. R. Slack. The effect of latent heat on numerical solutions of the heat flow equation. British Journal of Applied Physics, Volume 5, Issue 8, pp. 285-287, 1954.

[56] M. E. Rose. A method for calculating solutions of parabolic equations with a free boundary . Math. Comp. 14, pp. 249-256, 1960.

[57] G. E. Bell. On the performance of the enthalpy method. Int. J. Heat Mass Transfer, vol. 25, pp. 587-589, 1982.

[58] G. Soave. Equilibrium constants from a modified Redlich-Kwong equation of state. Chem. Eng. Sci. Vol. 27, pp. 1197-1203, 1972.

[59] S. Whitaker. Simultaneous heat, mass and momentum transfer in prous media: A theory of drying. Advances in heat Transfer 13, pp. 119-203, 1977.

[60] D. V. Nichita, S. Gomezb,E. Lunab. Multiphase equilibria calculation by direct minimization of Gibbs free energy with a global optimization method. Computers & Chemical Engineering, Vol. 26, Issue 12, pp. 1703-1724, 2002.

[61] G. A. Iglesias-Silva, A. Bonilla-Petriciolet, P. T. Eubank, J. C. Holste, K. R. Hall. An algebraic method that includes Gibbs minimization for performing phase equilibrium calculations for any number of components or phases. Fluid Phase Equilibria 210, pp. 229-245, 2003.

[62] K. M. Brantferger, G. A. Pope, K. U. Sepehrnoori. Development of a Thermodynamically Consistent, Fully Implicit, Equation-of-State, Compositional Steamflood Simulator. SPE Symposium on Reservoir Simulation, 17-20 February 1991, Anaheim, California.

[63] S. Krautle and P. Knabner. A reduction scheme for coupled multicomponent transport-reaction problems in porous media: Generalization to problems with heterogeneous equilibrium reactions. Water resources reasearch, Vol. 43, 2007.

[64] H. Buchholzer, C. Kanzow, P. Knabner, S. Krautle.The semismooth Newton method for the solution of reactive transport problems including mineral precipitation-dissolution reactions. Computer Optimization and Applications, pp. 193-221, 2011.

[65] J. Bruining C.J. van Duijn. Traveling waves in a finite condensation rate model for steam injection. Computational Geosciences, Vol. 10, Issue 4, pp. 373-386, 2006.

[66] W. Lambert, D. Marchesin, J. Bruining. The Riemann Solution for the Injection of Steam and Nitrogen in a Porous Medium. Transport in Porous Media 81, pp. 505-526, 2010.

[67] Z. Chen and R. E. Ewing. Comparison of Various Formulations of Three-Phase Flow in Porous Media. Journal of Computational Physics 132, pp. 362-373, 1997.

[68] J. Niessner, S. M. Hassanizadeh. A model for two-phase flow in porous media including fluid-fluid interfacial area. Water Resources Research Vol. 44, W08439, 10 PP., 2008.

[69] M. A. Celia, J. M. Nordbotten. Practical modeling approaches for geological storage of carbon dioxide. Ground Water, 47(5), pp. 627-638, 2009.

[70] B. Amaziane, M. Jurak. A new formulation of immiscible compressible two-phase flow in porous media. C. R. Mechaniques 336, pp. 600-605, 2008.

[71] D. Nayagum, G. Schafer and R. Mose. Modelling Two-Phase Incompressible Flow in Porous Media Using Mixed Hybrid and Discontinuous Finite Elements. Computational Geosciences Vol. 8, pp. 49-73, 2004.

[72] P. Binning & M. A. Celia. Practical implementation of the fractional flow approach to multi-phase flow simulation. Advances in Water Resources, Vol. 22, No. 5, pp. 461-478, 1999.

[73] J. Smoller. Shock wave and reaction–diffusion equations. A series of comprihensive studies in mathematics, volume 258, Springer-Verlag, New York, 1983.